Doctoral theses at NTNU, 2023:298

Haley Hoover

Electrical Resistivity of Materials in the Silicon Furnace

Doctoral thesis

NTNU
Norwegian University of Science and Technology
Thesis for the Degree of
Philosophiae Doctor
Faculty of Natural Sciences
Department of Materials Science and Engineering

NTNU
Norwegian University of
Science and Technology

Haley Hoover

Electrical Resistivity of Materials in the Silicon Furnace

Thesis for the Degree of Philosophiae Doctor

Trondheim, September 2023

Norwegian University of Science and Technology
Faculty of Natural Sciences
Department of Materials Science and Engineering

NTNU
Norwegian University of
Science and Technology

NTNU
Norwegian University of Science and Technology

Thesis for the Degree of Philosophiae Doctor

Faculty of Natural Sciences
Department of Materials Science and Engineering

ISBN 978-82-326-7296-7 (printed ver.)
ISBN 978-82-326-7295-0 (electronic ver.)
ISSN 1503-8181 (printed ver.)
ISSN 2703-8084 (online ver.)

Doctoral theses at NTNU, 2023:298

Printed by NTNU Grafisk senter

For my grandfather, who saw me begin this journey, but did not get to see me finish it.

PREFACE

This thesis is submitted to the Norwegian University of Science and Technology (NTNU), in partial fulfillment of the requirements for the degree of Philosophiae Doctor. The present work was conducted at the Department of Material Science and Engineering at NTNU, Trondheim, Norway, during the period from August 2019 to July 2023 under the supervision of Professor Merete Tangstad.

This report has been partly funded by the SFI Metal Production, (Centre for Research-based Innovation, 237738). The authors gratefully acknowledge the financial support from the Research Council of Norway and the partners of SFI Metal Production. This report is also published as part of the project “Electrical Conditions in Submerged Arc Furnaces—Identification and Improvement” (SAFECI), with financial support from the Research Council of Norway (project number 326802) and the companies Elkem, Eramet Norway, Finnfjord, and Wacker Chemicals Norway.

Haley Hoover

July 2023, Trondheim

ACKNOWLEDGMENTS

I embarked on this journey to complete a PhD almost four years ago, and in that time there have been many personal and professional ups and downs. In this time of reflection, I am reminded that no one accomplishes anything alone. There have been so many people who have helped me reach this point and I would like to take this opportunity to thank some of them.

First and foremost, I must thank my supervisor Merete Tangstad, who gave me this incredible opportunity and has given me excellent guidance and feedback. She works tirelessly, yet with endless patience and I am a better researcher for having known her. I would especially like to acknowledge her help finishing this thesis while she was enjoying her summer vacation. I would also like to thank my co-supervisor Gudrun Sævarsdóttir, who has known me since my time in Iceland, without her I would not have been introduced to metallurgy.

I am also thankful for my main collaborators, Gerrit, Meggi, Sethu, Khadija, who all stepped up to help me with my experiments and give my injured arms a much-needed break. I would also like to thank Gerrit (again) and Bendik for troubleshooting the resistivity equipment with me.

I would also like thank the many engineers and equipment experts working in Bergbygge, who are the backbone of the department. Dmitry, Arman, Marit, Pål, Audun, Berit, just to name a few. They are all essential to getting the job done and I thank them for their hard work and support. Additionally, I thank Morten for helping with the EPMA and Katherina for training me on the CT.

A special thanks must also be given to the many people who worked on the pilot scale experiment. It was a large collaboration between NTNU, SINTEF, and the industry which resulted in multiple publications. I would like to single out Vegar Andersen, who worked with me on the excavation publication, and Ingeborg Solheim, who helped with the logistics of the excavation.

Thanks to the SiMnTiAl group for the good working environment and for all the presentation practice and feedback.

Lastly, I would like to thank my family, Mom, Dad, Lindsay, AJ, Matthew, Dexter, Stella, and Willow. They have always encouraged me, even when my work has sent me very far away. My Aunt Bert, who first gave me the title “Dr. Haley Hoover” many years ago. Finally, my partner Sondre, who not only brought me here to this beautiful country, but remains my greatest supporter, my biggest believer, and my dearest friend.

SUMMARY

Production of silicon via carbothermic reduction of quartz (SiO_2) is an energy intensive and carbon dioxide (CO_2) emitting process. As the industry seeks to reduce both energy consumption and carbon emissions, the understanding of the energy distribution in the furnace is increasingly important. Most of the electrical energy in the furnace will be directed to the arc, which supplies the heat in the lower area of the furnace, where the silicon producing reaction occurs. Current may also travel through the conductive silicon carbide (SiC) crust. Any remaining current must pass through the charge mix, consisting of quartz and carbon materials. As the carbon material enters the furnace, it is heated and exposed to silicon oxide (SiO) gas. Both the changing temperature and the chemical reactions with the SiO gas will transform the material to SiC, changing its electrical properties. There is scarce literature on the resistivity of the materials as they are transformed in the furnace. Thus, the resistivity of the partially transformed carbon materials (char, coal, and charcoal) in the furnace was investigated as the main part of this thesis. Additionally, the transformation of the carbon to SiC was also investigated, as well as the resistivity of charge mixtures that included quartz. Finally, an excavation of a 160 kW pilot scale silicon furnace was presented.

The transformation of coal, char, and charcoal to SiC was studied through placing a carbon bed above an SiO generator and heating it at temperatures between 1750-1850 °C. The results showed similar surface crystal formation to that seen in other literature, with both SiC whiskers and crystals being seen in all three materials, although charcoal saw very little whisker formation. The main SiC formation will however be the SiO reacting with the carbon cell walls. The mechanism of SiC formation followed the grain model for all three carbon materials, where SiC formed along the outer edges of the particle and around the pores. Elemental silicon began to form in the pores in areas with high SiC content, but areas of carbon could still be found on the same particle. It was seen that since the material is transformed in a packed bed, there was unequal access to the SiO gas and a temperature gradient, causing some particles to be more highly transformed than others, even within the same area of the setup. Elemental silicon was produced in varying amounts, with charcoal producing the most and at a lower temperature than the char and coal.

Mechanical strength of the materials from coal and char was studied using compression testing. It was seen that the mechanical strength decreased as the coal was converted to SiC, until silicon began to form. However, the opposite was seen in the char and in general, the char was weaker than the coal. Partly transformed charcoal was too weak to be measured. All materials were weaker than the literature reported values for commercial SiC.

The resistivity of coal, char, and charcoal was measured between 25-1600 °C in a four-point method setup. The range for all three carbon materials was between 7-20 mΩm at 1600 °C. Charcoal had the highest range, containing both the lowest and highest resistivity at 1600 °C. Two industrial charcoals and one charcoal made from woodchips at 1600 °C were tested. The homemade charcoal was less sensitive to temperature and was conductive at low temperatures. However, at high temperatures it had a higher resistivity then the industrial charcoal. Three types of char were tested, and the range was between 10-15 mΩm at 1600 °C. Both untreated and heat-treated chars were tested, and the lower volatiles in the heat-treated chars lowered the resistivity and made it less sensitive to temperature changes. One type of coal was tested, and it had a range of between 5-10 mΩm at 1600 °C. Density explained the trends at 1000 °C, but at 1500 °C the density could not predict the resistivity.

The resistivity of partially transformed carbon materials containing SiC ranging from 30-72 % and Si ranging from 0-36 % was measured between 25-1600 °C. The resistivity decreased with increasing temperature for all materials. The resistivity increased with increasing SiC content, and then decreased as elemental silicon formed. The presence of silicon lowered the resistivity, but this was not related to the quantity of silicon in the sample within the range produced. It was found that above 1300 °C, the SiC crust will be more conductive than the partially transformed SiC material. At lower temperatures, the partially transformed SiC may be as conductive or less conductive than the SiC crust. Resistivity of charge mixtures containing quartz, char, woodchips (charcoal), and silica-iron ore were also measured and were found to be dependent of the amount of char in the sample, as it was the main conductor in these experiments.

An excavation of a 160 kW pilot scale Si furnace was conducted with the intention of studying the various zones of the furnace and comparing them with theory as well as results from other silicon furnace excavations. The results were similar to those of other excavations. However, a top cavity was seen high in the furnace and was held together by a layer of loose charge and condensate. The condensate contained silica, alumina and potassium and sodium oxides. No cavity was seen around the electrode tip, but it was likely small during operations and collapsed during cooling. No SiC crust was found, but SiC was seen in other forms throughout the furnace. A large silicon-slag layer was seen, with the slag consisting of silica, alumina, and calcia, usually mixed with SiC. Silicon was also found in droplets above the cavity and in more sizable quantities below the cavity. The resistivity profile of the various zones found in the furnace was also estimated based on the previous work. It predicts that the silicon-slag layer will have the lowest resistivity, followed by the partly reacted charge materials, which will have different resistivities based on the temperature and composition. The condensate layer and areas of inactive charge will likely be nonconductive based on the SiO_2 content and the low temperature.

The findings in this thesis aim to provide more knowledge to the conductivity of the materials in the furnace as they are transformed. This will ensure that the energy distribution in the furnace maintains the temperature and resistivity profile needed for good operations. Good operations will lead to lower energy consumption and CO_2 emissions. Furthermore, the data may be used to improve existing models of the furnace through providing a temperature profile for the conductivity of the charge mix.

LIST OF PUBLICATIONS

1. Hoover, H., Fromreide, M., Sævarsdóttir, G., & Tangstad, M. (2023). Bulk resistivity of materials in the Si/FeSi Furnace. *Processes*, 11(7), 1-16.
2. Hoover, H., Andersen, V., Sævarsdóttir, G., & Tangstad, M. (2022). Excavation of 160kW Pilot scale Si furnace. *Aspects in Mining and Mineral Science*, 9(2), 1013-1026.
3. Hoover, H., Glowacki, M., Sævarsdóttir, G., & Tangstad, M. (2022). Electrical resistivity of charge materials in the Si process and its effect on energy and CO_2 emissions. *COM2022*. Montreal, Canada.
4. Hoover, H., Glowacki, M., Sævarsdóttir, G., & Tangstad, M. (2022). Electrical resistivity of charge materials in the Si/FeSi furnace. *Silicon for the chemical and solar industry XVI*. Trondheim, Norway: Norwegian University of Science and Technology.
5. Hoover, H., Sævarsdóttir, G., & Tangstad, M. (2022). Electrical resistivity of transformed carbon materials in the silicon furnace. *TMS Furnace Tapping*. Anaheim, USA.
6. Hoover, H., Sævarsdóttir, G., & Tangstad, M. (2021). Electrical resistivity of partially transformed silicon carbide made from coal. *INFACON XVI*. Trondheim, Norway.
7. Hoover, H., Pedersen, T., Sævarsdóttir, G., & Tangstad, M. (2020). Bulk Resistivity of SiC and Carbon Materials in the Silicon Furnace. *Silicon for the Chemical and Solar Industry XV* (pp. 65-74). Trondheim, Norway: Norwegian University of Science and Technology.

TABLE OF CONTENTS

LIST OF FIGURES

LIST OF TABLES

1 INTRODUCTION

1.1 SILICON PRODUCTION PROCESS

Silicon is becoming an increasingly important part of the modern world through its applications in electronics, solar cells, and silicones, to name a few. Norway is a significant producer of silicon, competing with much larger nations such as Russia and the United States. In 2019, Norway produced 370 000 tons of silicon, making it the third largest producer in the world [1].

Silicon is produced by carbothermic reduction of quartz (SiO_2) in a submerged arc furnace (SAF). The overall ideal mass balance is shown in Equation 1. However, silicon dioxide is not reduced by solid carbon (C) directly, but through a number of sub reactions.

$$SiO_{2(s)} + 2C_{(s)} = Si_{(l)} + 2CO_{(g)} \tag{1}$$

The process takes place is an SAF with three consumable carbon electrodes which supply electrical energy to the system. The furnace can be further divided into two zones, the low temperature zone and the high temperature zone. The relevant chemical reactions in each zone are depicted on the diagram in Figure 1. The high temperature zone is where most of the silicon is produced via Equation 4. Molten SiO_2 from the charge material reacts with intermediate solid silicon carbide (SiC) and liquid silicon (Si) to form silicon oxide gas (SiO) and carbon monoxide gas (CO) according to Equations 2 and 5.

SiO gas plays an important role as it forms the SiC intermediate (Equation 3) necessary for the silicon producing reaction (Equation 4). While the liquid silicon pool is tapped at the bottom of the furnace, the gas moves upwards through the raw material (charge) in the furnace. As the gases reach areas of lower temperature, they eventually react to condensed materials in the low temperature zone. This means it can reform SiO_2 and Si as it condenses (reverse of Equation 2) [2].

$$SiO_2 + Si = 2SiO_{(g)} \tag{2}$$

$$SiO_{(g)} + 2C = SiC + CO_{(g)} \tag{3}$$

$$SiO_{(g)} + SiC = 2Si + CO_{(g)} \tag{4}$$

$$2SiO_2 + SiC = 3SiO_{(g)} + CO_{(g)} \tag{5}$$

However, some SiO gas manages to escape the furnace and reach the charge top where it is exposed to oxygen in the air and forms silicon dioxide dust particles, called silica fume or microsilica. This microsilica is captured and sold to other industries and is an important product of the process. The carbon monoxide gas also oxidizes at the top of the semi-open furnace to form carbon dioxide (CO_2), which goes to the final off gas.

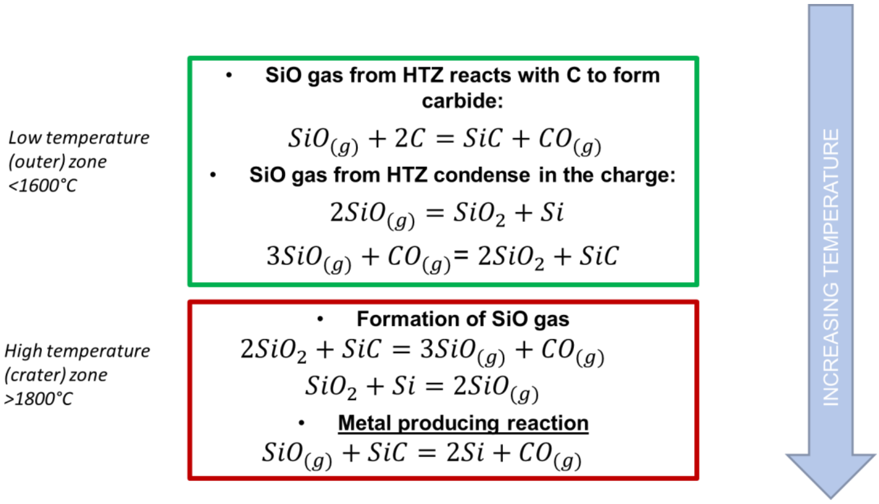

Figure 1. The low temperature zone (LTZ in the figure) outlined in green, and the high temperature zone (HTZ in the figure) outlined in red shows the important chemical reactions for silicon production.

Based on the thermodynamics of the Si-O-C system, a higher temperature in the high temperature zone of the furnace will give a lower SiO pressure. This is ideal for minimizing SiO gas losses. Similarly, a lower temperature in the low temperature zone will minimize SiO losses through favoring condensation. One of the ways in which this temperature profile is achieved is through ensuring that most of the current applied through the electrodes travels through to the bottom of the furnace via the arc. This supplies the heat required to sustain the endothermic reactions. However, current may also travel via the charge mix.

The charge mix is usually premixed and loaded in the furnace from the top, where the temperature is lowest. As the raw materials descend in the furnace, they are met with increasing temperature as well as SiO and CO gas. Among the raw materials, the carbon materials are the source of any conductivity, as quartz is an insulator. Carbon materials will first release moisture, then volatiles, and finally react with the rising gases. The combination of the physical and chemical changes of the carbon, in addition to the rising temperature, will change the electrical properties of the carbon.

Carbon materials in the furnace will react with SiO gas to form SiC, which is an important intermediate for the process as it is part of the silicon producing reaction (Equation 4). SiC initially formed from the transformation of carbon (Equation 3) will further transform at high temperatures to form SiC crust, which has been found to be highly conductive and may take a great portion of the current [3]. The resistivity of various carbon materials for metallurgical processes including coal, char (semicoke), coke, and charcoal have been studied previously by multiple authors [4] [5] [6] [7] [8] [9] [10]. In general, they agree that the resistivity decreases with increasing temperature. Therefore, in the furnace, the resistivity of the charge is decreasing as they descend towards the high temperature zone.

1.2 FURNACE EFFICIENCY AND POWER CONSUMPTION

Having the right temperature profile in the furnace is essential for good operations because it will keep the silicon yield high. Similarly, a high silicon yield will decrease energy consumption and CO_2 emissions. Both factors are becoming increasingly important in today's world. Silicon yield, also called silicon recovery (μ), is the amount of Si in the "metallic" product as a percent of the amount of Si in the quartz. This ratio is shown in equation 6. Typical Si yield can be as high as 95 % in Norway [11]. The specific power consumption is a function of both the furnace efficiency (η) and the Si yield. This is shown in equation 7, where (K_1) and (K_2) are constants based on the enthalpy of the total mass balance equations for production of

Si (Equation 1) and SiO after unit conversion, assuming the reactants are 25 °C and the products are 1600 °C and 1400 °C for solids and gases, respectively. Typical power consumption is 11-13 MWh/tSi [11].

Specific CO_2 emissions in Norway are typically calculated based on the carbon in the raw materials and the consumption of the electrodes, because emissions associated with energy production are excluded due to Norway's hydropower [12]. If the consumption of the electrodes is neglected, the CO_2 emissions can be based on the mass balance of carbon in the raw materials. In this case volatiles and fines are excluded. Power consumption decreases both as Si yield and furnace efficiency increase. The specific energy consumption (kWh/t Si) at 80-86 % furnace efficiency as a function of Si yield is shown in Figure 2. Also, the specific CO_2 emissions ($kgCO_2/kgSi$) as a function of Si yield are shown. As yield is increased both the power consumption and the CO_2 emissions decrease. The theoretical minimum based on the carbon balance in the furnace excluding the electrodes is 3.14 $kgCO_2/kgSi$.

$$Si\ yield = \frac{Si\ in\ metal}{Si\ in\ raw\ material} \tag{6}$$

$$Specific\ Power\ Consumption = \frac{1}{\eta} \cdot \left(\frac{K_1}{\mu} + K_2\right) \tag{7}$$

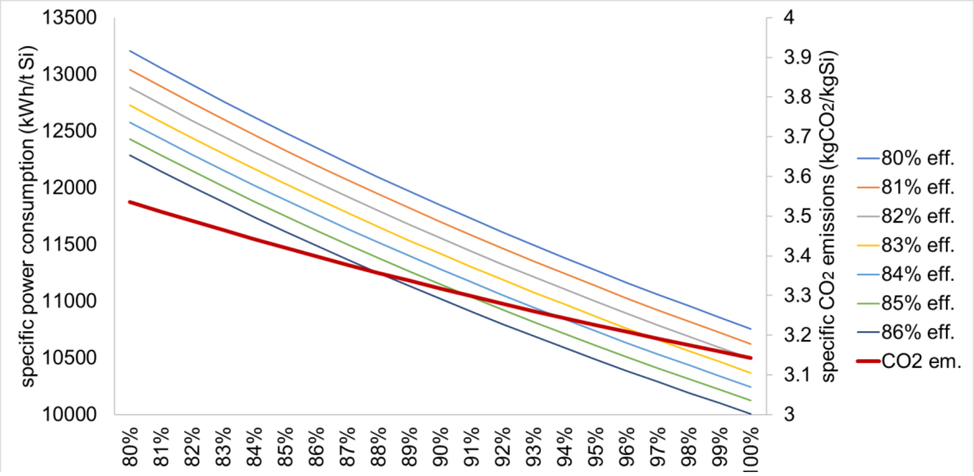

Figure 2. Specific power consumption (at various furnace efficiencies) and minimum specific CO_2 emissions (red line) versus Si yield. Increasing furnace efficiency decreases power consumption for the same Si yield. Increasing Si yield decreases power consumption and CO_2 emissions.

1.3 GOAL AND THESIS OUTLINE

Production of Si/FeSi requires high amounts of electrical energy and carbon materials which are becoming scarcer and more expensive. Understanding the transformation of the carbon materials as well as the energy development in the furnace are key to increasing process efficiency. Previous literature indicates that much of the electrical current delivered to the system via the electrode will pass through an electric arc, whereas the remaining current may pass through the silicon carbide crust or through the partially transformed raw materials depending on their conductivities [13]. The electrical resistivity in the arc and the SiC crusts have previously been investigated [3] [13] [14] [15], while there is scarce literature on the partly transformed charge material. Thus, the resistivity of transformed carbon materials and charge material mixes will be investigated. The conversion of the carbon materials to SiC is an important reaction in the furnace both metallurgically and electrically, as it will affect the Si yield. Most studies examine the formation of SiC for single particles or a few particles. However, in the furnace the particles will be transformed in a bed, where factors such as gas channeling and bed packing may affect both the conversion and the distribution of SiC. Hence in this work, the formation of SiC in the bed will be investigated for coal, charcoal, and char as starting carbon materials. Other factors such as density, porosity, and mechanical strength will also be discussed in the context of their effect on the bulk resistivity. Lastly, an excavation of a pilot scale silicon furnace is investigated to verify existing theory and/or discover gaps in preexisting knowledge.

This thesis is organized in the following way:

Chapter 1 introduces the main points of silicon production and the thesis goals.

Chapter 2 summarizes the existing literature on the material zones in the furnace, the electrical system, formation of silicon carbide, resistivity of silicon carbide and carbon materials, and previous excavations.

Chapter 3 presents the experimental methods and results regarding silicon carbide formation in a bed of particles.

Chapter 4 presents the experimental methods and results regarding the bulk resistivity measurements of the partly transformed SiC material detailed in Chapter 3, as well as mixtures of charge materials.

Chapter 5 presents a discussion of the results of Chapter 3 and 4.

Chapter 6 presents the excavation of a pilot scale Si furnace including a discussion.

Chapter 7 summarizes the main findings in this work, as well as suggestions for future work.

2 LITERATURE REVIEW

2.1 CURRENT PATHS IN THE SAF

The paths of the applied electrical current will determine the energy distribution of the furnace [14]. Accurate understandings of the current and voltage are essential for operations as they determine whether electrode position is adjusted or not [16]. For a stable operation the electrical current paths should be focused on the lower part of the furnace and minimized elsewhere. The electrical system is an important source of information for understanding the silicon production process as it controls the power and heat supply entering the furnace [17].

Based on the structure of the furnace, shown in Figure 3, there are four presumptive and logical paths the current may follow [2]. In the first path, the current travels from the electrode to the conductive materials bottom that contains liquid silicon and slag containing SiC particles. In the second path, the arc strikes the side wall, which is primarily SiC crust [3], with pores containing liquid silicon or gases. In the third path, the current is passing through the partly transformed charge material. The transformed charge in the furnace consists of quartz, partially transformed carbon to SiC, and woodchips transformed to charcoal. Generally, SiO_2 is an insulator, carbon is conductive, and woodchips will become conductive once they have sufficiently been transformed to charcoal at high enough temperature. The last path is electrode to electrode via the charge material.

Most of the current is believed to be passing through the electric arc onto one of its two possible paths. The electric arc is an important characteristic of the silicon process, as it is the main source of heat in the furnace. It is what ensures there is enough energy in the high temperature zone to raise the temperature to allow the main reactions to occur. According to Schei et al. [2], an electric arc is a type of current through gas characterized by its high current, low voltage drops, and high power. It’s worth noting that these arcs in the furnace are small, they are unsustainable at lengths longer than about 10 cm [13]. However, typical electrode movement is much greater than 10 cm at many points in the process [3] as shown in Figure 4. Therefore, arcs must strike the cavity walls in addition to the liquid silicon pool, and thus there is a significant portion of the current is passing through the SiC crust or the partially transformed charge. Some literature also suggests multiple arcs [15]. Additionally, some of the current will pass through the charge material, but how much depends on the resistivity of the charge mix, as the path favors least resistance.

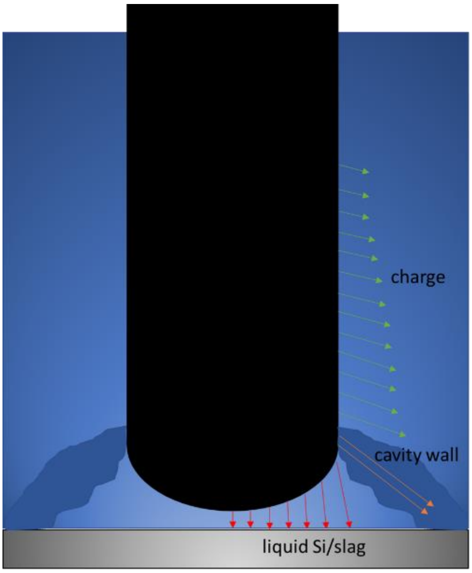

Figure 3. Schematic of possible current paths in the silicon furnace around a single electrode. The direct path through the liquid Si/slag is shown in red, the path through the SiC crust in orange, and the path through the charge is in green.

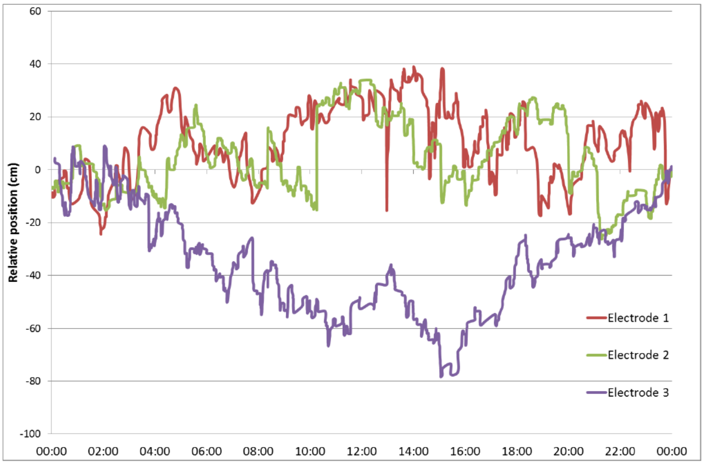

Figure 4. Example of electrode tip position over time from Wacker Chemicals Norway shows that typical electrode movement is greater than 10cm, used with permission from [3].

It is desirable to achieve high electrical resistance in the charge to generate more power for the electric arc and its surroundings [18]. Thermal energy must be generated at the electrode tips with a minimum amount of energy generated further up in the furnace to achieve optimal conditions for the reduction of SiO_2 [19]. To accomplish this charge material with high resistivity is desired because it allows for greater voltage without disruption to the process itself. When furnace resistance is too high there is increased slag formation, decreased sensitivity to electrode movements, and increased electrode wear [18]. If the operating resistance in the furnace is much higher than the resistance in the charge, the heat distribution will be altered as more heat is used to melt the raw materials and therefore less is available for the hearth. The operating resistance must therefore consider the resistance in the charge [17].

Tesfahunegn [14] [15] [20] [21] has worked to develop a 3D model of the SAF in ANSYS Maxwell using an eddy current solver that considers alternating current (AC). His work has successfully modelled the effects of side arcs, carbide configuration, and electrode shape and movement. He also investigated how the charge conductivity affected the various electrical parameters in the furnace. For example, power distributions in the carbide and the charge were more effected by electrode tip positions than holder positions. Increasing the number of side arcs decreased the furnace resistance and increased the current through the crater. When the main arc was considered and charge had a low conductivity, most of the power went through the main arcs and crater wall. However, when the charge's conductivity was increased by two orders of magnitude, the power in the charge increased by the same factor and decreased in the main arcs and crater wall. This trend was also seen when the main arcs were not included in the simulations. He concluded that the phase resistance of the furnace changes with a change in charge conductivity and/or the existence of the main arcs and side arcs. The furnace resistance decreased as the conductivity in the system increased. However, this modelling used a constant phase current, so for different configurations the total resistance changes the voltage, which is not typically representative of industrial operations, where the electrodes would be moved to compensate for the changing charge properties.

2.2 FORMER EXCAVATIONS

Many previous excavations have been done on various industrial and small-scale Si/FeSi furnaces. The results from these excavations are useful for studying the various zones and reactions that are expected from the theory. This is also an important background for understanding and modelling the electrical current paths in the furnace. Each excavation is unique, as the zones in the furnace will depend on the history of the operations, but commonalities exist among most of them [22]. This chapter summarizes the main findings of nine excavations, two ferrosilicon, 5 silicon, and two small scale furnaces.

A **17.5 MW FeSi75 furnace at Finnfjord** was excavated and the recreated cross section through two electrodes is shown in Figure 5 [23]. Raw materials were loosely packed on top of the furnace, and below that they had partially reacted and were held together by glassy condensates. One large cavity was found around each electrode. Additional gas channels were found on the outside of the crater walls. The crater walls consisted of mainly SiC and Si in a layered, but varying structure. Deposits from the gas phase could be found on the exteriors of the wall from the gas channels. The wall itself extended to the condensate zone around electrode 1. Both white and brown condensate layers were found on the outside of the crater walls and above the crater. There was a large piece of SiC that blocked the taphole at the end of the operations. Quartz had transformed to cristobalite around 20-50 cm below the top of the charge. Finally, FeSi was pooled in the bottom of the furnace and covered with SiC. Additional raw material was also found under the electrode, likely due to falling during stoking or during the excavation.

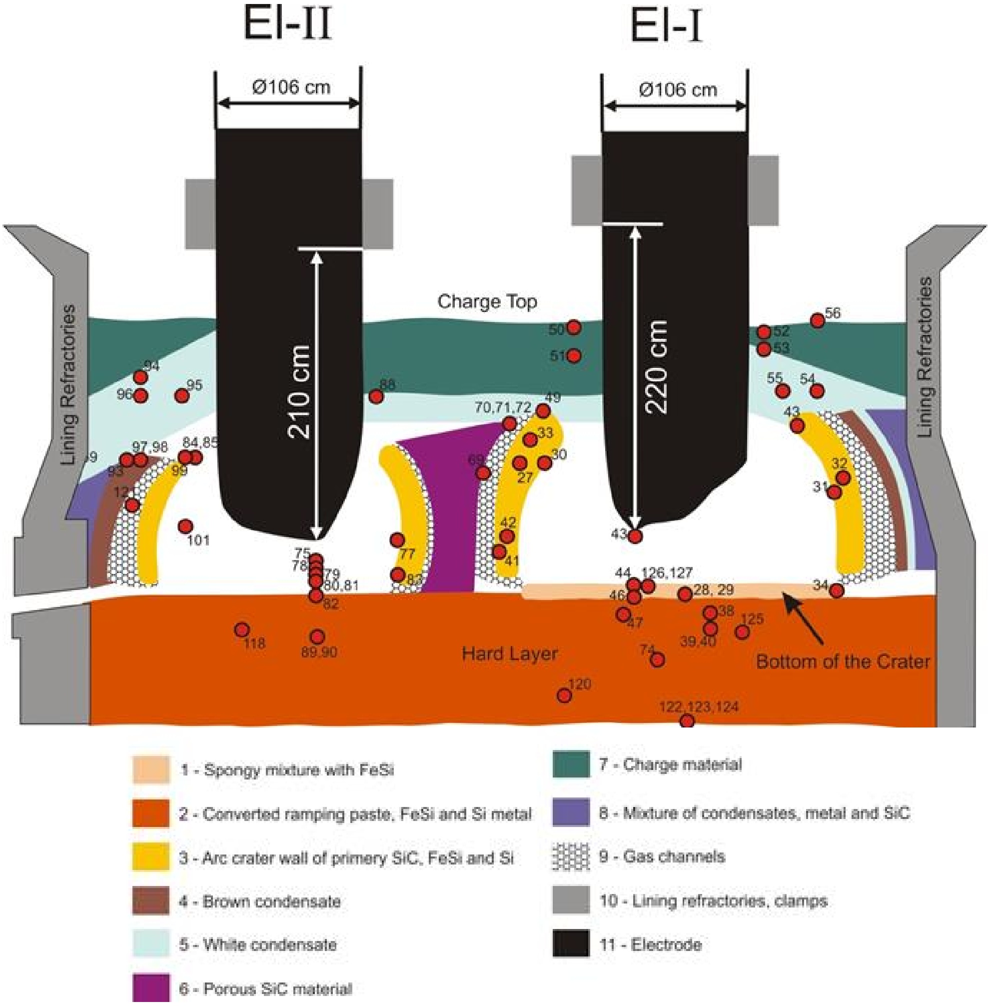

Figure 5. Recreated cross section of Finnfjord furnace excavation and various samples and zones. Used with permission from [23] [24]

Tangstad et al took part in the excavation of a **40 MW Si furnace at Thamshavn** in 2013 [24] [25]. They divided the furnace into 4 SiC zones based on the structure and composition of the SiC crust (also called black SiC), which comprised almost half of the furnace space. This is shown in Figure 6. The first zone, moving from the outside of the furnace in, was classified as inactive. The second zone contained a condensate layer on top, a mixture of slag and SiC on the bottom before reaching the lining, and a large portion of black SiC in the middle. Zone 3 follows the electrode track and saw a layer of charge and a thinner layer of condensate before reaching the black SiC. The fourth zone in the area in the center of the furnace, which contained thin layers of charge and condensate, but mostly black SiC.

This excavation showed the structure of both α-SiC, also called black SiC or high temperature SiC, and β-SiC, produced from carbon materials as well as found in the slag and condensate layers. β-SiC is also called green SiC. The condensate consisted of SiO_2 mixed with SiC (green). Si drops were seen in the brown condensate that agree with Vangskåsen's pilot scale findings [26]. SiO gas condensate was also found during the experiment in needle shapes. SiC was found from both condensate formation and the conversion of carbon materials, where the pores are filled by Si. A slag/SiC layer was found where the green material was slag and gray areas were SiC. Some samples also contained Si. The slag consisted of CaO, Al_2O_3, and SiO_2 intricately mixed in SiC. In other areas, SiC/slag mixtures with more Si were found and did not share the same green coloring.

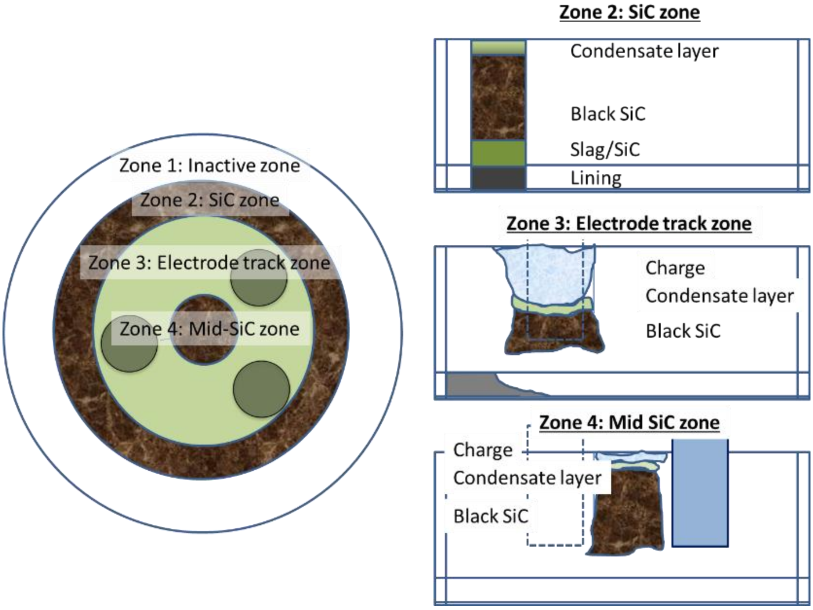

Figure 6. The divided zones of a 40 MW Si furnace at Thamshavn, used with permission from [24]

In an excavation done at **Bjølvefossen on an 18 MW FeSi50 furnace** [22] [25], no cavity was found, and slag had filled the furnace to the top with a lot of loose charge around the electrodes. This is seen in Figure 7. The excavation was divided into two zones based on the relation to the electrode track. Within the electrode circle, the furnace resembled a coke bed instead of a cavity as would be expected. As a result, little condensate was found. Outside the electrode track there was a large amount of slag containing SiC particles. No major areas of SiC crust were found.

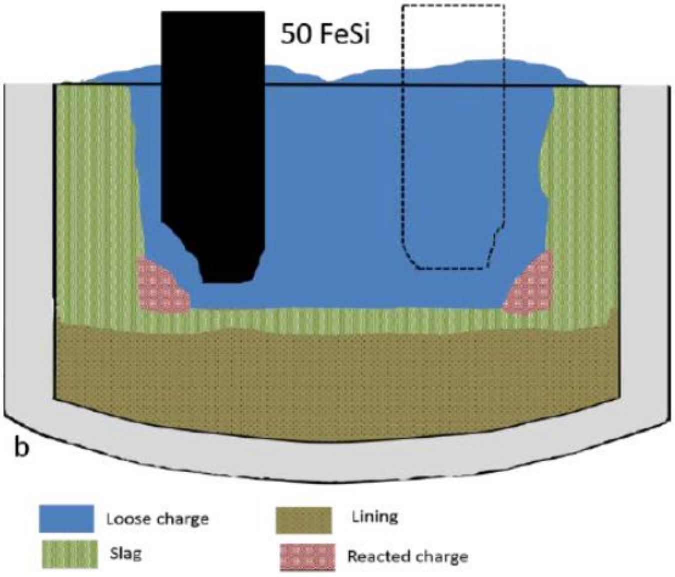

Figure 7. Recreated schematic of the cross section of the excavation of 18 MW FeSi50 at Bjølvefossen, used with permission from [25]

In an excavation done on **Wacker furnace 4** [22] [27], a 33 MW Si furnace, loose SiC, quartz, and slag were found in major areas of the furnace. No cavity was observed as there was a large inactive zone with slag lining the edges of the furnace and a very small amount of SiC crust. The excavation divided the SiC into four categories: the SiC crust, SiC formed from carbon material, SiC-slag layers, and SiC condensate layers. Imaging confirmed that the SiC crust has large smooth areas of SiC with Si present. There was also a layer of SiC containing some silica along with silicon droplets. The cross section and labelled areas can be found in Figure 8. In retrospect one would maybe not call the SiC-crust part a crust today, as the material was small particles and not a crust as such.

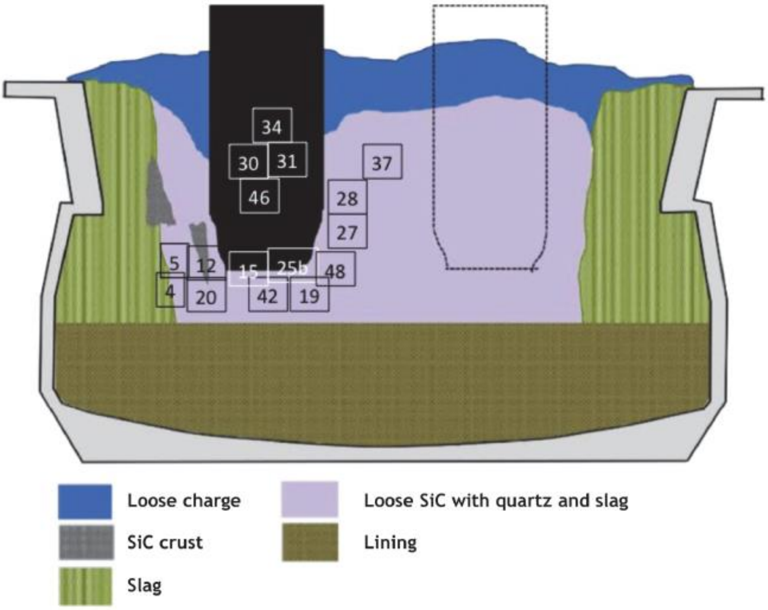

Figure 8. Recreated cross section of the Wacker 4 excavation with labels of sample locations, used with permission from [22] [27]

In an excavation done on **Wacker 1** [22] [25] [27] a 13 MW Si furnace, there was a large inactive zone with slag lining the furnace all the way to the top and a very small cavity. This is shown in Figure 9. However, there was a large pool of SiC with Si. Additionally, in this excavation the electrode tip was very high in the furnace. The excavation did not find any SiO_2/SiC condensates, but rather found coarse SiO_2 enveloping SiC, which was speculated to not be condensate due to the texture. It also showed partly reacted materials from samples taken specifically along the electrode track. Close to the electrode towards the top of the electrode holder, unreacted quartz and carbon material were found. The smooth surface of the quartz indicated that it had been softened or melted. The coal was found to be contaminated by a small amount of slag. Further down, more unreacted coal was found, but as samples were taken deeper in the furnace, the outer area of the particle had been converted to SiC with an unreacted carbon core. This confirms that in this area of the furnace, temperature and SiO pressure were substantial enough to begin converting the carbon to SiC. At the same level SiO_2 was also found, but it was not clear whether it came from quartz directly or through condensation reactions.

Charge and SiC intermixed with condensate was found further down along the electrode track. The composition of the condensate was SiO_2 with Si particles, which was similar to the brown condensate in Wacker furnace 4 and in Vangskåsen [26] and Tangstad's [25] work. SiC that had been converted from coal was also found at this level. Samples at this depth saw SiC along with charge and condensate. It was assumed that the condensate was brown condensate. Directly beneath electrode 3, large particles of Si and some SiO_2 and SiC were found. Within the SiO_2, more Si was also found and appeared to be accumulating within the matrix. A SiC crust similar to that seen in Wacker furnace 4 consisting of Si and SiC was also found with a layer of SiO_2 on top. More SiC from converted coal was also seen at this level, along with larger separate areas of Si consistent with a silicon pool from the silicon producing reaction in the furnace. Midway between electrodes 1 and 3, porous SiC from coal was found due to the formation of gas channels of SiO and CO in this region.

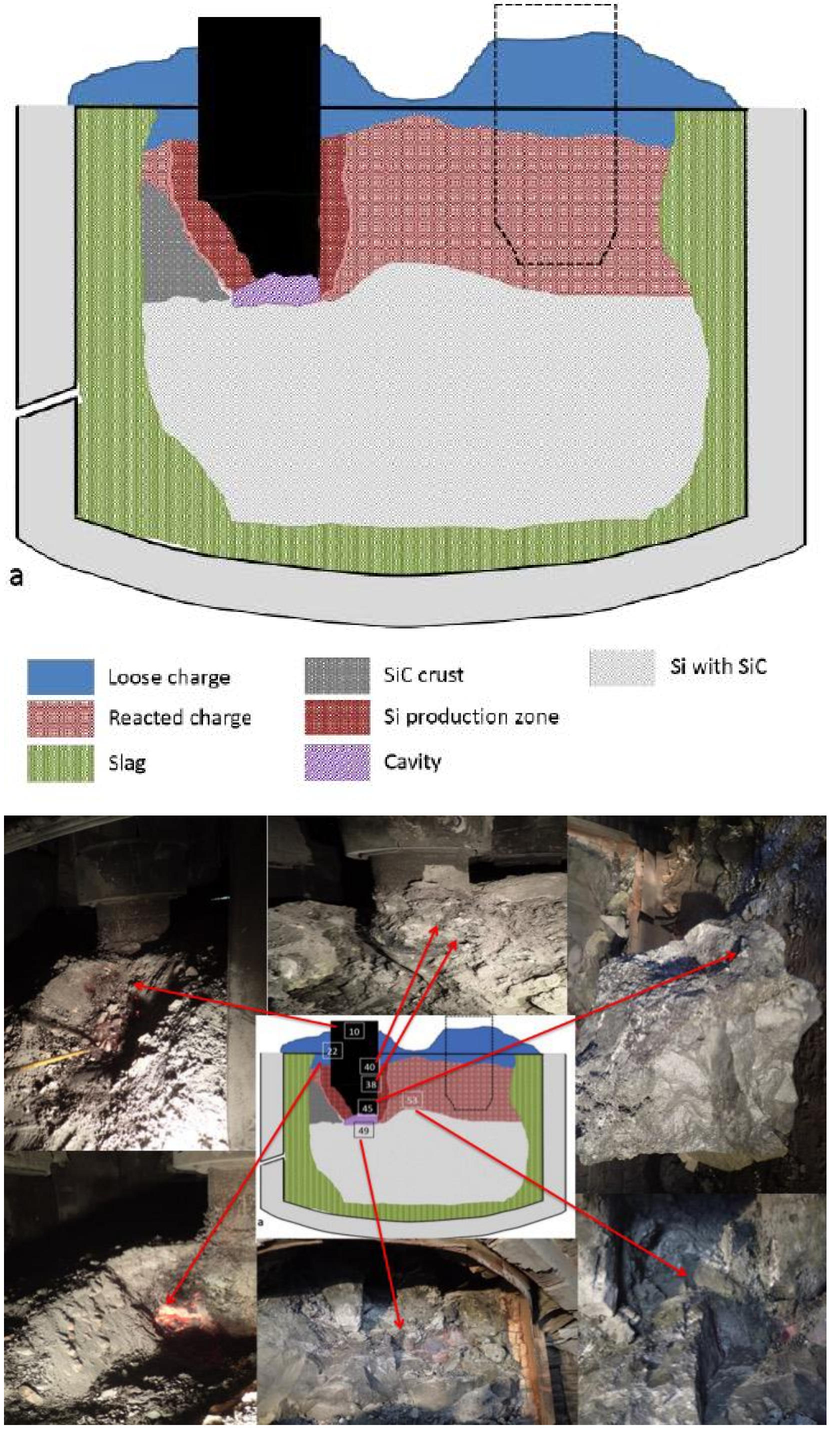

Figure 9. Recreated cross section of Wacker 1 excavation (top) with physical pictures and sample areas labeled (bottom), used with permission from [22] [25] [27]

In the excavation done by Ksiazek at **Elkem Salten** [24] [25], no crater or loose charge was found. There was also little slag and SiC crust and the majority of the furnace consisted of reacted charge with a heap of SiC and Si in the center, with charge and condensate mixtures lining the outer edges. Some quartz was found, and a hard layer of condensate was observed. The quartz contained some cracks but held its original shape according to the SEM images, which aligned with visual observation of the sample. Another sample from this region showed areas of SiC and SiO_2 mixed. From the hard layer covering the furnace a mixture of mainly SiO_2 with MgO, K_2O, CaO, Al_2O_3, and FeO was found. Partly reacted material was also found behind the condensate layers in the direction of the electrodes. This is shown in Figure 10.

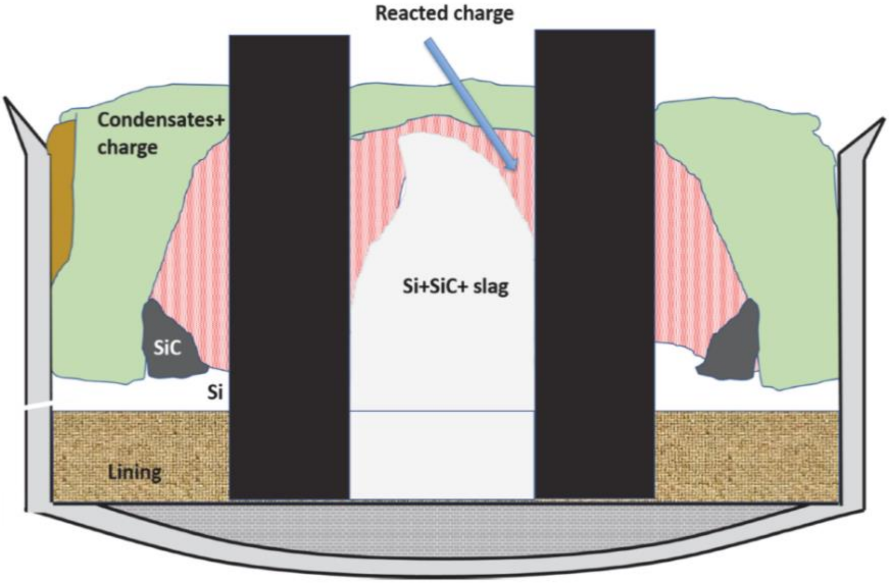

Figure 10. Recreated cross section of the excavation at Elkem Salten, used with permission from [24]

During the excavation of **Finnfjord furnace 2** [24] [25], six samples from underneath the electrode in the silicon/slag pool were analyzed. This is shown in Figures 11 and 12. They found slag of various compositions and SiC particles of various sizes along with the silicon. The samples were assumed to have been liquid in the furnace. Additionally, three samples from the SiC layer were taken for analysis. The samples were porous, and it was found they contained both α-SiC and β-SiC. In the case of of β-SiC, they could see the original structure from the carbon material. In contrast, the α-SiC is a dense matrix that contains silicon droplets.

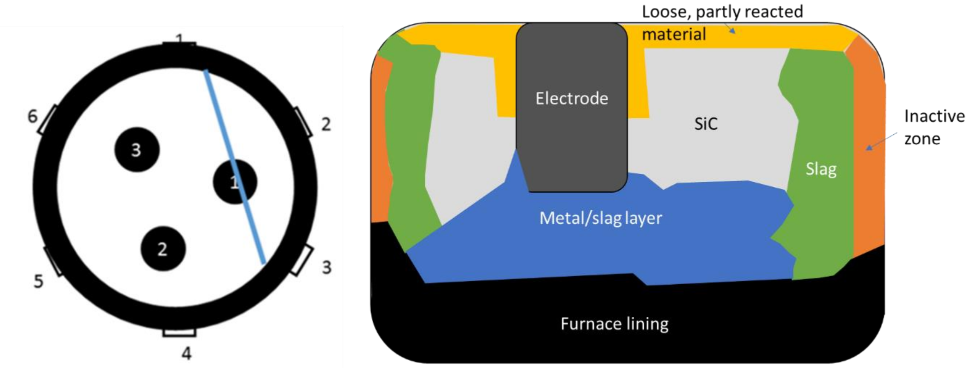

Figure 11. Recreated cross section of the excavation from Finnfjord 2 and where the cross section lies in the furnace, used with permission from [24] [25]

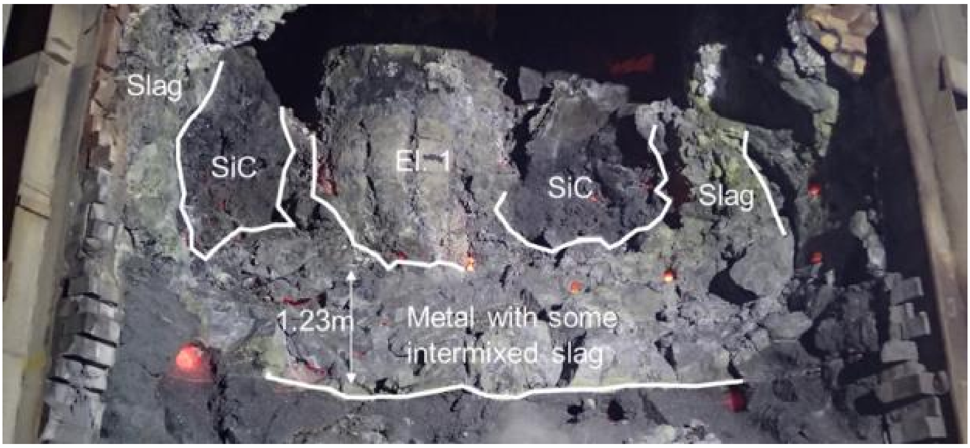

Figure 12. Zones in the Finnfjord 2 excavation, used with permission from [17]

Myrhaug excavated a **150 kW pilot scale Si furnace** in 2003 [28]. Samples were divided in the furnace into 10 zones, (Figure 13) which will be summarized here. The first zone (light yellow) was Si with precipitated SiC that describes the silicon pool below the electrode. The Si had leaked into the carbon lining and the slow cooling of the furnace had allowed SiC crystals to form in the carbon saturated Si. Additionally, impurities formed silicides on the grain boundaries. Zone 2 (orange) describes the area just above the lining, where a matrix of SiC crystals were found with Si filling the pores. The SiC was believed to be precipitated as it did not resemble the original carbon material in the charge. Zone 3 (yellow) was the 1-3 cm thick crater wall consisting of coarse SiC with some Si. Moving further up in the furnace is zone 4 (brown), which was classified as a mixture of SiC, SiO_2, and Si. The SiC was green in color and converted from the charcoal. The SiO_2 was from both molten quartz and condensate, the form appearing as gray and glassy, and the condensate being brown. Additionally, Si could be seen partially enriching areas of both the condensate and the SiC particles. Zone 5 (green) consisted of a mixture of partly converted reduction materials. Additional green SiC was seen as well as additional quartz that may have softened, but not yet melted fully. Zone 6 (turquoise) was the top of the charge with SiO condensate which contained mostly unreacted charcoal, quartz, and brown condensate which glued the materials together. Additionally, the woodchips that were added were converted to charcoal with no way to differentiate between them and the added charcoal. In zone 7 (blue), which is near the refractory lining and away from the active zone, was inactive charge. In addition to the charge mix, a small amount of brown condensate and melted quartz were found. The final material zone was zone 8 (pink) which contained fallen quartz from the top of the charge during the final shut down. Zones 9 (gray) and 10 (black) were the refractory lining made up of Al_2O_3 and the electrode, bottom lining, and taphole.

Myrhaug's results also show the presence of two cavities, one around the electrode tip, and another higher up in the furnace held together by the condensate layer. The presence of two cavities rather than one was also seen in laboratory scale silicon furnace experiment by Tangstad et al. [29].

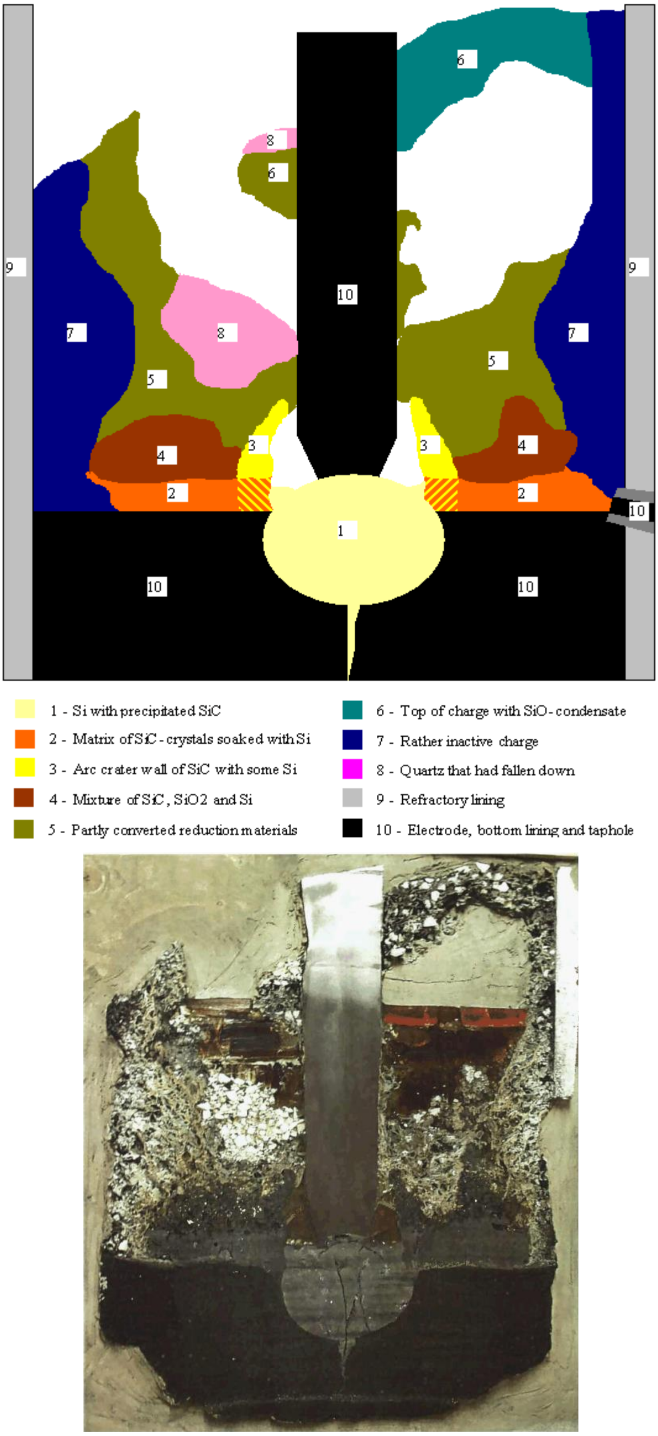

Figure 13. Recreated cross section with various materials (top) and a picture of the cross section (bottom) from Myrhaug's pilot scale excavation, used with permission from [28]

In a **160 kW Si pilot experiment** excavated by Vangskåsen [26] 17 samples were taken in the area between the electrode and the lining. His focus was on the formation of condensates and the silicon producing reaction mechanisms. Quartz melted below sample 2 in Figure 14. Near the top of the furnace, above the cavity, brown condensate was stuck to quartz and carbon particles. Brown condensate is the name for condensate that consists of Si in an SiO_2 matrix [30]. The condensate found in the cavity side walls (5-12) contained the same phases as the brown condensate but was paler in color and less homogeneous. The Si in this region was also more round in shape and was expected to accumulate and flow deeper into the furnace. However, Si was found as high as position 5. Samples 13 and 14 represent the silicon pool below the electrode, which consisted of mainly silicon with some SiC. Sample 14 is slightly darker in color and contained a higher amount of SiC. It was believed that the furnace was undercooked, causing SiO gas blows that periodically raised the temperature in the upper part of the furnace.

Vangskåsen also divided the cross section into zones shown in Figure 14. In zone 1, which is the area above the cavity, the charge is consumed from the bottom up, and the condensation of SiO gas forms a cavity roof that is stoked and sends additional charge deeper in the furnace. Zone 3 is the area around the electrode in the so called “hot zone” which will consume charge in the direction of the arrow shown on the figure. Zone 2 is towards the outer edge of the furnace and represents the inactive region of the furnace. Temperature tends to be lower in this region due to the gradient, but SiO gas will still condense and form a crust containing condensate, quartz, and carbon that will make up the hard rooftop of the furnace. Zone 4 is the liquid silicon and slag bath region.

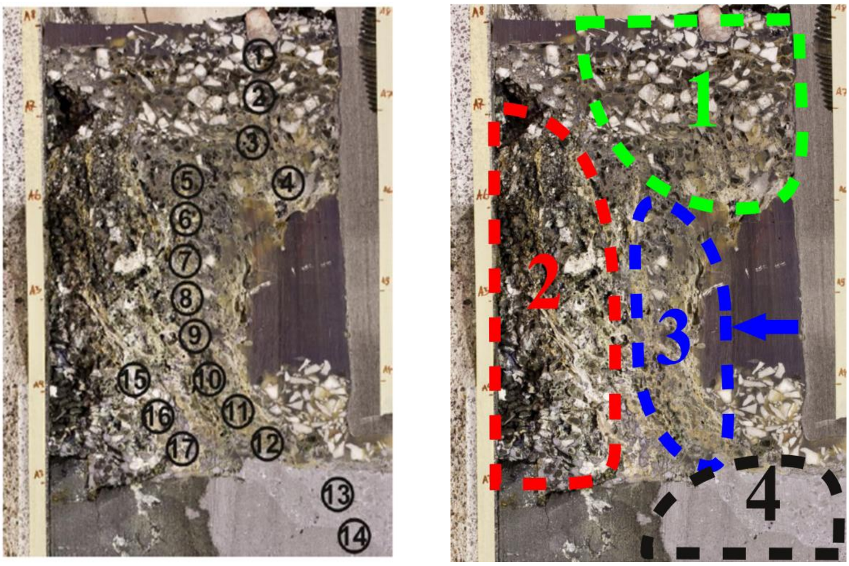

Figure 14. Left side cross section of the pilot scale furnace with sample locations labeled (left) and zones labeled (right) from Vangskåsen's pilot scale experiment, used with permission from [26]

2.3 SIC FORMATION

Silicon carbide is an important intermediate in the silicon production process because it takes part in the silicon producing reaction and it's alpha polytype forms a significant portion of the cavity wall, also known as α-SiC crust or black SiC [31]. Silicon carbide is known for its ability to resist oxidation, retain strength at high temperatures, resist wear, conduct heat, and resist thermal shock [32] [33] [34]. Silicon carbide has a number of polytypes, however the most relevant for studying the silicon furnace are the cubic form (3C) often simply referred to as β-SiC, and the non-cubic form (2H, 4H, 6H) referred to as α-SiC [35]. The β-SiC structure forms first in the silicon furnace. However, α-SiC, which forms at temperatures over 2000 °C, and liquid silicon together make up a highly conductive SiC crust or cavity wall. SiC has a melting point close to 3000 °C [36], so it will remain solid in the silicon process.

The SiO reactivity test is used to quantify the ability of a carbon material to capture SiO gas and form SiC. It is used as a parameter in evaluating raw materials because a high SiO reactivity will minimize Si losses in the industrial furnace. There are various ways to measure the SiO reactivity from 1 particle at a time to test where a higher amount of SiC is produced [37]. The most used test industrially is the SINTEF-reactivity test. SINTEF developed a test procedure for small amounts of carbon materials for the industry. The apparatus used for the SINTEF-test is shown in Figure 15. An SiO generator produces known amounts of SiO and CO gas from pellets of SiO_2 and SiC at 1650 °C. A carrier gas is used (usually argon) to blow the gas mixture upwards through the reaction chamber containing carbon material. The SiO will react with the carbon to form SiC and CO gas according to Equation 3, and the amount of SiO gas that passes through the chamber unreacted is defined as the reactivity. Therefore, a low amount of SiO gas losses equates to high reactivity of the carbon material as it can produce higher amounts of SiC. The SiO reactivity of some common carbon materials is shown in Figure 15, where charcoal has the highest SiO reactivity, while cokes are on the lower end of the spectrum. Furthermore, if all the SiO gas is captured, the off gas would contain 18 % CO gas and if none of the SiO gas is captured, it will contain 6 % from the SiO generation [38].

SiO reactivity is also measured in other apparatus, such as Ramas [39], Norbø [40], and Jayakumari [41] who investigated the SiO reactivity in two-layer crucibles, where the SiO forming pellets were in the lower layer, while carbon materials rested either on the pellets or on a porous disc. When larger amounts of SiC are needed, one can also perform it on a larger scale previously reported by Jayakumari [41].

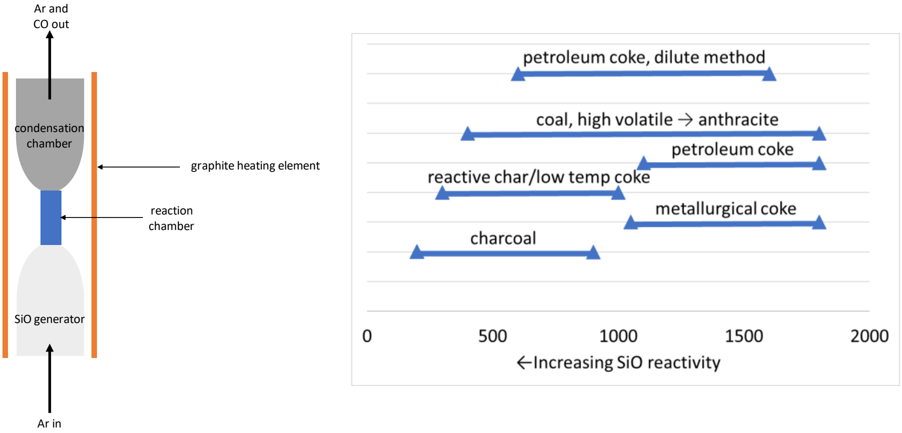

Figure 15. Illustration of the SiO reactivity test (left) and the SiO reactivity of various carbon materials (right) from SINTEF [35]

The shrinking core model (SCM) can be used to characterize a gas/solid reaction in which the reaction occurs at a boundary layer that expands into the particle. As the reaction proceeds, a product shell is created, and the original solid becomes the “unreacted core” of the overall particle. The particle could be subject to changing size depending on the densities.

The following steps are the process according to [42] and they are illustrated in Figure 16:

1. Mass transfer of reactant in the bulk gas phase and gas film boundary layer
2. Diffusion of gas reactant through product layer. As the product layer expands, the reaction will depend on gas diffusion through said layer to reach any remaining core.
3. Chemical reaction at unreacted core forms product layer (with any chemical reaction steps)
4. Diffusion of gas product through product layer
5. Mass transfer of gas product in the gas film layer and bulk gas phase

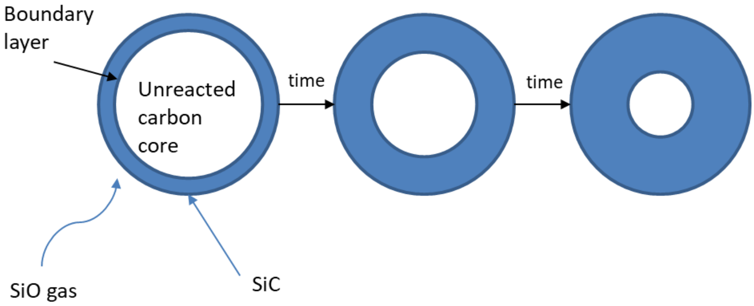

Figure 16. Illustration of the process steps of the shrinking unreacted core kinetic model, where the reaction occurs at a boundary layer that expands into the particle and over time the original particle shrinks to an unreacted core.

Myrhaug [43] modelled the SiC formation reaction using the SCM and found it to be a good fit with both thermogravimetric methods (TGA) on one particle and the SINTEF SiO reactivity test. As such, the rate of conversion is dependent on the chemical reaction at the surface, diffusion of product gas through the product layer, and on external mass transfer. The following assumptions were made by Myrhaug et al. [43]:

- The chemical reaction occurs on the thin layer of unreacted core that has a radius r_c
- The particles are spherical with a radius of r_p

- The reaction is first order
- Pseudo-steady-state approximation is used, where no gas species accumulate in the product layer and there is equimolar counter diffusion
- Particle volume is not changed
- No temperature gradient exists between the gas and the particle or within the particle itself

Similarly, Abolpour and Shamsoddini [44] studied the kinetics of SiO_2 and carbon powders to produce SiC at 1293-1660 °C using TGA. They found that above 1477 °C the controlling step of SiC formation to be the diffusion of SiO gas through the carbon particle. They verified the reaction to be first order in this temperature range and that it approximately follows the 3D diffusion mechanism. They also determined that CO and CO_2 did not affect the formation of SiC at temperatures above 1200 °C and therefore SiC may only be produced through solid carbon reacting with a silicon containing species. Based on the work of Jayakumari [41] using carbon particles with some porosity, a proposed mechanism for the formation of SiC is shown in Figure 17, where SiC will form on the edges of the particles and around the pores according to the SCM. As the reaction progresses and a layer of SiC is formed on the outside of the particle, Si may begin to form via Equation 4 in the pores of the particle.

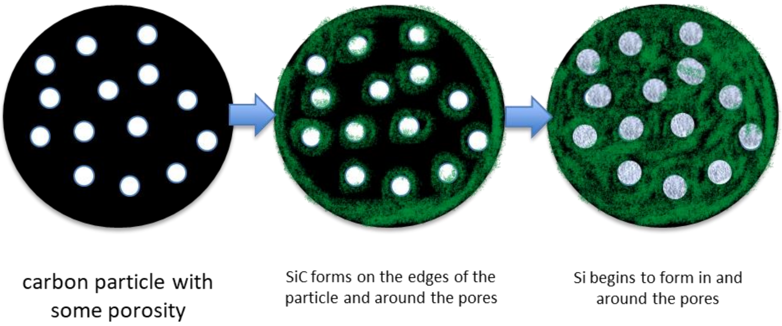

Figure 17. Example of proposed mechanism for SiC formation in a carbon particle with some porosity via Equation 3 and the formation of Si in the pores via Equation 4.

The grain model is also used to characterize gas-solid reactions, usually when the solid is porous and therefore the boundary between the product and the unreacted core is not as sharp. In this case, the particle is composed of individual grains. Depending on if the reaction is chemical reaction controlled, diffusion controlled, or a combination of both, three cases can occur, summarized well by Myrvågnes [37]. In the chemically controlled case, the concentration of the gas is uniform across the particle and each grain acts like its own shrinking core. In the diffusion-controlled case, the gas is the limiting factor and thus the reaction occurs at a narrow zone, where some grains are transformed into the product and others are not because the gas has not reached them. This case resembles the shrinking core model. Finally, if the reaction is both chemical and diffusion controlled, both are occurring at the same time. This leads to a particle that has grains on the outer edge of the particle that are transformed, an area in between that is partially transformed, and an area in the middle where the grains are not transformed.

2.4 CARBON MATERIALS IN SI PRODUCTION

Carbon is the main reductant in Si production as well as an energy source. For silicon production, the source of carbon in the charge material is usually a mix of coal, coke, charcoal, and woodchips. The properties of these materials, for example the fixed carbon content and amount of volatiles, can have a significant effect on the operation of the furnace including the power consumption [45].

Coal is formed from the decay of organic matter over millions of years. As decaying matter is exposed to heat and pressure for long periods of time, a complex set of chemical reactions result in the high carbon content substance recognized as coal [46]. Coal is loosely defined to contain 50 % organic matter by weight [47]. Ash are the materials in coal that are considered noncombustible. If the ash content of a substance is too high (above 50 %wt), it would be classified as carbonaceous shale. The four coal ranks are anthracite, bituminous, sub-bituminous, and lignite. Anthracite is the highest rank coal and has the highest carbon content. However, it tends to be less widely available than other forms of coal, thus it's use is mainly limited to the metallurgical industry. Bituminous coal is the most abundant type of coal, and still has a high carbon content. It is used for both electricity generation and industrial processes. Subbituminous coal is almost as abundant as bituminous coal, however due to its lower carbon content, it tends to only be used for electricity generation. Lastly, lignite is the lowest rank of coal. It has the lowest carbon content, lowest energy content, and high moisture content. Though not widely mined, the lignite that is produced is used for electricity generation through combustion or through conversion to synthetic natural gas [48].

The type of coal needed to fulfill each of these purposes is based on coal grade, not to be confused with coal rank or coal type. Coal grade is “an economic or technological classification of the relative quality of the coal for a particular use” [47]. Coal grade is commonly referring to the ash content of the coal as it will affect for what purpose the coal can be used [37].

Metallurgical coal is mainly used for producing coke but is also an important raw material in many industrial processes including silicon production. Metallurgical coal is usually low in sulfur (less than 1 %), low in ash (less than 10 %) and low in volatile matter (20-30 %). Elemental analysis is necessary for metallurgical coal to determine if there are any trace elements that could interfere with the process. Given these requirements, high grade metallurgical coal is often medium-ranking bituminous coal.

Metallurgical coke is made from heating coal in the absence of oxygen to remove volatiles and tars. The resulting coke has a higher fixed carbon, lower volatiles, and different mechanical properties compared to the original coal. The coking process usually goes up to around 1000-1200 °C [49]. Semicoke, or char, is made at a lower temperature and typically with a lower grade coal [50].

Charcoal, in contrast to coal, is gaining in popularity because it is more carbon neutral and can be made from readily available and sustainable materials [51]. In essence, the charcoal production involves wood undergoing heating to increase the carbon content and calorific value. This process is known as carbonization, which is a more specified form of pyrolysis and involves the breaking down more complex substances, in this case wood, into their simpler components. While the carbonization step may only account for around 10 % of the total costs for production of charcoal (from tree growth to delivery) it remains the most important step because it determines the yield and quality of the product [52].

Shown in Figure 18 are the steps for charcoal formation. The starting material is dried wood. The drier the starting material, the better the yield as this minimizes the endothermic first step of the process. In warm, dry areas, the sun usually provides adequate drying without external assistance and with minimal losses, but in colder or more humid areas, this is a relevant concern. Once dried, the process is carried out in confinement to avoid combustion of the material. The main product is of course the charcoal, which consists primarily of elemental carbon. Ash originating from the wood source and tar make up the remainder of the charcoal. Charcoal has been shown to be an effective reductant for production of silicon and silicomanganese [10] [53]. However, its low mechanical strength poses a challenge as the creation of fines will negatively affect the permeability and gas flow in the furnace [54]. Typical compositions of carbon materials used in Si production are shown in Table 1 [28].

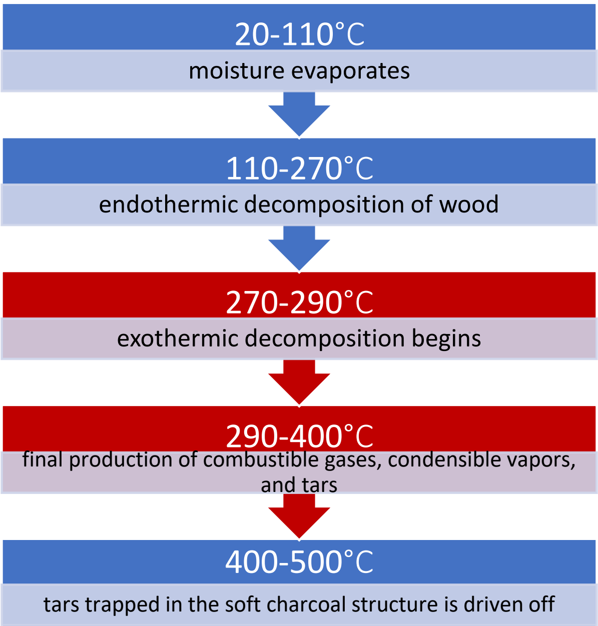

Figure 18 Steps of charcoal formation [52], endothermic steps are blue, exothermic steps are red.

Table 1. Typical compositions of various carbon materials, from Myrhaug [28]

	Coal	Coke	Charcoal	Woodchips	Petroleum coke	Electrodes
Fixed carbon	39-62	81-95	75-85	20-26	88-93	85-99
Ash	1-5	1-10	0.5-10	1-10	0.05-1	0.1-5
Volatiles	34-58	2-5	10-25	70-75	7-12	1-10
Si	0.3-2	0.6-4	0.05-9	0.2-1		
Al	800-5700	1000-10000	100-6200	<50-100	70-110	<50-4000
Fe	700-5200	1400-9000	100-1700	<100-1400	<100-600	100-3500
Ca	150-2400	600-3400	1000-4000	600-1000	<75	200-1500
K	<75-1800	300-1800	100-1800	250-900	<75	<75-210
Mg	80-1100	300-1400	200-1100	75-200	<15-100	<15-500
Na	<320	230-2100	170-230	<50-130	<50-110	<50-300
Ti	50-600	60-4000	10-300	~1	<0.5-50	~100
P	<5-143	16-160	80-300	20-110	<5-13	<5-170
S	1200-8300	330-11000	200-1500	100-1300	20000-50000	55-3400

(< denotes sample is below detection limit)

2.5 SILICA

Silica refers to silicon dioxide, or SiO_2, and provides the source of silicon in silicon production. While several polytypes exist, quartz is the most common polytype found in nature because it is the most stable at ambient temperature and pressure. Quartz used in Si production normally has high purity, with contaminants on a ppmw level. Some typical impurities and their amounts are shown in Table 2 [28].

Table 2. Typical impurities found in quartz used in Si production, from Myrhaug [28]

Element	Amount (ppmw)
Al	300-3200
Fe	100-1500
Ca	<75-160
K	<75-1700
Na	50-170
Mg	20-140
Ti	20-200
Mn	3-600
P	<5-50
S	<5-1400

(< denotes sample is below detection limit)

Quartz will undergo thermal degradation to some degree at high temperatures. This is undesirable for furnace operations since the available surface area will change, thereby effecting the chemical reactions and temperature distribution. Jusnes [55] studied thermal degradation of several types of quartz and found that factors such a grain size and preexisting cracks can influence the degree of degradation.

2.6 RESISTIVITY

Resistivity (ρ) is an intrinsic property that relates the current and voltage over a given area and it is the mathematical reciprocal of conductivity. It can also be expressed as a function of its resistance (R) over a given area(A) and length(L) [56]. The general equation is shown below (Equation 8). As with resistance, it is temperature dependent and sensitive to impurities as well as particle size and volume. In studying resistivity of mixed materials, it is important to further differentiate between material resistivity, contact resistance, and bulk resistivity [6]. Bulk resistivity refers to a bed of particles, and it is the combination of both material and contact resistivity. Material resistivity refers to the intrinsic resistivity value of a given material. Contact resistance refers to the resistance that arises from current passing through points of contact between particles. Contact resistance is believed to largely contribute to bulk resistivity as the area of contact connecting the conducting particles will greatly affect its ability to conduct charge [6].

$$\rho = \frac{RA}{L} \tag{8}$$

Many studies have been published on the resistivity of carbon materials, with various trends and conclusions that are summarized well in Eidem's PhD thesis [6]. In general, it is accepted that resistivity decreases with increasing temperature for the materials in the Si/FeSi furnace. It can however be mentioned that for metals the resistivity increases with temperature [57]. The effect of particle size may also be an important factor. Tangstad et al [54] argue that the effect of smaller particles having more contact points and thus more possible current paths is cancelled out by having more contact resistance between the particles. However, they reasoned that the smaller particles will be less porous, but the larger particles will have greater contact area and thus lower bulk resistivity. Current in the charge conducts through an array of conducting particles in the bulk and contact resistance decreases with increasing temperature and contact pressure. Volatiles in carbon materials were seen to increase resistivity. Heat treatment and increasing graphitization decreased the resistivity if the current was measured parallel to the carbon layers. More recent studies build on these trends [4] [5] [7] [8].

2.6.1 Material resistivity

Material resistivity refers to the intrinsic ability of a material to conduct current. In practice this means the resistivity of a single particle of the material, thereby excluding the effects of contact resistance or particle size. Eidem [6] tested the material resistivity of three metallurgical cokes from room temperature to 1600 °C and found that over 1000 °C the decrease in resistivity was moderate and there was no statistical difference between the three cokes. At 1600 °C the resistivity was 0.13-0.15 mΩm. Graphite, used as a reference was 0.0086 mΩm. Anthracite was also found to have a moderate decrease past 1200 °C and at 1600 °C had a resistivity of 0.485 mΩm.

Cromarty et al [5] studied the material resistivity of cylinders of five different cokes from room temperature up to 1600 °C and found similar trends to other carbon materials. They also concluded that the type of coal used to make the coke had a greater effect on the resistivity compared to other cokes than the temperature. Four out of the five cokes tested had a resistivity of less than 0.2 mΩm at 1600 °C and were not very sensitive to temperature. The fifth coke was made of a lower rank of coal and thus had higher resistivity over the entire temperature range (approximately 1 mΩm at 1600 °C).

Bharat [4] studied the effect of increasing heat treatment temperatures and residence times of two different types of charcoal. They found that increased heat treatment temperature decreased the resistivity at room temperature for both charcoal types. The residence time had little effect compared to temperature. Furthermore, they found that there is a small difference in the resistivity if the charcoal was measured perpendicular or parallel to the wood grain, but this effect was lessened at the high treatment temperatures.

Krokstad [3] measured the material resistivity of industrial α-SiC crust samples and compared it to commercial samples found in literature up to 1600 °C. The review of materials is summarized in Figure 19. He found that industrial α-SiC crust had a resistivity in the range of 1-10 mΩm at 1600 °C. The SiC crust had a higher resistivity than both liquid Si and the more conductive grades of commercial SiC and had a lower resistivity than a cokebed. Krokstad also found that even though there were large variations in composition in the SiC crust samples, the differences in resistivity were not significantly affected at high temperature. He believed that increased silicon content and the state of the silicon (liquid) had the potential effect of lowering the resistivity, but believed additional investigations were needed to confirm the trend. Though not investigated directly in his work, he also speculated that the effect of porosity was significant, particularly at lower temperatures, and could account for the large ranges in resistivity of the material.

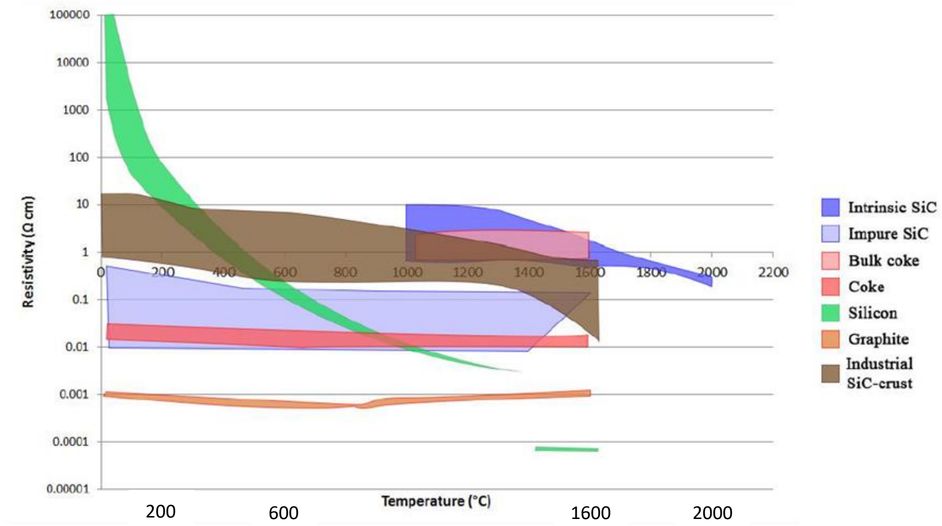

Figure 19. The material resistivity of materials used in the silicon furnace from Krokstad's MSc Thesis work [7]

Table 3 shows a table of the various values found in literature for the material resistivity of carbon and SiC materials. Some units have been converted for clarity.

Table 3. Material resistivity values of various relevant materials from literature

Material	Temperature	Resistivity	Particle type
cokes (3) [6]	1600 °C	0.13-0.15 mΩm	Cylinders (30 mm diameter, 24 mm height)
graphite [6]	1600 °C	0.0086 mΩm	Cylinders (30 mm diameter, 24 mm height)
anthracite [6]	1600 °C	0.485 mΩm	Cylinders (30 mm diameter, 24 mm height)
cokes (A-D) [5]	1600 °C	>0.2 mΩm	Cylinders (1.5 mm diameter, 40 mm height)
coke E[5]	1600 °C	1 mΩm	Cylinders (1.5 mm diameter, 40 mm height)
industrial SiC crust [3]	1600 °C	1-10 mΩm	Cylinders (2-3.5 cm diameter, 1.8-6.5 cm height)
Si [58]	1000 °C	0.1 mΩm	2x2x100 mm filament
Si [58](near melting)	1400 °C	0.05 mΩm	2x2x100 mm filament
liquid Si [59]	1600 °C	0.0007 mΩm	molten
commercial SiC [3]	1600 °C	1-1000 mΩm	
iron [60]	1600 °C	0.0013 mΩm	molten
α-SiC [61]	950 °C	0.8-1.4 mΩm	tube heating elements
β-SiC [61]	800 °C	0.15 mΩm	tube heating elements
(α+β)-SiC mix [61]	950 °C	1-1.6 mΩm	tube heating elements

2.6.2 Contact resistance

Contact resistance refers to the resistance that arises when two particles are in contact with one another. Metal contact theory is used to describe and predict what will happen to carbon materials in the SAF as it is believed to be analogous [6]. Metal contact theory explains that when two particles are in contact there is an apparent contact area, but due to the uneven surface of the particles a smaller area is in mechanical contact, and of that area, some are in electrical contact. This is illustrated in Figure 20. However, assuming there is no insulating layer due to oxides, such as ash, the mechanical contact area should be equal to the electrical contact area.

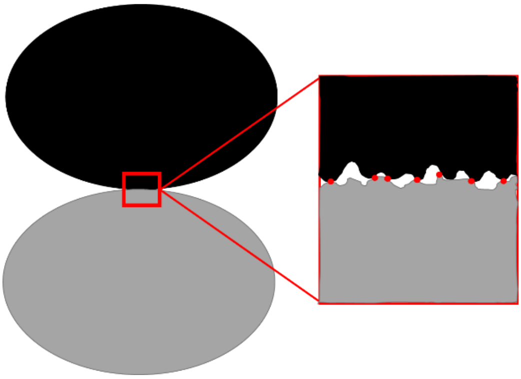

Figure 20. Example of apparent contact between two particles and the mechanical contact due to uneven surfaces on the microscopic level.

Sørlie and Gran, as reported by Schei et al [2] found that contact resistance decreased with increasing temperature and contact pressure using steel and carbon in contact at 975 °C. The resistance decreased from 350 µΩ to 28 µΩ as the contact pressure was increased from 0.1 to 10 MPa. Eidem also measured the contact resistance for metallurgical cokes with increasing temperature from room temperature to 1600 °C and also found that it decreases with increases temperature. When compared to the total resistance, contact resistance accounted for 70-95 % at lower temperatures and decreased to 50 % at 1600 °C. He argues contact resistance is a major component of the total resistance, but its contribution decreases with increasing temperature because the increased temperature compensates for the added energy band gap. The resistance of two half spheres at 1600 °C was between 52 and 106 mΩ for the cokes. Half spheres can be assumed to mimic the minimum possible point of contact between two particles. When compared to the other shapes and contact areas tested, which can be seen in Figure 21, this shows that increasing the contact area decreases the contact resistance due to increased points of electrical contact.

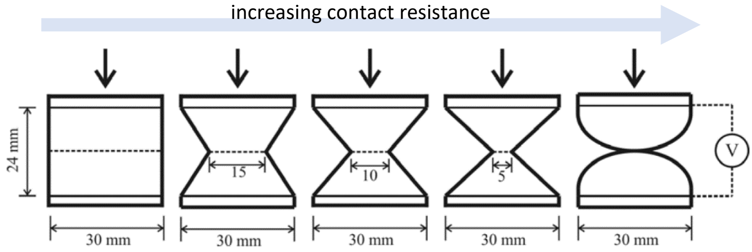

Figure 21. Decreasing contact area moving from left to right with increasing contact resistance as seen in Eidem's PhD thesis [55]

2.6.3 Bulk resistivity

Bulk resistivity refers to the resistivity of a bed of particles and is made up of material resistivity, contact resistance, and the geometry of the material. Usually, the bed is not homogeneous and there is a constant balance between the material resistivity, contact resistance, and geometry. For example, the current travelling through a bed of particles will follow many possible paths throughout, so long as it travels through a series of conducting particles. However, since the bed is likely inhomogeneous, this can lead to localized breakthroughs of the voltage [2]. While most setups are unique, there are general parameters used in previous studies that outline good practices for measuring the bulk resistivity. The main factors which must be considered according to Singh [62] and as explained by Schei et al. [2] are shown in Table 4.

Table 4. Best practices and considerations for measuring resistivity according to Singh *[62]* and Schei et al. *[2]*

Sample preparation	Simulate furnace conditions as much as possible
Appropriate choice of measurement method based on shape and nature of sample	Current likely passes through materials that are modified from reactions with other charge materials
Sample mount	Resistivity can depend on current density for some materials
Temperature control	Temperature should be uniform and independent of the current
Electrical contacts	Linear dimensions of sample should be 10x (at least) the dimensions of the largest particle
Input current	Distribution must be homogenous
Homogeneity	Voltmeter with a large internal resistance should be used to measure the voltage

The four-point method is commonly used to measure resistivity. The four-point method introduces a separate measurement circuit in addition to the current supply [63]. The use of a voltmeter with a large internal resistance (usually several MΩ) for the measurement circuit makes its current negligible. This essentially eliminates contact resistance between the sample and the electrical contacts. The resistance (R) is measured through the voltage drop (V), and from Equation 10 the bulk resistivity (ρ_{bulk}) can be calculated [6] where the area is (A) the height of the bed is (h) and the current is (I). As current is applied the voltage drop is measured over the distance between the conductors, also known as the height of the bulk. From there the specific resistance can be calculated via Ohm's law (Equation 9).

$$V = I \cdot R \tag{9}$$

$$\rho_{bulk} = \frac{V_{drop} \cdot A}{h \cdot I} \tag{10}$$

Eidem [6] measured the bulk resistivity of six metallurgical cokes, two charcoals, two anthracites, and three petcokes with particles sizes between 10-30 mm. The results confirm that the carbon materials decrease in resistivity as the temperature is increased from room temperature to 1600 °C. The cokes had the lower resistivity, between 4-14 mΩm at 1500 °C. The petcokes were between 8-20 mΩm and the anthracites were 9 mΩm at 1450 °C and 41 mΩm at 1400 °C. Charcoals had a bulk resistivity between 7 and 16 mΩm, at 1600 °C, though with different particle sizes. He argues that volatiles and variation in texture account for the differences. In addition, different particle size ranges were used to measure the bulk resistivity of the cokes and charcoal. For both materials, the bulk resistivity decreased with increasing particle size. He argues that the increased porosity in the larger particles lowers the mechanical strength, which leads to crushing of the material at the contact points, thereby increasing their electrical contact area and decreasing the contact resistance.

Nurmukhanbetov et al. [19] measured the resistivity of reductants in ferroalloy processes and found that they had similar resistivities between 700-900 °C. Over 1000 °C they saw cokes having a higher resistivity than char. At 1600 °C the cokes had a range of 20-36 mΩm and the char was 16.6 mΩm. The particle size was 3-6 mm.

Krogerus et al [64] measured the conductivity of metallurgical coke, char, and gas coke up to 1600 °C. For grain size 5-25 mm they found coke had the highest conductivity followed by the char and the gas coke. At 1600 °C the coke had a conductivity of 14.1 Ω^{-1} and the char and gas coke had approximately the same value of 6.1 Ω^{-1}. The coke saw the volatile bump (in this case decrease in conductivity) between 1000-1300 °C, whereas the char and petcoke increased steadily. For the smaller grain size of 2.36-5 mm the trend was the same, but the conductivity decreased slightly. They also tested mixtures of ferrochrome smelting charge and found that the conductivity was much lower in the charge mixtures than for the reductants alone and that using metallurgical coke made the conductivity more sensitive to changes in the charge than with the char and gas coke.

Hasannezhad and Meysami [65] showed that increased resistance and porosity led to higher efficiency and lower energy consumption in ferrosilicon arc furnaces. They used coke and semicoke for comparison and showed a 10.3 % increase in furnace efficiency when using the semicoke compared to coke. The porosity was measured through immersion methods and confirmed with SEM imaging. The apparent porosity of the semicoke was three times the porosity of the coke and the bulk densities of the materials were comparable at 0.921 g/cm^3 for the semicoke and 1.075 g/cm^3 for the coke. Their measurements went to 600 °C and they found that semicoke was 1250 mΩm and coke was 110 mΩm. Furthermore, they believed the greater porosity in the semicoke samples allowed for better transfer of SiO gas which contributed to the greater furnace efficiency. Increased porosity will also affect the contact resistance as a large number of pores will lead to many additional small and poor points of contact.

Surup et al [9] studied the properties of blends of charcoal, coal, and coke used in SAFs and found that the resistivity of the carbon bed was determined by the temperature and volume fraction of conductive material. Their results show that at least 40 % of the material must be conducting to allow for conduct current through the entire bed. Charcoal below 650 °C was nonconductive and can therefore inhibit current paths in the upper regions of SAF. Surup et al [8] also studied the electrical resistivity of carbon materials up to 1700 °C. They found that the resistivity of charcoal is similar to fossil-based reductants above 1400 °C and that residence time and maximum temperature had little effect on resistivity compared to the heat treatment temperature. In another study, the origin of the charcoal was not found to influence the electrical resistivity [10]. Additionally, they found that the bulk density and load also had a large impact on the resistivity. Particle size, on the other hand, showed little effect at high heat treatment temperature and high compaction pressure. Furthermore, the mechanical durability of charcoal was increased after heat treatment, whereas coke and coal saw the opposite trend.

Extensive work was also done by Pedersen [7] [66] on the resistivity of carbon materials for silicon production. The resistivity of the carbon materials is shown in Figure 22. Pedersen confirmed the trends found in other works that charcoal has the highest resistivity, followed by char and coal (both heat-treated). He also saw the “bump” at 1200 °C that Krogerus and argued that this was due to devolatilization.

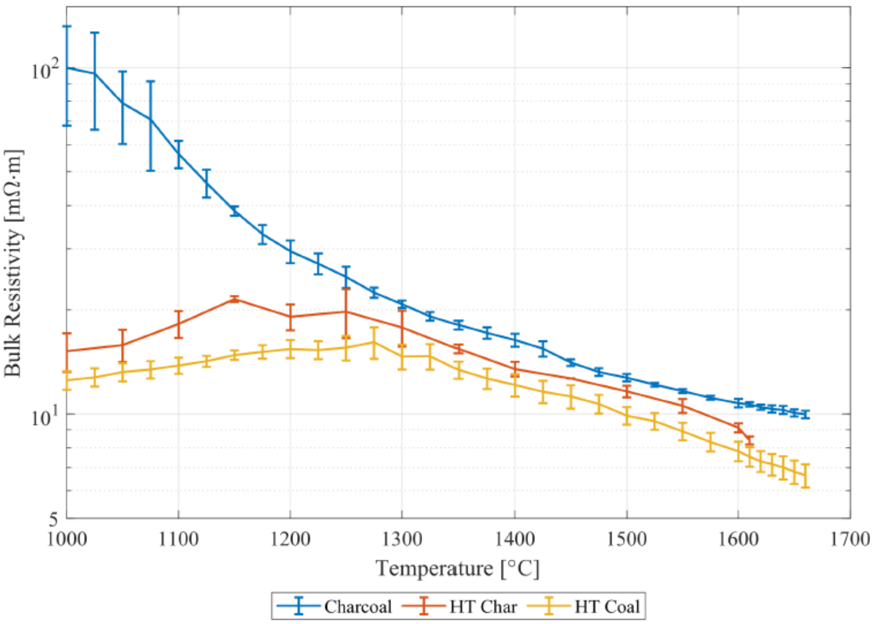

Figure 22. Bulk resistivity with increasing temperature for coal, char, and charcoal from Pedersen's MSc Thesis [69]

Pedersen then sought to measure the resistivity as the char and charcoal were exposed to SiO gas. Based on the excavation of the crucibles after the experiments, little SiC was produced beyond the bottom of the measuring zone and condensate formation around the measuring wires impacted the results. The resistivity with increasing temperature of the experiments is shown in Figure 23. There is a steep decrease in resistivity after 800 °C for experiments 3 and 4 (charcoal), and an increase as the chemical reactions begin to take place. The resistivity stabilizes over time with constant temperature. Experiment 2 used heat treated char and saw little SiC formation, which explains why the resistivity is less sensitive to temperature changes. With increasing SiC formation, oxides would form around the Mo-wires in the setup, and hence a high resistivity was measured at longer times.

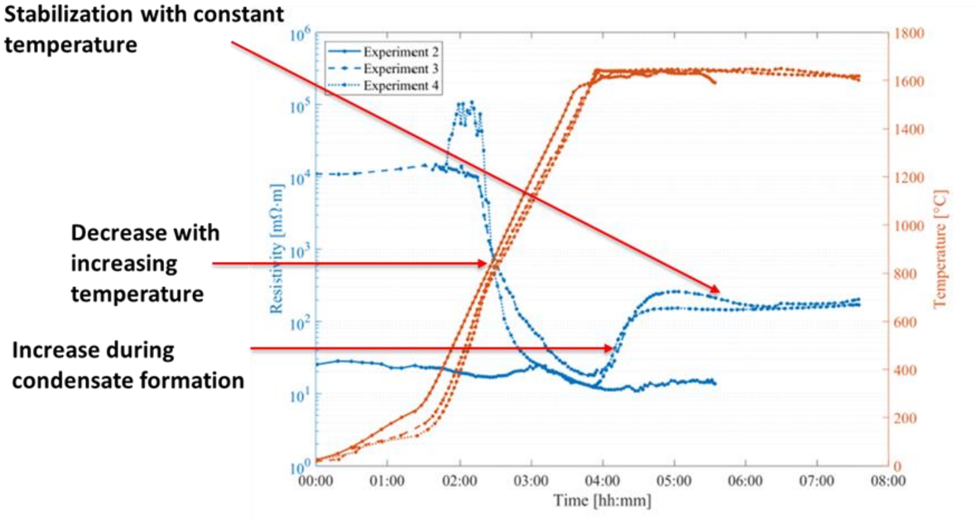

Figure 23. Bulk resistivity with increasing temperature of char and charcoal as they are converting to SiC with emphasis on the major changes in resistivity from Pedersen's MSc thesis [69] with areas of interest highlighted by Haley Hoover.

Table 5 shows a summary of the various values found in literature for the bulk resistivity of carbon materials. Some units have been converted for clarity.

Table 5. Bulk resistivity values of various relevant materials from literature

Material	Temperature	Resistivity	Particle size
various cokes [6]	1500 °C	4-14 mΩm	10-30 mm
petcoke [6]	1450 °C	8-20 mΩm	10-30 mm
charcoal [6]	1600 °C	7-16 mΩm	10-30 mm
anthracites [6]	1400 °C	9 and 41 mΩm	10-30 mm
coke [19]	1600 °C	20-36 mΩm	3-6 mm
char [19]	1600 °C	16.6 mΩm	3-6 mm
coke [64]	1600 °C	70.9 mΩ*	5-25 mm
char and gas coke [64]	1600 °C	164 mΩ*	5-25 mm
coke [65]	600 °C	110 mΩm	
semicoke [65]	600 °C	1250 mΩm	
charcoal [7]	1600 °C	10.8 mΩm	4.5-9.5 mm
char (treated) [7]	1600 °C	9.1 mΩm	4.5-9.5 mm
coal (treated) [7]	1600 °C	7.8 mΩm	4.5-9.5 mm
charcoal/SiC/condensate [7]	1600 °C	200 mΩm	4.5-9.5 mm

*published as conductivity and converted to resistance

A study on SiC ceramics performed at room temperature [67] found that increasing the carbon content decreased the resistivity and compressive strength of the sample. In contrast, the addition of silicon increased the resistivity and compressive strength. These trends were seen from increases from 0-50 wt% for the carbon and 0-30 wt% for the silicon.

2.7 SLAG IN FESI/SI FURNACES

Although in theory, production of silicon is a “slag free” process, impurities in the raw materials and imperfect operations result in the formation of slag in the furnace. Slag usually consists of SiO_2-CaO-Al_2O_3. The ratios of these three oxides, as well as temperature, determines the properties of the slag, including the viscosity and electrical conductivity. The slag has the potential to affect the quality of furnace operations by making tapping more difficult, for example if it is highly viscous [68].

The slag composition will vary vertically within the same furnace due to the temperature. Typically, slag collected lower in the furnace will contain less SiO_2, as more of it will be reduced compared to higher in the furnace where the temperature is lower, and the quartz may still be solid. Higher amounts of CaO in the slag will result in lower viscosity, therefore slag high in SiO_2 and Al_2O_3 will have a high viscosity [69].

Liu et al. [70] studied the electrical conductivity of CaO-SiO_2-Al_2O_3 slags and found that the electrical conductivity decreased and then increased with increasing CaO/Al_2O_3 ratio with constant SiO_2. The minimum occurs at CaO/Al_2O_3=1. Similarly, at fixed Al_2O_3 content, the conductivity increased by replacing SiO_2 with CaO. Additionally, they calculated the conductivity from the viscosity of the slags and compared that to their direct conductivity measurements. The experimental and calculated results showed reasonable agreement, thereby showing the direct correlation between conductivity and viscosity of the slags. The conductivity contours from the Slag Atlas [71] for Al_2O_3-CaO-SiO_2 melts at 1650 °C shows the conductivity is lower for higher SiO_2 amounts.

3 SiC FORMATION IN A BED OF PARTICLES

This chapter describes the thesis work regarding the formation of SiC. Although the work producing SiC was done to produce materials for the resistivity measurements, knowledge has been obtained during these experiments. Thus, it is treated here as a separate chapter, although the experimental design is limited compared to a separate study. The aim was to study and verify the mechanism of carbon materials transforming to SiC and the formation of elemental silicon in the SiC.

3.1 MATERIALS, APPARATUS, AND METHODS

This section details the materials and methods regarding SiC formation in a bed of particles. The materials used to produce the SiC are shown, followed by the methods to produce it and the characterization techniques. These materials provide the raw materials for the electrical resistivity measurements. The methods for electrical resistivity are then explained in Chapter 4. Sethulakshmy Jayakumari and Khadija Choudry contributed to this section of the work through performing a few of the SiC formation runs under the supervision of the author. This contribution will be indicated in the experimental tables. All characterization and interpretations were done by the author.

3.1.1 Materials

Quartz and silicon produce SiO gas via Equation 2, which then flows upwards and reacts with the carbon material to form SiC via Equation 3. Over time and at high temperature the SiO gas will again react with the SiC to produce elemental silicon according to Equation 4. The amount fixed carbon, ash, volatiles, and moisture for the carbon materials used is shown in Table 6, as well as their particle densities measured using gas pycnometry, which is explained later. The composition of the carbon materials was obtained by proximate analysis from ASG Lab in Germany. Proximate analysis is conducted by using mass loss during heating in specific atmospheric conditions to determine the moisture, volatiles, fixed carbon, and ash. The total mass “as received” is heated to 105 °C to evaporate any moisture. The remaining mass is the total solids, and the moisture is the difference between the weigh “as received” and the total solids. The total solids are then heated in an inert atmosphere at 950 °C. The remaining mass of the sample is the nonvolatile matter, and the difference is the volatiles. Finally, the nonvolatile matter is oxidized at 815 °C. The remaining mass is the ash, and the mass loss during this step is the fixed carbon [72].

$$SiO_2 + Si = 2SiO_{(g)} \tag{2}$$

$$SiO_{(g)} + 2C = SiC + CO_{(g)} \tag{3}$$

$$SiO_{(g)} + SiC = 2Si + CO_{(g)} \tag{4}$$

Due to the caking performance of the coal, it was heat treated (HT) before the experiments and then crushed into the correct size. The heat treatment for the coal was performed in an induction furnace at 1200 °C for approximately 15 minutes. Particle size of the carbon materials was 4-9.5 mm. If needed, materials were crushed using a jaw crusher and then sieved to the correct sizing. The quartz had a purity of 99.2 % according to chemical analysis. The silicon was the same as was used in Jayakumari's work, and had a purity of 99 %, according to the supplier [41].

Table 6. Chemical analysis of carbon materials used measured by proximate analysis analyzed by ASG Lab in Germany. Density was measured by gas pycnometry.

Material	fixedC(%)	Ash(%)	Volatiles(%)	Moisture (%)	Particle density (g/cm^3)
CharA	88.5	5.87	5.4	8.8	1.86
CharcoalA	85.9	3.97	15.9	27.5	1.26
CoalA	78.3	1.25	38.8	12.2	
CoalA (HT1200 °C)	96.1	2.28	0.4	0.2	1.75

3.1.2 Apparatus

The heating apparatus used in this work was an induction furnace, pictured in Figure 24. The induction furnace uses a high frequency current to induce an electromagnetic field, which then in turn interacts with the conductive graphite crucible to produce heat. The entire system includes a power supply, induction coil, refractory lining, water cooling system, and an exhaust. During operation, a temperature gradient is present due to heat loss through the open top of the furnace and due to coil placement within the furnace.

Figure 24. Picture of induction furnace used throughout this work taken by the author.

To examine the temperature gradient, an experiment was conducted by Sethulakshmy Jayakumari using 5 thermocouples. The gradient was measured from the top of the sieve, or the top of the SiO_2/Si bed if a sieve was not used, (~5 cm from the bottom of the crucible) to the top of the carbon layer in increments of 2 cm. The measured temperatures at each point are shown throughout the length in Figure 25. The middle thermocouple (TC3 on the figure) is not shown because of a malfunction during experimentation. In Figure 26, a graph of temperature versus height in the crucible is shown to display the change more clearly. Based on the trend, the middle of the carbon bed will be around 200-250 °C colder than the bottom. Temperature was controlled using a C-type thermocouple encased in alumina to prevent damage. The thermocouple was connected to the controller which controls the heating rate, holding temperature, and holding time.

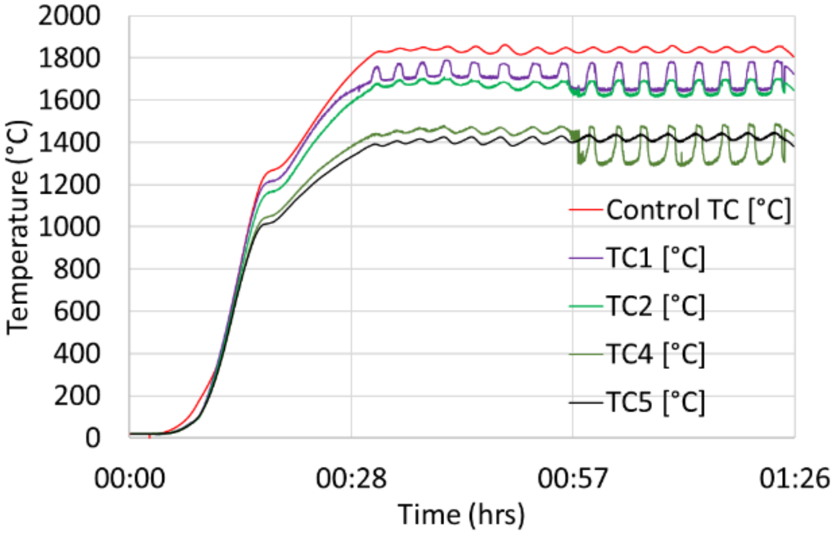

Figure 25. Graph of time vs. temperature during a SiC formation experiment where 5 thermocouples were placed at 2cm intervals in the carbon bed to determine the temperature gradient. TC3 is not shown due to failure during the experiment.

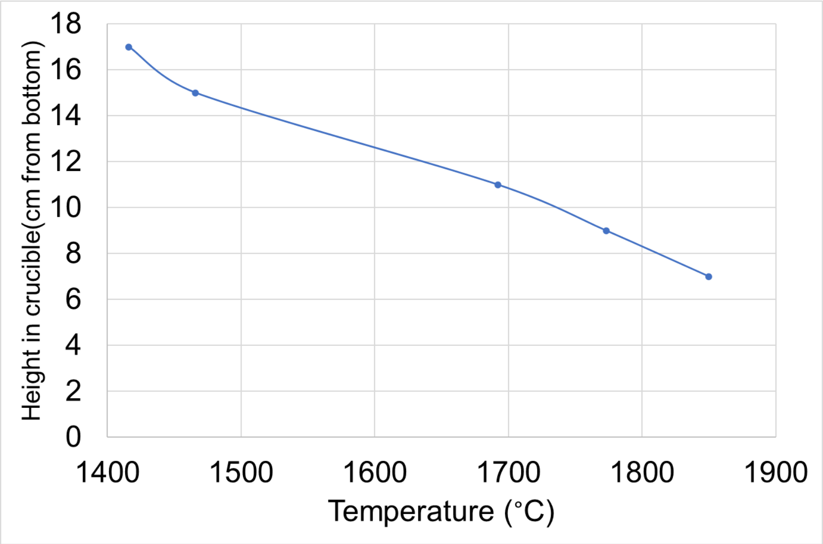

Figure 26. Graph of temperature versus height in the crucible during a SiC formation experiment, where 1850 °C was the target temperature for the bottom of the carbon bed.

The crucible setup is shown in Figure 27. Materials are loaded into a graphite crucible, with a thermocouple placed at the bottom of the carbon bed, in the radial center of the crucible. This corresponds to the red line ("Control TC") in Figure 25.

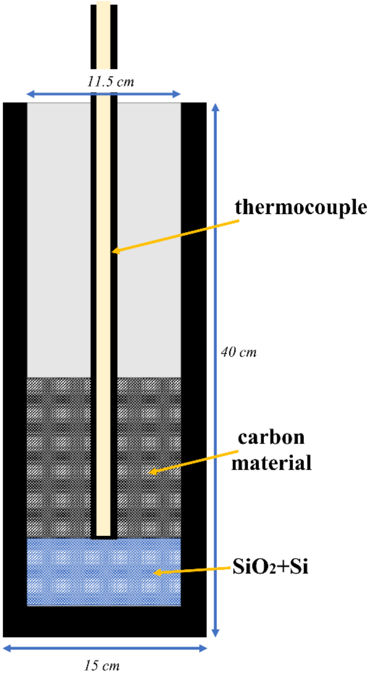

Figure 27. Drawing of a sample graphite crucible used to produce SiC: the height, outer diameter, and inner diameter are 40 cm, 15 cm, and 11.5 cm, respectively, and the height of the carbon material layer is around 10-12 cm.

The temperature curve for the formation of SiC from char at 1850 °C with a holding time of 60 minutes is shown in Figure 28. There is some variation between the programmed and the measured temperature, due to the various chemical reactions taking place as well as the existing temperature gradient. However, the holding time is started as soon as the measured temperature reaches the target holding temperature.

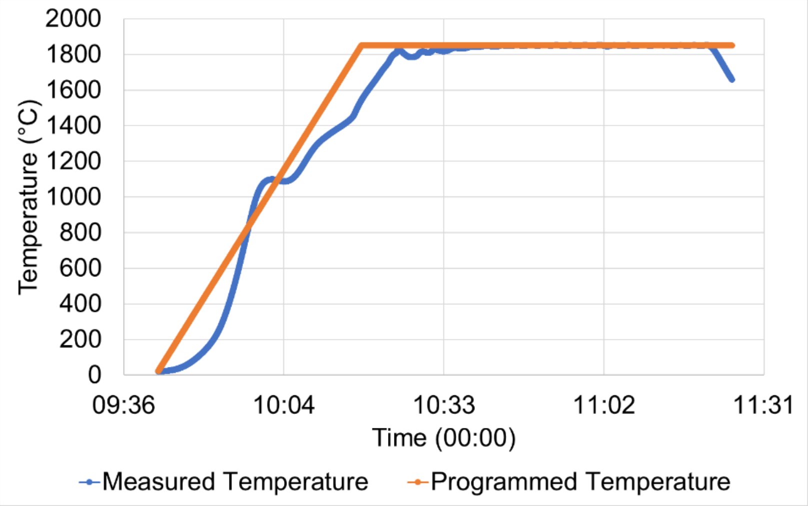

Figure 28. Graph of temperature with respect to time comparing the measured temperature with the programmed temperature for automatic control during an experiment with char with a holding temperature of 1850 °C and a holding time of 60 minutes.

3.1.3 Methods

The SiC material used in this work is produced with a procedure based on the work of Jayakumari [31] with the goal of producing approximately 1 liter of material. A 1:1:4 molar ratio, that is a stoichiometric amount according to Equation 3, of quartz, silicon, and carbon material is layered in a graphite crucible as seen in Figure 27. The amount of carbon material used was slightly reduced to reduce the amount of unreacted carbon leftover after the experiment. The materials were weighed and placed in the graphite crucible before being placed in the induction furnace. The temperature and holding times were varied between 1750-1850 °C and 60-90 minutes, as shown in Table 7. This ensures SiC materials with varying amounts of SiC and Si formed via Equations 2-4 [31]. In some cases, a graphite sieve with 2-mm holes was placed on top of the SiO_2/Si mixture to allow for better SiO gas permeation and separation to the carbon material. The carbon material as well as a graphite tube housing the thermocouple was placed on top of the sieve.

After the experiment, the partly transformed SiC material was extracted from the crucible in three layers, the top layer containing mainly unreacted carbon, the middle layer containing SiC and carbon, and the lower layer containing more SiC and Si. This was determined by the visible color and structure, so there is some variance. The top layer was often disregarded as it was mostly unreacted carbon due to the low temperature and SiO pressure. The middle and lower layers were separated based on color. However, often sample sizes were too small to be used for resistivity measurement, so they were combined. Samples of the same carbon material but different experimental conditions were again combined to obtain large enough sample sizes. Later in this work, more repetitions of the same experimental conditions were done to prevent the need to combine materials, which is why some samples are labelled as "mixed" and others specify that they come from sample produced under the same conditions and taken from the same layer. Samples sent for chemical analysis were obtained using a riffle splitter as a measure to obtain representative samples. Images from an experiment with charcoal are shown in Figure 29 to show how the layers are sorted. Table 7 lists all the SiC formation experiments, with their maximum temperature and holding time.

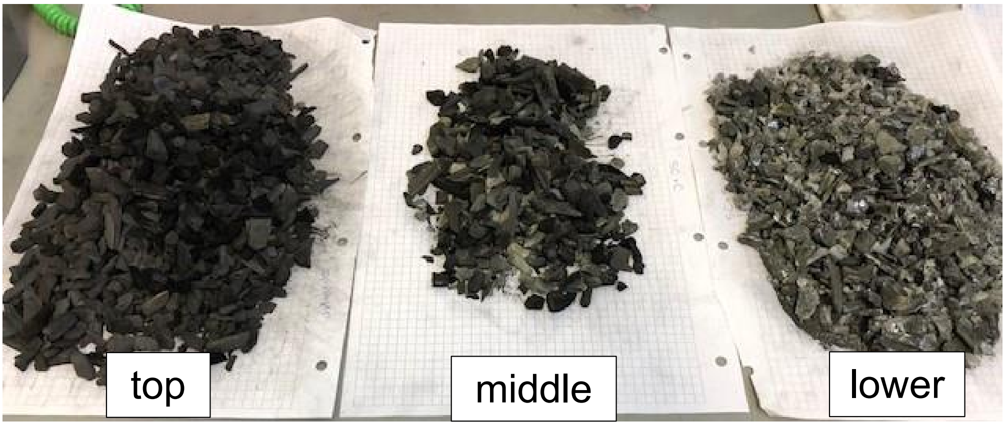

Figure 29. Top(left) middle (middle) and lower (right) layers from SiC from charcoal before they are sieved. Many fines are present, especially in the lower layer sample along with some quartz impurities that are taken out.

Table 7. List of SiC formation experiments including their carbon material, holding temperature and holding time. Samples are labelled with “A,B,C” designations based on when additional materials from different sources are used in the resistivity measurements. “B” and “C” were not transformed to SiC and are hence not included here.

Number of experiments	Carbon material	Temperature (°C)	Holding time (min)
4	HT CoalA	1825	60
1	CharcoalA	1750	90
2	CharA	1750	60
1	CharA	1750	90
3	CharA	1850	60
1	CharcoalA	1850	150
3	CharcoalA	1850	60
2	CharcoalA	1850	90
3	CharcoalA	1750	60
3*	HT CoalA	1850	60
3*	CharA	1850	60
3*	CharcoalA	1850	60
2**	CharcoalA	1850	60
2**	CharcoalA	1850	120
2**	CharcoalA	1850	180

*indicates experiments run by Sethu Jayakumari
** indicates experiments run by Khadija Choudry

3.1.4 Characterization

Chemical analysis was performed on all partially transformed materials by Degerfors Lab (D-lab) and gave the amount of free carbon, total carbon, and total silicon in the samples. The total Si was measured using X-ray fluorescence (XRF). The total carbon was measured using LECO CS-444 and the free carbon using a LECO RC-612. Based on the values of free carbon, total carbon, and total Si, the amount of SiC, C, and Si were calculated based on equations 11-13, which were also used by [41].

$$\%SiC = (\%C_{total} - \%C_{free}) \times \frac{MM_{SiC}}{MM_C} \tag{11}$$

$$Si\ in\ SiC = \%SiC \times \frac{MM_{Si}}{MM_{SiC}} \tag{12}$$

$$\%Si = \%Si_{total} - Si\ in\ SiC \tag{13}$$

To further characterize the SiC material SEM (Scanning Electron Microscope) and EPMA (Electron Probe Micro-Analyzer) were used to identify phases [73] [74]. CT was also used. SEM uses high energy electrons in the focused beam to produce signals which are read on a 2D image. It is used to examine the morphology and structure of samples, as well as chemical composition when paired with energy dispersive x-ray microscopy (EDS). An EDS detector separates the x-rays of abundant elements in the sample into an energy spectrum to show the composition of a given area of spot [73]. An electron probe micro-analyzer (EPMA) was used to identify different phases and specific compositions for mixed samples. The particles were cast in iodoform epoxy to give better contrast. This will make it possible to distinguish the carbon phases and the epoxy. EPMA works similarly to the SEM but is more precise in its quantitative analysis through the use of wavelength dispersive spectroscopy (WDS) [74]. SEM imaging was done using Zeiss Supra. EPMA was performed using XA-8500F Field Emission Electron Probe.

In evaluating the density of the materials, three different methods were used. First, gas displacement pycnometry was used to calculate the “true” particle density of some materials, or the density of one particle excluding open pores and voids. In this method, an inert helium gas is pumped into a chamber containing the sample in a receptacle of known volume. The helium fills the space not occupied by the sample, including any open pores of at least 1 Å in diameter. The pressure difference observed from discharging the gas from the sample chamber into another empty chamber then allows for calculation of the volume of the solid sample. From the volume and the mass, the density is then calculated. These measurements were performed using the Accupyc II 1340 (Figure 30) and are illustrated in Figure 30 taken from the manufacturer of the instrument, Micromeritica [75]. The second method involves a similar procedure as pycnometry, but with sand as the medium instead of helium gas. This allows the envelope density to be measured, in other words the density of a single particle including its pores. The porosity of the material was calculated from the difference in volume from the two methods. Finally, the bulk density was measured by obtaining the mass when the sample filled a container of known volume.

Figure 30. Pycnometer used (left) and schematic of how the instrument works from the manufacturer [75] (right)

Computed tomography (CT) [76] was used to take images of the partially transformed SiC material to examine the SiC formation in a bed of particles. As this method is relatively new in this area, the work is done to check if this method can be used to separate the heterogeneous carbon materials from the produced SiC. CT is a non-invasive method for imaging where the instrument rotates an object between an X-ray generator and a detector. The X-rays essentially show differences in the density of the material, because denser materials will absorb more of the X-rays and less dense samples will absorb fewer X-rays which will then pass through to the detector. A series of 2D images are then reconstructed using software to give a 3D model (see Figure 31 below).

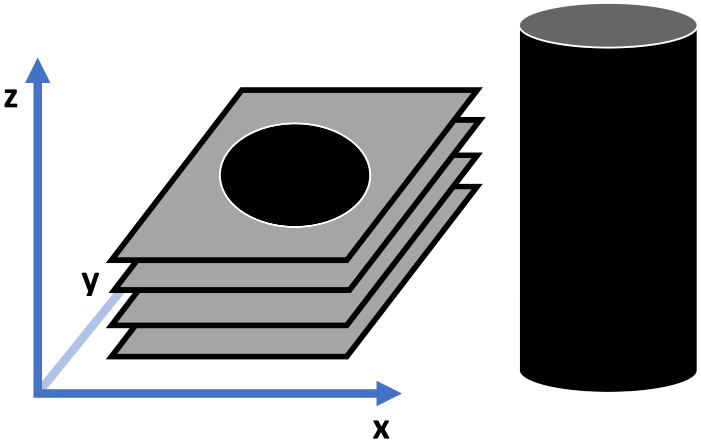

Figure 31. An example of CT stacks of 2D images and how they are oriented to produce a 3D model after processing.

Compression Testing was used to compare the mechanical strength of the SiC and carbon materials from coal and char. Charcoal was not measured as the material was too flat and brittle to give results. A Zwcik Roell testing machine with a maximum of 2.5 kilo-Newtons (kN) was used to measure the force needed to crumble a single particle. Breaks were not always clean and multiple breaks can occur when the material is irregularly shaped, so the particles crumbled instead of splitting. Therefore, multiple particles of each material were tested to discover a possible trend. The instrument setup is shown in Figure 32. Data obtained was filtered below 100 N to account for surface cracks, bumps, and other irregularities on the surface.

Figure 32. Image of Zwcik Roell compression testing machine with a yellow arrow pointing to where the sample is placed.

At the end of this work, a CT scan of an entire crucible was taken for an experiment with charcoal, which was run at a holding temperature of 1750 °C for 1 hour. The before and after of the same slice of the scan is shown in Figure 33. The charcoal bed forms a U-shape after the experiment. As the quartz and silicon form SiO, the volume of the SiO_2-Si bed will be reduced, causing carbon material is flow down. However, since there is more SiO_2 and Si at the edges, less will flow down there. There is also some volume loss due to using an open furnace, as the top of the carbon bed will be exposed to oxygen. The charcoal is effectively being heat treated, increasing the fixedC when losing volatiles. There is also movement of the graphite tube which houses the thermocouple. During the excavations of the crucible, one did not notice the radial change of SiC transformation, only the vertical. This could be because of radial temperature gradient in the crucible, the center of the bed at this height in the crucible may not have sufficient temperature to support the formation of SiC compared to the edges which are closer to the heating element and the SiO generators.

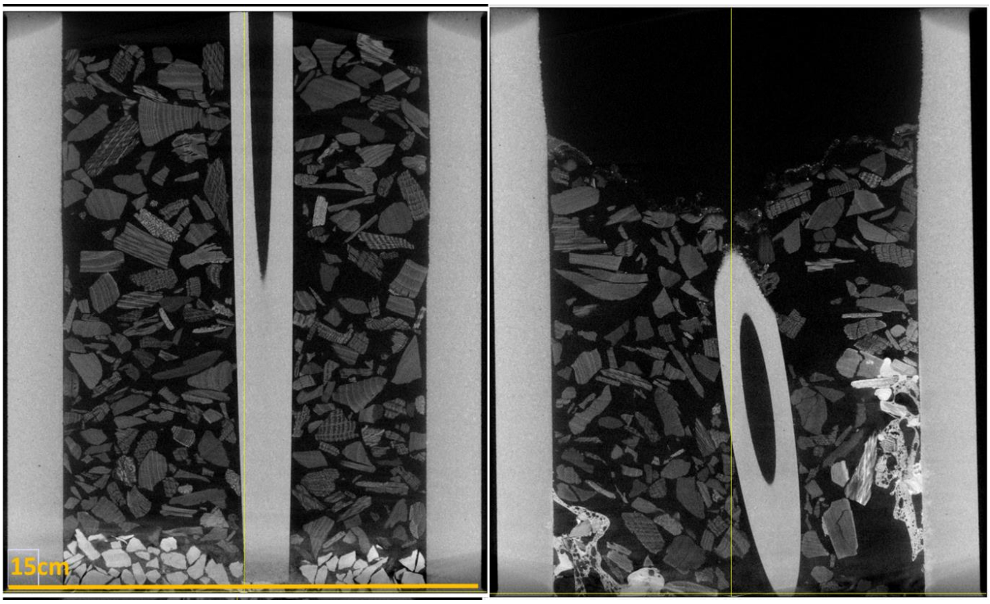

Figure 33. CT scan before (left) and after (right) of the charcoal bed for 1750 °C and 1 hour holding time.

3.2 RESULTS

The amount of SiC in the partially transformed material ranges from 0 %, that is the original carbon material to 72 % SiC (from coal) taken from the lower layer of the crucible. Elemental silicon is found in some samples with the content ranging from 2%-36 %. SEM imaging and EPMA elemental mapping are done to provide another qualitative indication of the material transformation. CT scans of around 10 particles from select samples are also shown. A table of the overall SiC materials produced is shown in Table 8 for the resistivity measurements, along with if they are taken from the same layer at the same temperature and holding time, or if they are mixed. This section will focus more on individual particles, therefore the overall SiC content may not be representative, but is instead used to classify the entire sample for the resistivity measurements in Chapter 4.

Table 8. Summary of SiC materials produced as individual layers or mixed samples

SiC content, Si content (%)	Carbon source	Layer in crucible
30 %SiC	HT coal	Mixed
69 %SiC	HT coal	Middle
72 %, 7 %Si	HT coal	Lower
32 %SiC	CharA	Mixed
35 %SiC	CharA	Middle
63 %SiC, 2 %Si	CharA	Lower
54 %SiC, 6 %Si	CharcoalA	Mixed
60 %SiC, 6 %Si	CharcoalA	Middle
60 %SiC, 36 %Si	CharcoalA	Mixed
56 %SiC, 1 5%Si	CharcoalA	Middle

3.2.1 SiC from coal

As the depth in the crucible increases, so does the temperature and SiO pressure. This is reflected in the transformation in the lower layer compared to the middle layer. The middle and lower layers show formation of SiC on the surface and the lower layer shows additional silicon formation. Figures 34-38 shows the SEM, BSE images, and EPMA elemental mapping of the SiC materials from coal. Formation of surface crystals and whiskers in the samples from coal were both seen. Figure 35 shows the transformation of carbon to SiC, followed by the subsequent formation of silicon for the material from coal. It appears that the SiC forms on the outer edges of the coal particle, then as a particle becomes more transformed it has SiC distributed on the surface of the particle. The SiC layer becomes thicker, even though there may be some areas of unreacted carbon, likely due to physical or kinetic hindering. As silicon begins to form in the SiC layer, gradually less carbon is seen, and the silicon appears to form in the pores and become more homogeneously distributed across the particle. EPMA elemental mapping (Figures 36-38) once again confirms this. In the 30 %SiC sample, the carbon core of the particle is visible and the SiC phase is visible on the surface. A very small amount of Si appears to be present, which was not measured in the chemical analysis, but this is likely due to some small variations in the individual particles and the overall sample contains little to no Si.

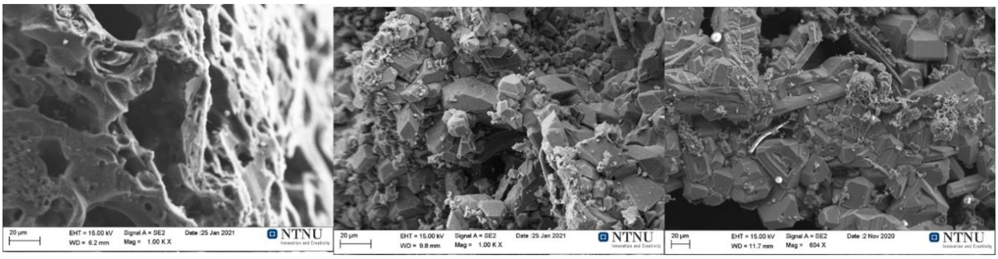

Figure 34. SEM images of material from coal as it is not transformed to SiC (left), to where surface crystals have formed (middle) and as the particle is more highly transformed larger SiC crystals are formed (right).

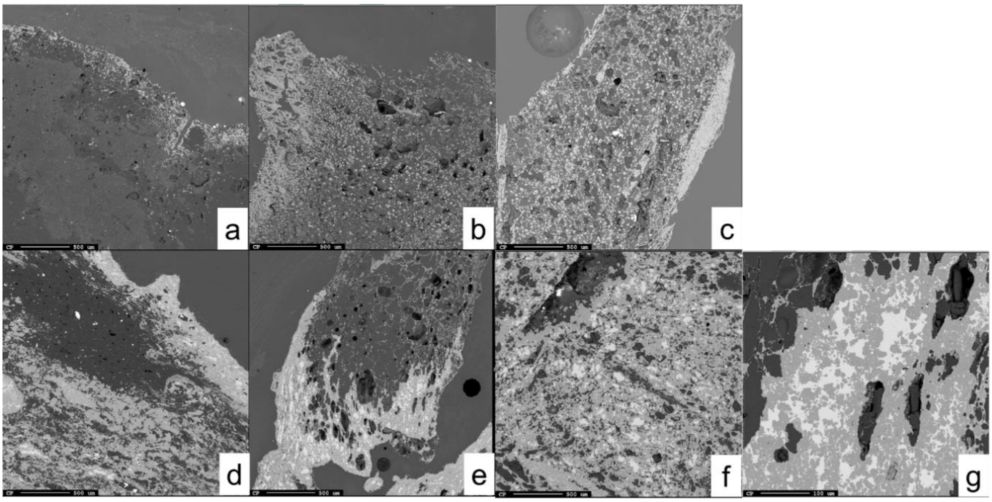

Figure 35. BSE images of materials from coal as they are transformed to SiC. In (a) and (b) the particle is mostly carbon with some SiC forming on the outer edge of the particle. In (c) and (d) the outer edges of the particle still contain a thicker layer of SiC, but there is SiC evenly distributed across the inner surface. In (e) elemental silicon has begun to form in the thick SiC layer on the outer edge of the particle, whereas the inner particle is still carbon. In (f) and (g) the particle is highly converted to SiC and Si seems to have filled the pores of the original carbon.

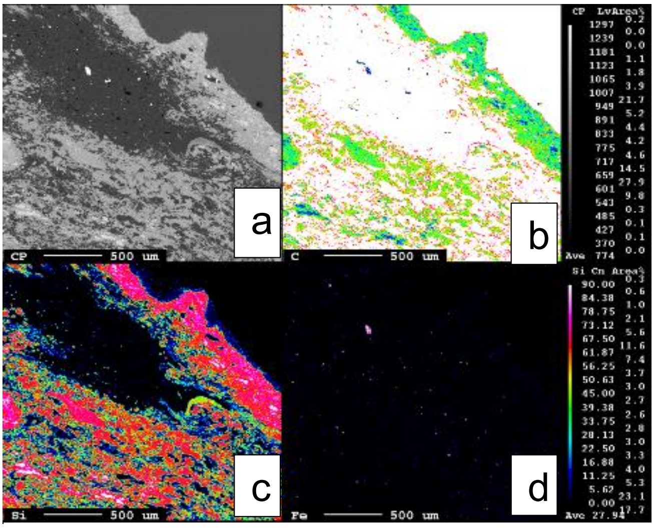

Figure 36. EMPA elemental mapping of 30 %SiC from coal. The BSE image (a) is the same as Figure 35(d). In (b) it can be seen based on the color gradient that carbon is concentrated in the core of the particle, and present on the surface and outer edges. In (c) the pink areas show silicon presence that align with the carbon presence in (b) with no silicon in the core that corresponds to carbon. In (d) it shows that there is very little iron present.

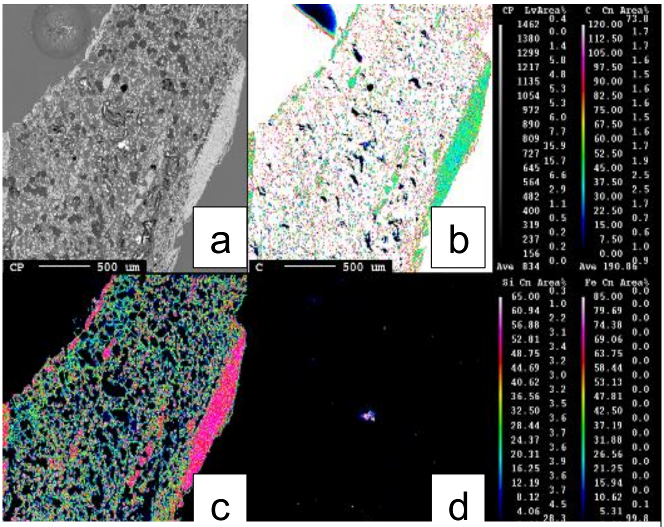

Figure 37. EPMA elemental mapping of 69 %SiC from coal. The BSE image (a) is the same as Figure 35(c). In (b) it can be seen based on the color gradient that carbon is concentrated in the core of the particle, and present on the surface and outer edges. In (c) the pink areas show silicon presence that align with the carbon presence in (b) with little silicon in the core that corresponds to SiC and carbon. Si scale is set by operator, since little to no "pure Si" is seen, maximum scale is set at 65%. In (d) it shows that there is very little iron present.

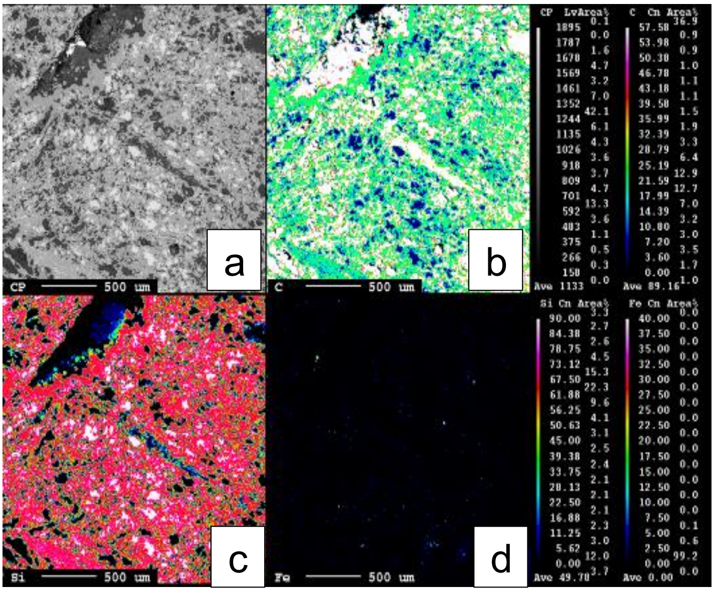

Figure 38. EPMA elemental mapping of 72 %SiC 7 %Si from coal. The BSE image (a) is the same as Figure 35(f). In (b) it can be seen based on the color gradient that carbon is throughout the particle corresponding to the SiC and is not present in the areas of silicon. In (c) the pink areas show silicon presence that align with the carbon presence in (b) with areas of elemental silicon shown in the pores. In (d) it shows that there is very little iron present.

CT scans of around 10 particles cast in epoxy are shown in Figure 39, along with a photograph of the sample and a BSE image of an area of one of the particles. In Figure 39, the particle that is examined (outlined in red in a and b) appears porous and has two shades of gray present. The idea is that the two shades correspond to SiC and carbon. Upon closer examination of the particle (c in the figure) an area was observed in the EPMA, where the edges corresponding to the BSE image (d) is drawn in red. The BSE image reveals the area is mostly carbon with a small amount of SiC lining the outer edge. Compared to the CT, it seems the carbon likely represents the darker shade of gray seen on the CT. However, the SiC does not appear visible compared to the epoxy.

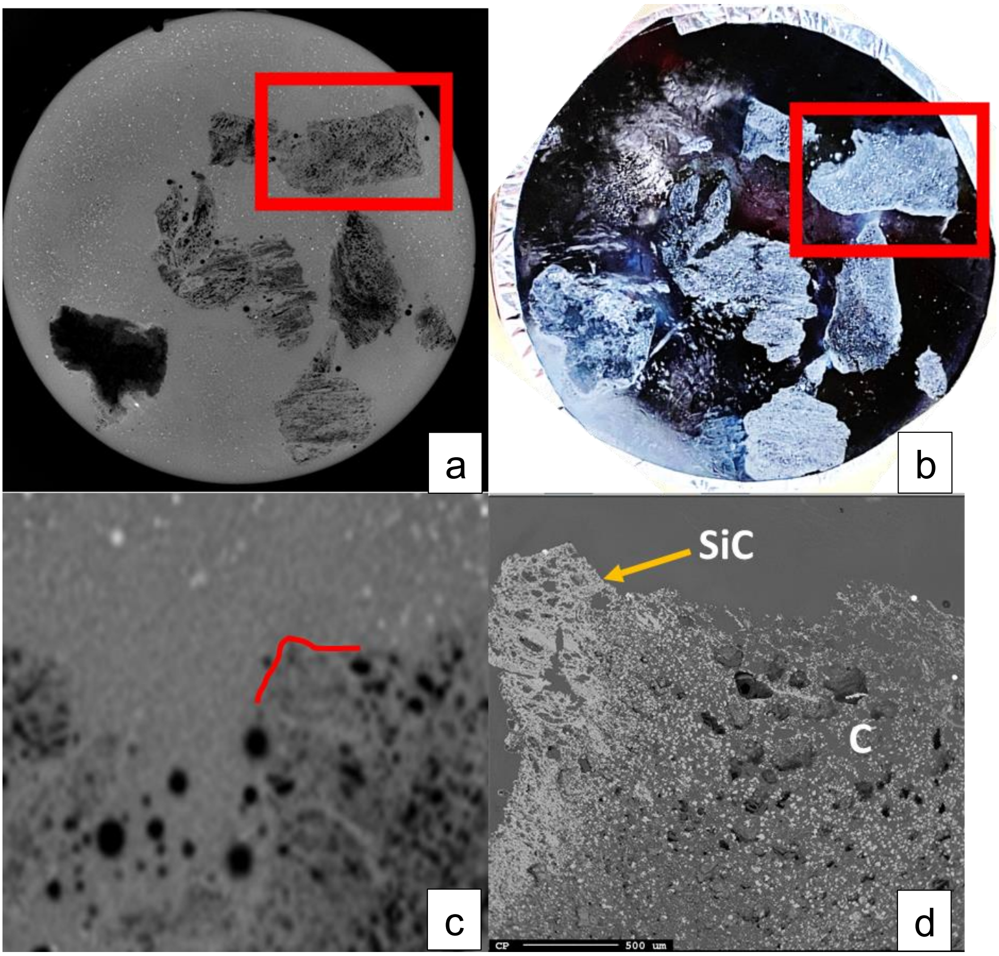

Figure 39. In (a) the overall CT slice is shown for particles from the 30%SIC from coal sample with the particle of interest outlined in red. In (b) the image is shown with the particle of interest outlined in red. In (c) the particle of interest is zoomed in and drawn in red are the borders that will define the BSE image shown in (d).

The particle density, envelope density, and porosity of the SiC materials from coal are plotted against their SiC content in Figures 40-41. The 72 %SiC, 7 %Si sample is treated separately (represented by green squares) due to the presence of silicon. A linear trendline for the materials containing SiC and carbon are shown by the blue dotted line, with the theoretical trendline based on the chemical reactions is shown by the orange line for the densities.

Based on Equation 3, if one carbon particle was converted to 100 %SiC, there would be a 67 % increase in the particle density if the volume remained constant. This is based on the equation $SiO+2C=SiC+CO$ and the molar mass of C and SiC. (40-24/24=0.67). In Figure 40, the trendline for the SiC material's particle and envelope density is approximately the same as the theoretical trendline. This implies there is no shrinkage or expansion of the periphery of the particles, so the assumption that the total volume of the particle is the same is valid. The porosity is also shown as carbon is converted to SiC in Figure 41. The porosity is approximately the same with only a 3 % increase, which could be within the experimental uncertainty. Therefore, the total volume and the pore volume are constant during the transformation to SiC. Additionally, as Equation 4 occurs, SiC will produce elemental silicon in the pores, causing a decrease in porosity and increase in the envelope density for the 72 %SiC 7 %Si samples. The results of the 72 %SiC 7 %Si sample in the particle density are likely within the experimental variability.

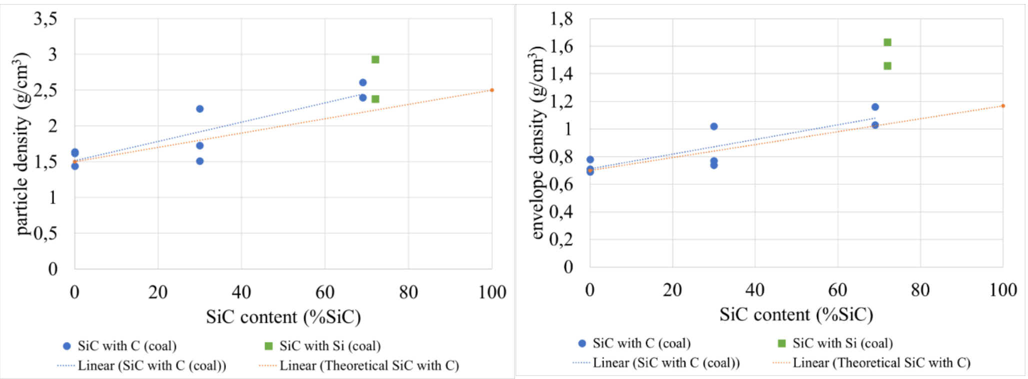

Figure 40. Particle density (left) of all SiC materials from coal in relation to the theoretical 67 % increase in density that is expected, shown by an orange line. In a linear comparison, the results are the same as the theoretical value. The envelope density (right) and SiC content of all materials is shown in relation to the theoretical 67 % increase in density that is expected, shown by the orange line. In a linear comparison, the results are approximately the same as the theoretical line.

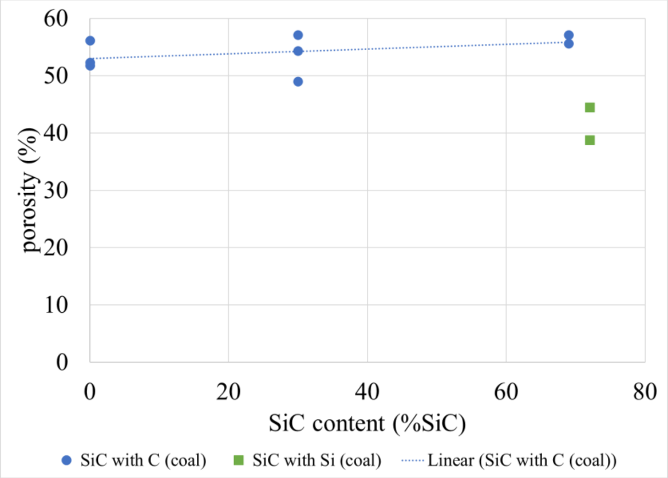

Figure 41. The porosity and SiC content of all materials (right) is shown. The porosity is approximately the same for all SiC materials until elemental Si begins to form in the pores, which decreases the porosity.

The compression test results for all SiC materials from coal are shown in Figure 42, split into three graphs for clarity. The results are shown with a 5-period moving average. For the HT coal and 30 %SiC there is no discernable difference in strength as all the curves seem to be intertwined with one another, therefore they are taken as the same strength for the remaining comparisons. The HT coal and 30 %SiC compared to the 69 %SiC has higher strength, as less force is required to crush the particles. The blue shaded region represents the HT coal and 30 %SiC and the green region represents the 69 %SiC. The 72 %SiC compared to the 69 %SiC shows that 72 %SiC is stronger, as more force is required to crush the particles, comparing the first 1.5 mm. The yellow shaded region shows the 72 %SiC and the green represents the 72 %SiC. This is likely due to the presence of elemental silicon filling the pores via Equation 4. There is a large variation from particle to particle regarding the strength, likely due to irregular size and shape. As the coal is transformed to SiC, the porosity will be about the same as the original particles and the mechanical strength of the SiC particles are lower or equal to the original coal particles. Though SiC is known to be a strong material, it is here seen that perhaps the high porosity is giving a low strength.

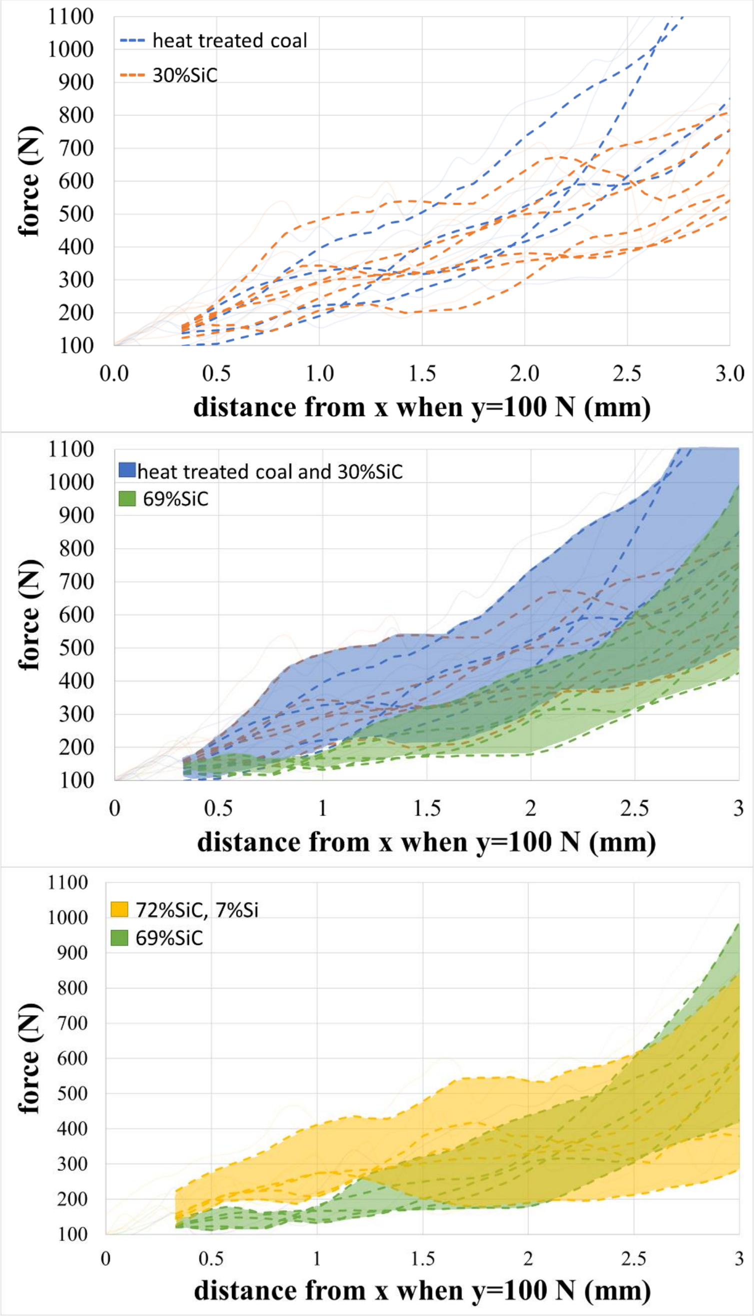

Figure 42. Compression tests for the HT coal and 30 %SiC shown with a 5-period moving average. There is no discernible difference in strength (top). Compared to the HT coal and 30 %SiC, the 69 %SiC has lower strength (middle). The 72 %SiC compared to the 69 %SiC shows that 72 %SiC is stronger, likely due to the presence of elemental silicon (bottom).

3.2.2 SiC from char

Figures 43-46 show the SEM and BSE images of the SiC from char. SiC was found as both surface crystals and whiskers in the materials from the char The middle layer contained 35 %SiC and the lower layer contained 63 %SiC 2 %Si. EPMA elemental mapping is also shown. In the 35 %SiC, both carbon and SiC and visible throughout and the sample still appears porous. In the 63 %SiC 2 %Si, the sample contains large pockets of silicon. One can also see that the char contains more iron that has been reduced to metallic iron, compared to the coal. Figure 45 shows the transformation of carbon to SiC, followed by the subsequent formation of silicon for the material from char. The SiC does not clearly form on the outer edges of the particle, as seen in the coal, but is rather more homogeneously distributed on the surface. The pores are still visible, even when the particle is highly transformed to SiC. As with the coal, elemental silicon begins to form in the pores in areas where the SiC layer is thick, but areas of carbon can still coexist on the same particle. As more silicon is formed, the pores disappear.

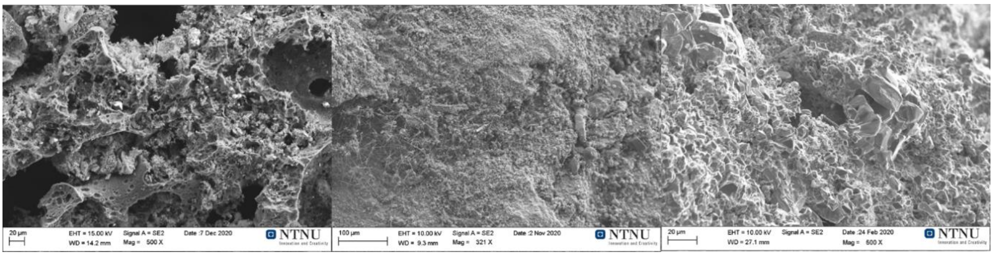

Figure 43. SEM images of material from char as it is not transformed to SiC (left), to where surface crystals and whiskers have formed (middle) and as the particle is more highly transformed larger SiC crystals are formed (right).

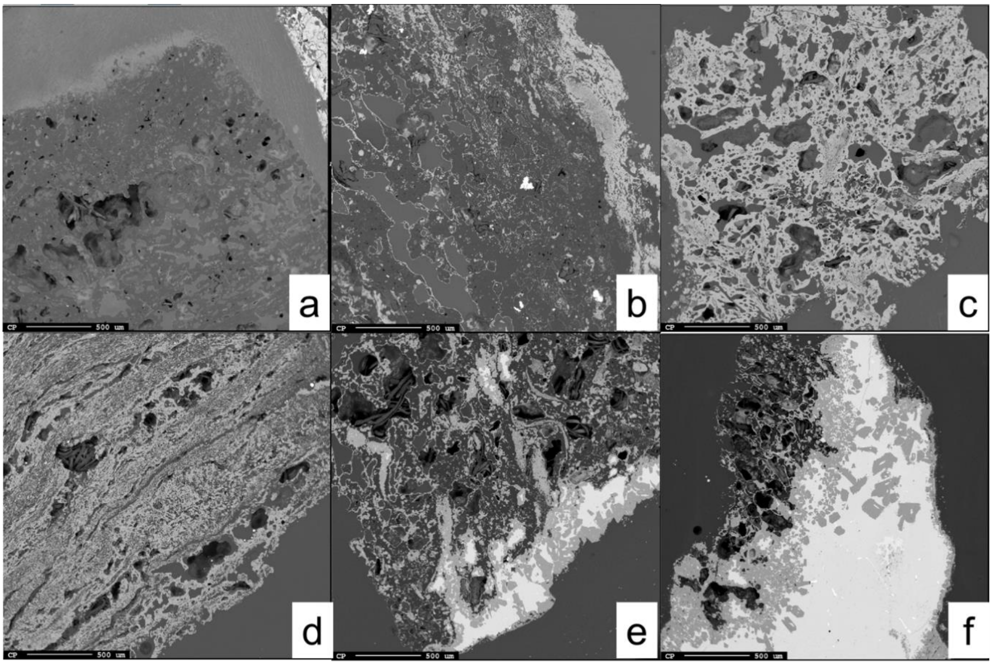

Figure 45. BSE images of materials from char as they are transformed to SiC. In (a) the particle is mostly carbon. In (b) the particle is beginning to form SiC across the surface but is still mostly carbon. In (c) and (d) the particle are highly converted and there is SiC evenly distributed across the inner surface. In (e) elemental silicon has begun to form in the thick SiC layer on the outer edge of the particle, whereas the inner particle is still carbon. In (f) the particle is mostly silicon mixed with SiC.

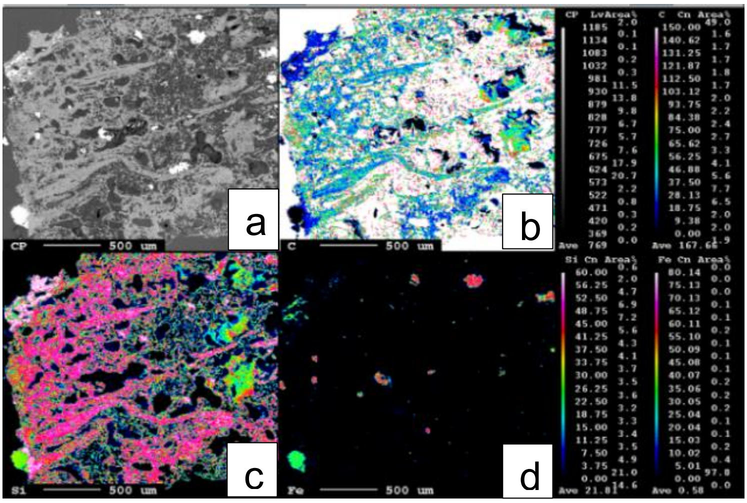

Figure 44. EPMA elemental mapping of 35%SiC from char. The BSE image (a) shows areas of SiC, carbon, Si and iron. In (b) it can be seen based on the color gradient that carbon is throughout the particle corresponding to the SiC and is less concentrated towards the edges of the particle. In (c) the pink areas show silicon presence that align with the carbon presence in (b) with a very small area of elemental silicon in the top left corner. In (d) it shows that there is some iron present.

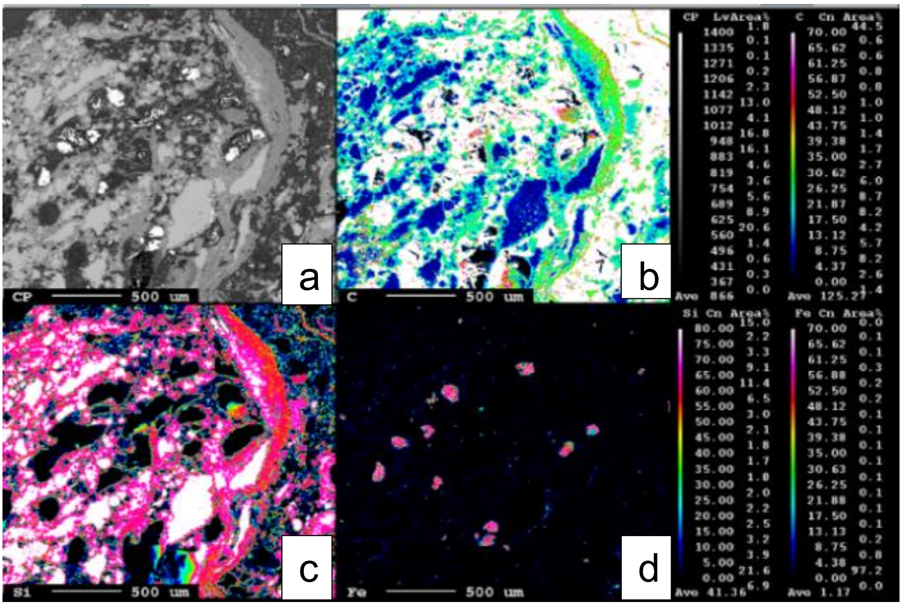

Figure 46. EPMA elemental mapping of 63 %SiC 2 %Si from char. The BSE image (a) shows areas of SiC, carbon, Si and iron. In (b) it can be seen based on the color gradient that carbon is throughout the particle corresponding to the SiC and is not present in the large pockets of silicon. In (c) the pink areas show silicon presence that align with the carbon presence in (b) with areas in pockets of elemental throughout the inner surface of the particle. In (d) it shows that there is some iron present.

CT images, photographs of the samples, and BSE of all the SiC materials from char are shown in Figures 47-48. In Figure 47 (a) and (b) the CT shows three shades of gray. Based on the BSE image, the areas of carbon and SiC can correspond to the darker and medium shades of gray respectively. However, the CT also shows a third, even lighter shade of gray. This cannot be seen in the BSE so it cannot be defined as a separate phase. In Figure 48 (a) and (c) the particle of interest has a darker color and two shades of gray. The BSE area shown in (d) only shows the gray phases, so carbon cannot be defined as the darker phase. Furthermore, the gray areas are likely SiC and silicon based on the BSE image, but these cannot be directly seen in the CT.

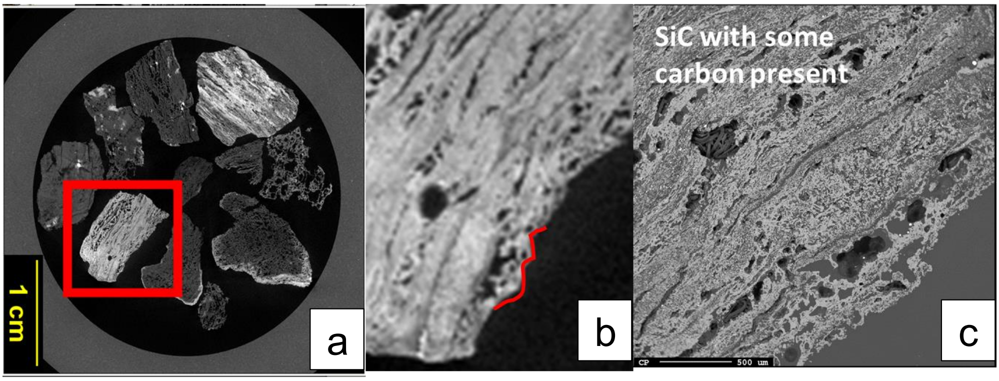

Figure 47. In (a) the overall CT slice is shown for particles from the 35 %SiC from char sample with the particle of interest outlined in red. In (b) the particle of interest is zoomed in and drawn in red are the borders that will define the BSE image shown in (c).

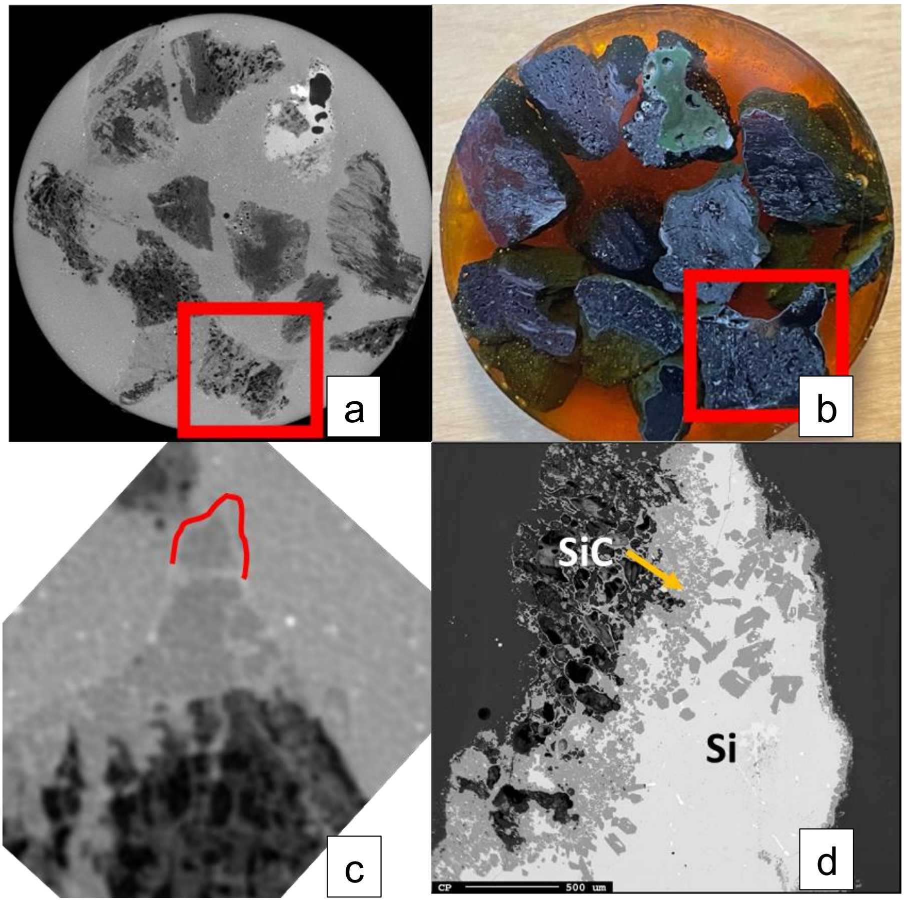

Figure 48. In (a) the overall CT slice is shown for particles from the 63 %SiC 2 %Si from char sample with the particle of interest outlined in red. In (b) the image is shown with the particle of interest outlined in red. In (c) the particle of interest is zoomed in and drawn in red are the borders that will define the BSE image shown in (d).

Compression tests were done for the heat-treated char, 35 %SiC and 63 %SiC 2 %Si. A 5-period moving average was graphed to examine the force needed to crush the entire particle. In Figure 49, the results are shown and no discernable difference in strength is seen between the 32 % and 63 %SiC. However, the char appears to be weaker than the SiC particles, as less force on average was required to crush the particle. This contrasts with findings from previous tests on coal and SiC, which found that conversion to SiC decreased the strength until silicon formed.

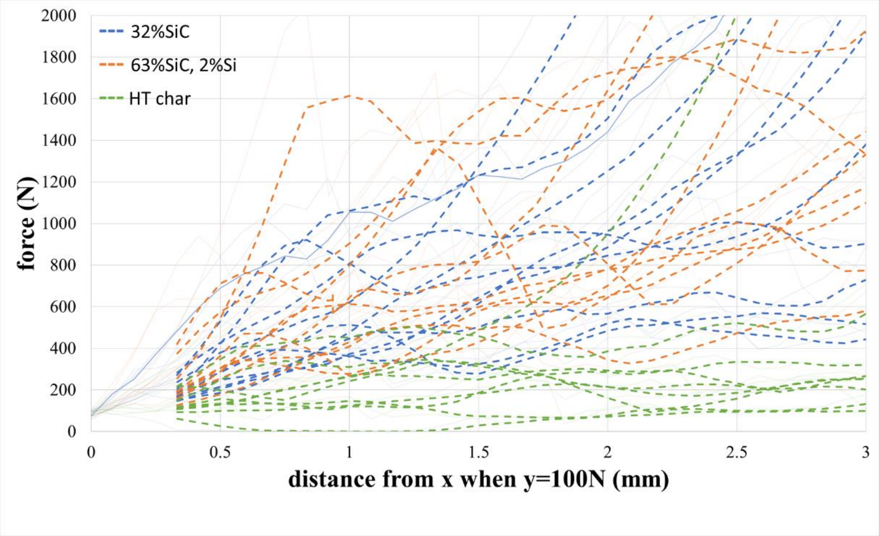

Figure 49. Compression tests for the char, 35 %SiC, and 63%SiC from char shown with a 5-period moving average. There is no discernable difference in strength between the materials with SiC, but the char is weaker than the other two materials.

3.2.3 SiC from charcoal

Figures 50-53 show the SEM and BSE images of middle and lower layers of SiC from charcoal and the EPMA elemental mapping. In the middle layer, both carbon and SiC are visible and large pores are present. The original structure of the charcoal can still be seen. Hexagonal surface crystals were seen in the SEM in addition to a small amount of whiskers. Figure 51 shows the transformation of carbon to SiC, followed by the subsequent formation of silicon for the material from charcoal. The charcoal structure is clearly visible and SiC begins to form on the outer edges of the particle and on the edges of large pores. When the particle is mostly converted to SiC, silicon begins to form in the pores of the SiC. Eventually, the charcoal structure is no longer visible as the "particles" are more or less silicon mixed with SiC.

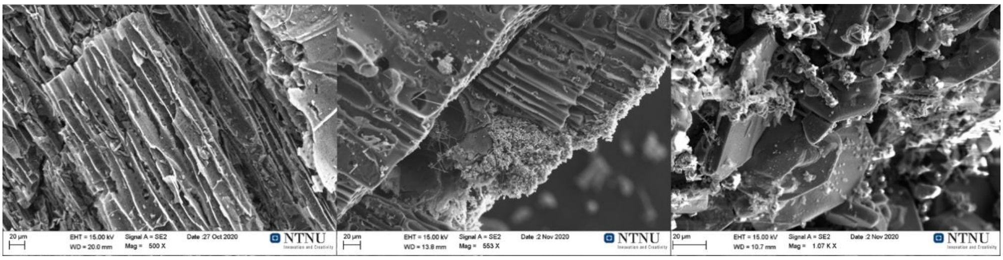

Figure 50. SEM images of material from charcoal as it is not transformed to SiC (left), to where surface crystals and whiskers have formed on the outer edge (middle) and as the particle is more highly transformed larger SiC crystals are formed (right).

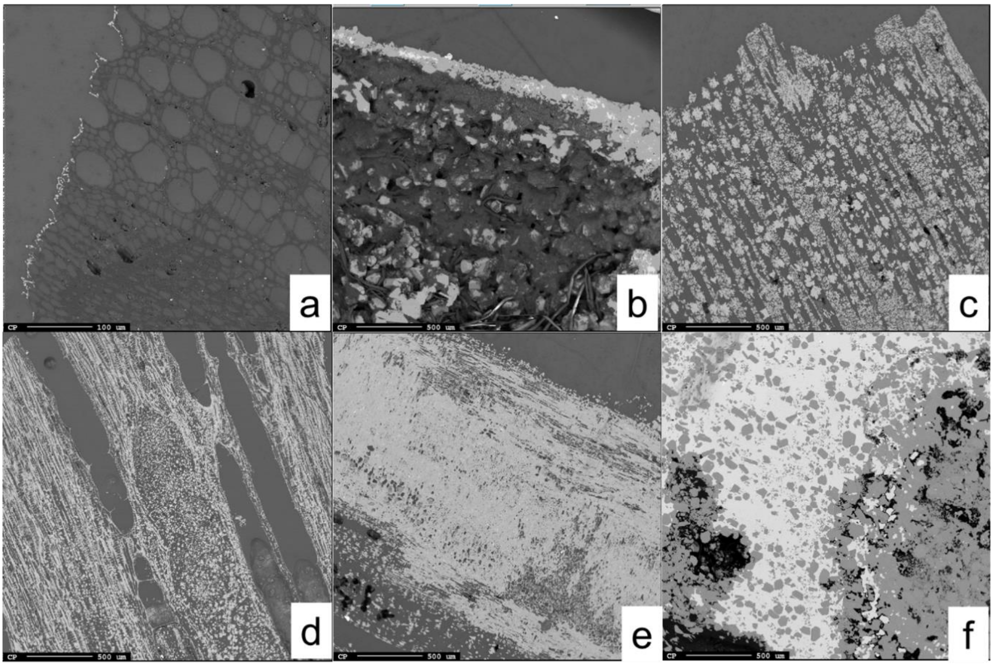

Figure 51. BSE images of materials from charcoal as they are transformed to SiC. In (a) and (b) the particle is mostly carbon with some SiC forming on the outer edge of the particle. In (c) and (d) the particles are highly converted to SiC. In (e), (f), and (g) the "particle" is mostly silicon mixed with SiC with no carbon remaining.

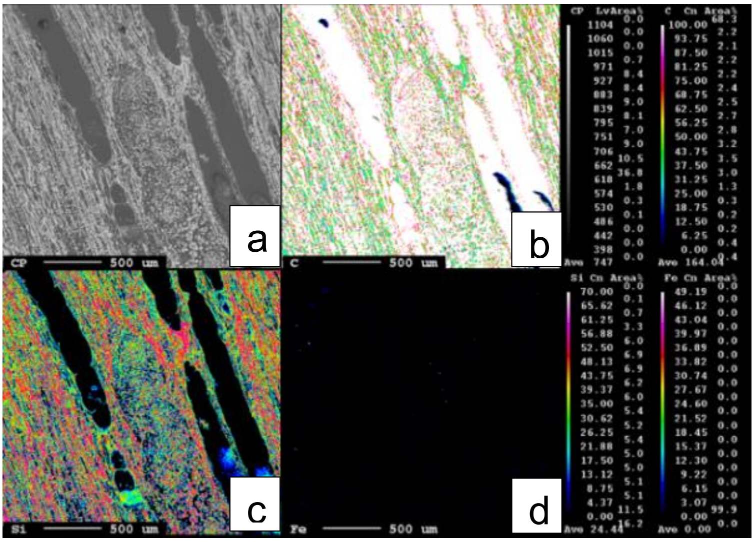

Figure 52. EMPA of the middle areas of the crucible of SiC material from charcoal. The BSE image (a) is the same as Figure 51 (d) shows areas of SiC and carbon. In (b) it can be seen based on the color gradient that carbon is throughout the particle corresponding to the SiC around the pores. In (c) the pink areas show silicon presence that align with the carbon presence in (b) with no areas of elemental silicon. In (d) it shows that there is no iron present.

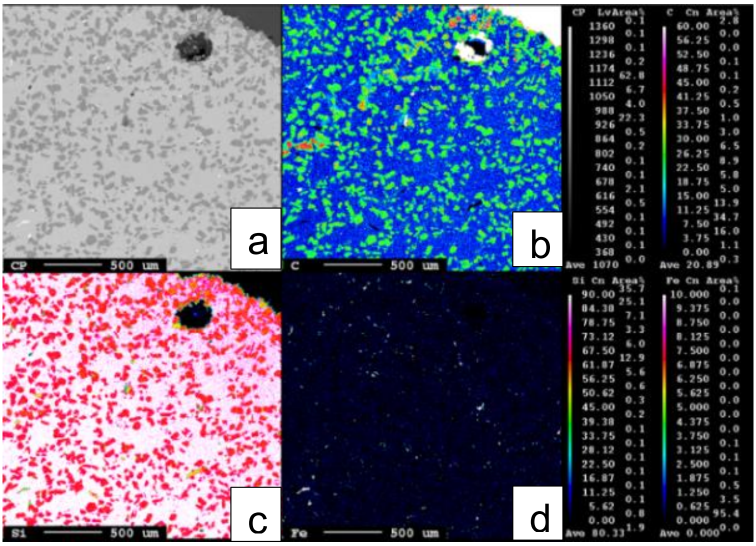

Figure 53. EPMA elemental mapping of the lower areas of the crucible of SiC material from charcoal. The BSE image is the same as Figure 21 (h) and shows mostly silicon with no carbon structure. In (b) it can be seen based on the color gradient that carbon is throughout the particle corresponding to the SiC and there is no remaining free carbon. In (c) the pink areas show silicon presence that align with the carbon presence in (b) but the area is mostly elemental silicon. In (d) it shows that there is some iron present.

The CT images, photographs of the samples, and BSE from particles of the SiC materials from charcoal are shown in Figures 54-55. In Figure 54 (a) and (b), the particle of interest is outlined in red. The particle is shown close up in (c) and the BSE is shown in (d). The CT shows what appears to be one dark gray phase throughout the particle. While it is also not possible to tell the exact location of the BSE image on the particle, it is clear that the darker gray phase on the CT corresponds to carbon in the BSE. The very thin line of SiC on the BSE cannot be seen on the particle in the CT, likely because it is so thin. In Figure 55 (a) and (b), a different particle from the same CT scan is outlined in red. The particle is zoomed in (c) with the border in red that shows the BSE image in (d). The BSE image reveals the particle to be entirely SiC. This corresponds to the light gray color on the CT that is hard to distinguish from the epoxy, however due to the recognizable structure of charcoal it can be seen. This makes it likely that in the CT the darker areas correspond to carbon, and the lighter areas that are similar in color to the epoxy but have the characteristic charcoal structure are likely SiC.

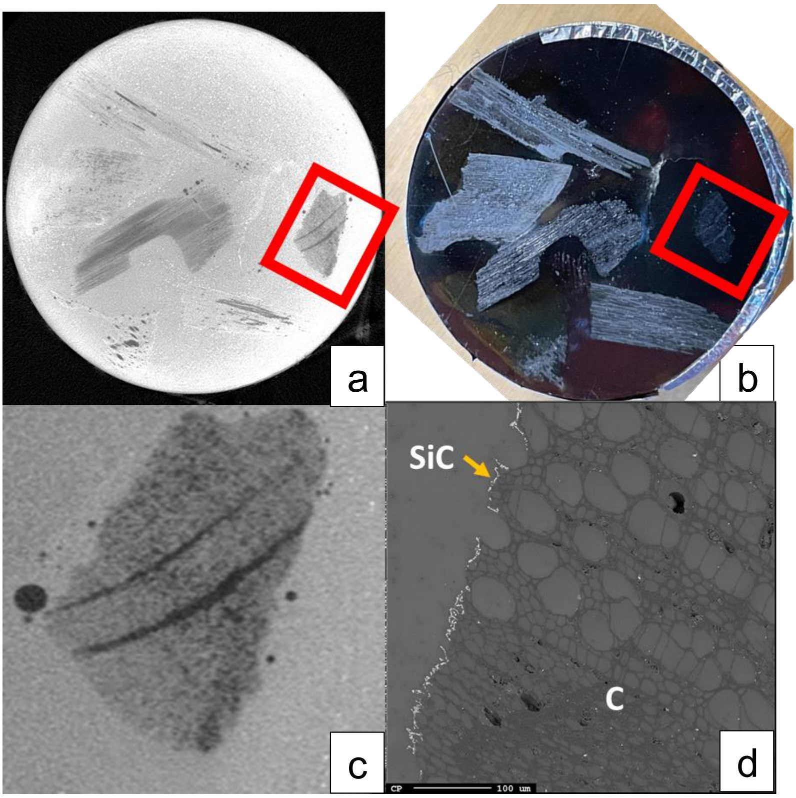

Figure 54. In (a) the overall CT slice is shown for particles from the 60%SiC 6%Si from charcoal sample with the particle of interest outlined in red. In (b) the image is shown with the particle of interest outlined in red. In (c) the particle of interest is zoomed in and the BSE image is shown in (d).

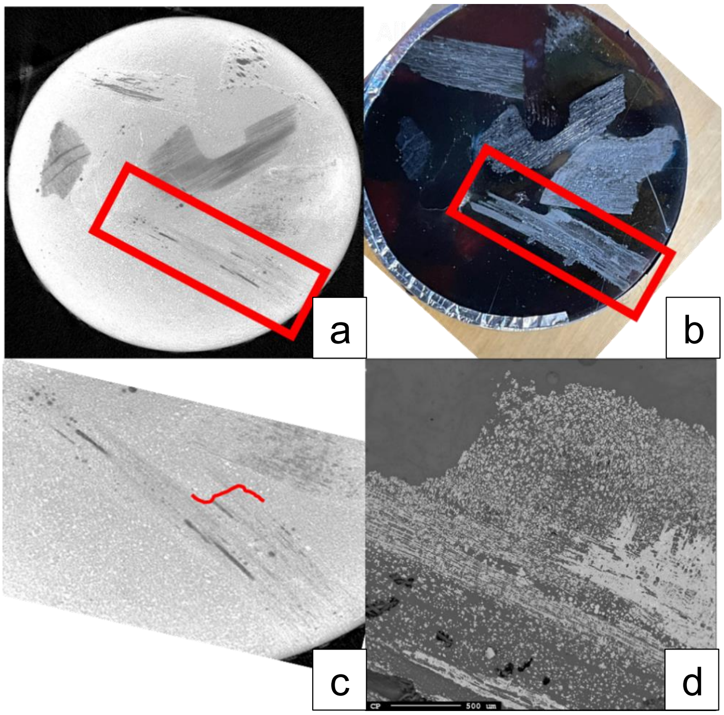

Figure 55. In (a) the overall CT slice is shown for particles from the 60%SiC 6%Si from charcoal sample with the particle of interest outlined in red. In (b) the image is shown with the particle of interest outlined in red. In (c) the particle of interest is zoomed in, and the BSE image is shown in (d). BSE showed that the particle was entirely transformed to SiC.

3.2.4 Bulk density

The bulk density, loosely packed, versus the SiC content of most of the partially transformed materials is shown in Figure 56. Coal based samples are blue, char is green, and charcoal is orange. Diamond markers indicate the presence of silicon. The results show no clear trend. The presence of silicon may increase the bulk density.

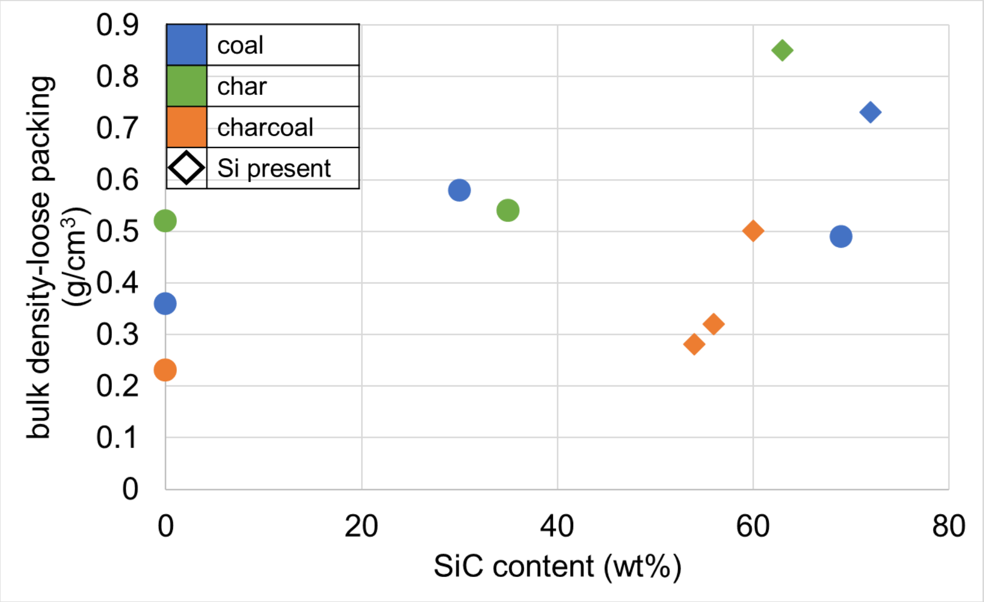

Figure 56. The bulk density of partially transformed materials with increasing SiC content. Coal samples are blue, char is green, and charcoal is orange. Diamond markers indicate the presence of silicon.

3.2.5 Overall Transformation of C to SiC

Sample layers from one batch each of coal and charcoal were studied separately to study SiC formation in large scale setups. The temperature was kept constant at 1850 °C and the holding time was varied from 1-3 hours. However, no clear results were discovered. More results of this work will be shown in Appendix A, but Figures 57-58 show the mass distribution of each layer from each of the samples and each layer is labelled with it's SiC and Si content. The blue represents the top layer, the orange represents the middle layer, and the gray represents the lower layer. Here it is seen that there is not a large difference in the total transformation between the two carbon types, or between the different holding times. In general it does appear that the charcoal sees more transformation in the lower layers than the top layers, whereas the coal showed more similar trasnformation throughout the middle and lower layers. However, this method is not accurate enough to be used to show the difference in reactivity between the carbon materials.

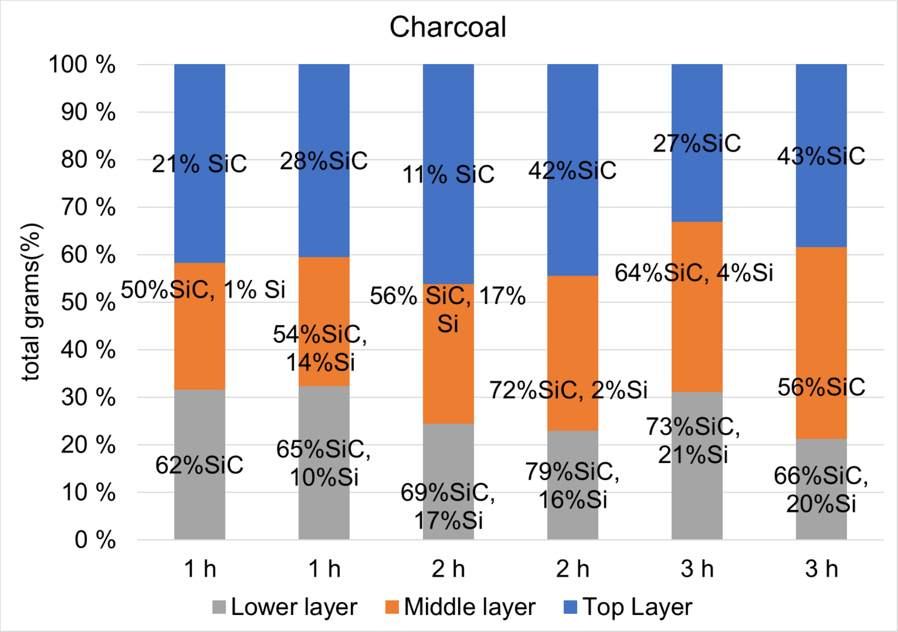

Figure 57. Distribution of layers from charcoal experiments, with the top layer in blue, middle layer in orange, and the lower layer in gray.

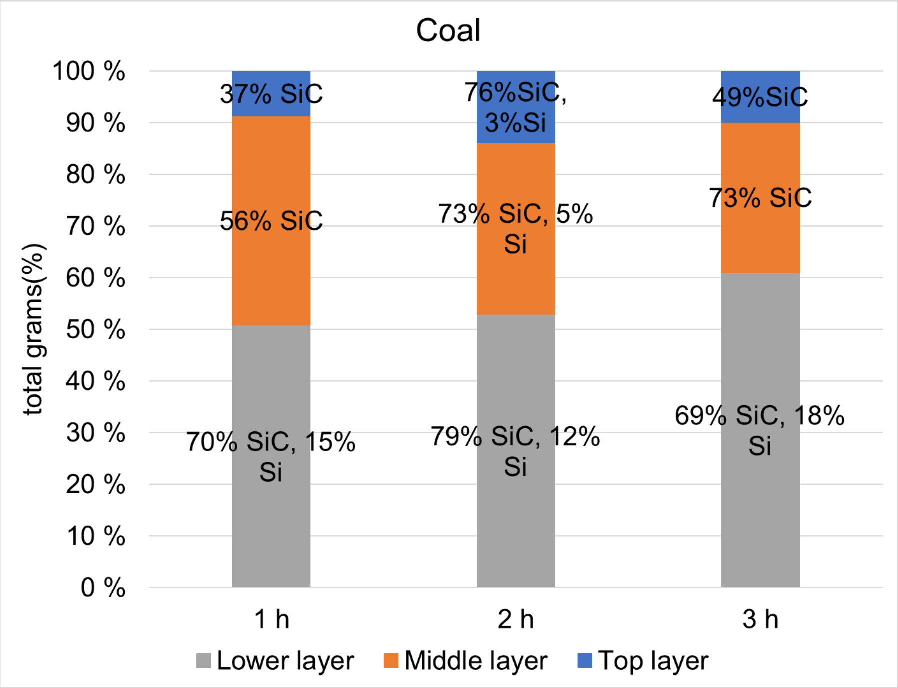

Figure 58. Distribution of layers from coal experiments, with the top layer in blue, middle layer in orange, and the lower layer in gray.

4 BULK RESISTIVITY IN A BED OF PARTICLES

This chapter describes the thesis work regarding measurement of bulk resistivity. The carbon materials and partially transformed SiC described in Chapter 3 provide the materials used for the resistivity measurements. The goal was to build on the well-established resistivity of carbon materials and show how their transformation to SiC and the presence of silicon changed the resistivity of the bed. Furthermore, the resistivity of the charge mixtures is also of interest. The resistivity of char mixtures of char, quartz, woodchips (charcoal), and silica-iron ore were hence also measured.

4.1 MATERIALS, APPARATUS, AND METHODS

The materials used for all the resistivity measurements (including those already introduced in Chapter 3) are explained, followed by the methods used for measuring the resistivity. Meggi Glowacki and Khadija Choudry contributed to the work in this section through physically aiding or performing some of the experiments and their work is included as a part of the total study. Furthermore, Mads Fromreide developed and executed the CT comparison method that will be used to describe the movement in the bed before and after measurement. The author is responsible for supervising and for interpreting the results from Glowacki and Choudry.

4.1.1 Materials

The total list of materials tested in this work are shown in Tables 9-11. The chemical analysis of the raw materials used in this work are shown in Table 12. For the charge mixes, the relative weight ratios of the materials are listed. The amount of woodchips was reduced due to the large volume change that was expected to reduce the volume of the sample below the measuring zone. The notation “HT” means the material was heat treated beforehand, as described in Chapter 3. The “charcoal from woodchips” also called “homemade charcoal” was recovered from the previous resistivity measurements that included woodchips. When additional homemade charcoal was needed, woodchips were heat treated separately according to the same temperature program in the induction furnace. A loose cover was used to prevent too much oxidation. Particle size used for resistivity measurements was 4-8 mm, and materials were crushed using a jaw crusher and then sieved if needed.

Table 9. List of the number of experiments done on each of the carbon materials. "HT" denotes heat treatment. Different samples of the same carbon material are differentiated using A, B, or C.

Number of experiments	Carbon materials	FixedC (%)	Ash (%)	Volatiles (%)
1	CharA	88.5	5.87	5.4
1	CharA HT			
4	CharB HT*	96.2	1.2	2.6
4	CharC*	86.9	11.8	1.2
1	CharcoalA	85.9	3.97	15.9
1	Charcoal from woodchips*	91.4	4.9	3.7
1	CharcoalB*	81.8	0.03	16.2
1	Coal HT	95.3	2.28	0.4

*indicates the experiment was run by Meggi Glowacki

Table 10. List of materials used in the bulk resistivity measurements. Number of experiments shown in parentheses

SiC materials from charcoalA	SiC materials from charA	SiC materials from coal
60 %SiC, 6 %Si** (3)	32 %SiC (1)	69 %SiC (5)
60 %SiC, 36 %Si (4)	35 %SiC (2)	72 %SiC, 7 %Si (4)
54 %SiC, 6 %Si (2)	63 %SiC, 2 %Si (3)	30 %SiC (2)
56 %SiC, 14 %Si (1)		

**indicates the experiment was run by Khadija Choudry

Table 11. List of the number of experiments done on each of the charge mixtures. Weight ratios are listed in the same order as the materials.

Number of experiments	Charge mixes
7	1:1.8char+quartz*
4	1:1.2char+quartz*
2	1:0.5char+quartz*
3	1:1.8:0.5char+quartz+woodchips (charcoal)*
7	1:1.8:0.57char+quartz+silica/iron ore (+charcoal)*
3	1:0.57char+silica/iron ore*

*indicates the experiment was run by Meggi Glowacki

Table 12. Chemical analysis of Quartz A and Silica-Iron Ore A/B for the charge mixes (wt%)

	Quartz A		Silica-Iron Ore A	Silica-Iron Ore B
	Wt%		(Wt%)	(Wt%)
SiO_2	99.8	SiO_2	46.3	61.8
MgO	0.02	MgO	6.72	3.57
Al_2O_3	0.04	Al_2O_3	11.4	6.91
Fe_2O_3	0.14	Fe_2O_3	7.42	19.5
Cr_2O_3	0.04	CaO	22.5	4.96

4.1.2 Apparatus

The experimental setup for bulk resistivity measurements is shown in Figure 59. Contained within the graphite crucible is an alumina tube (not to be confused with the small alumina tube used to house the thermocouple or Mo wires) which acts to insulate the charge from the graphite crucible walls. A four-point measurement system is used to eliminate contact resistance between the samples and the electrical contact points through measuring voltage and current in two different places [6]. Molybdenum (Mo) wires are placed across the length of the alumina tube (8 cm wide) 10 cm apart from each other and the sample is loaded to cover both wires to measure the resistivity of the bulk. The main thermocouple is placed through the top electrode and embedded in the center of the sample. An additional “outer” thermocouple is placed between the alumina tube and the inside of the graphite crucible. This outer thermocouple controls the heating rate of the furnace to ensure the stability of the equipment. A stainless-steel weight sits atop the graphite block to provide even total pressure. The graphite block acts as the top electrode, with the bottom of the graphite crucible acts as the bottom electrode. The graphite acts as the "outer circuit" in the four-point measurement setup, with the Mo-wires acting as the independent "inner circuit" that is separated from the current supply. The area between the wires is what is considered the measuring zone.

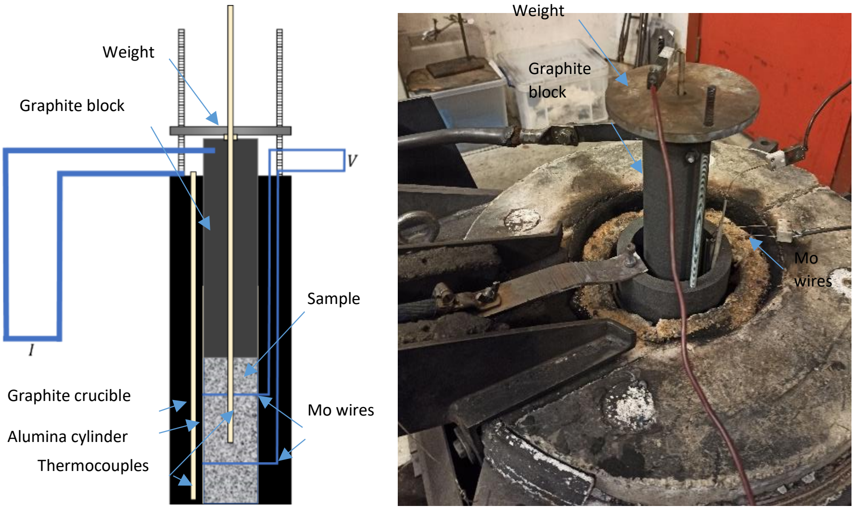

Figure 59. Schematic (left) of the setup used for bulk resistivity measurements. A picture of the resistivity setup from the laboratory (right). The graphite crucible is 40 cm in height with a 15 cm outer diameter and 11.5 cm inner diameter. The alumina tube is 30 cm in height with an 8 cm inner diameter.

Since one thermocouple is embedded in the center of the setup and another is placed close to the outer wall of the graphite crucible, a radial temperature gradient is measured as shown in Figure 60. Additionally, the sample is heated with two different heating rates, depending on temperature. Shown in Figure 60 is a temperature log from the sample containing 63 %SiC 2 %Si made from char. The heating program, shown in orange, begins at a slower rate of 3 °C/min, then holds at 250 °C for 10 minutes, then speeds up to 13 °C/min until 1600 °C is reached. This was done to minimize thermal stresses on the alumina tube. The temperature in the sample is lower, but the difference decreases as the maximum temperature is reached. Often, the sample will continue to heat up for a short period after the furnace has been shut off, which is why the sample rises to 1600 °C when the outer thermocouple begins to measure a decline in temperature. The programmed temperature drops to zero when the program is restarted, which can happen any time the furnace is shut off. The furnace could be momentarily shut off for safety reasons if the Mo wires for example need to be adjusted.

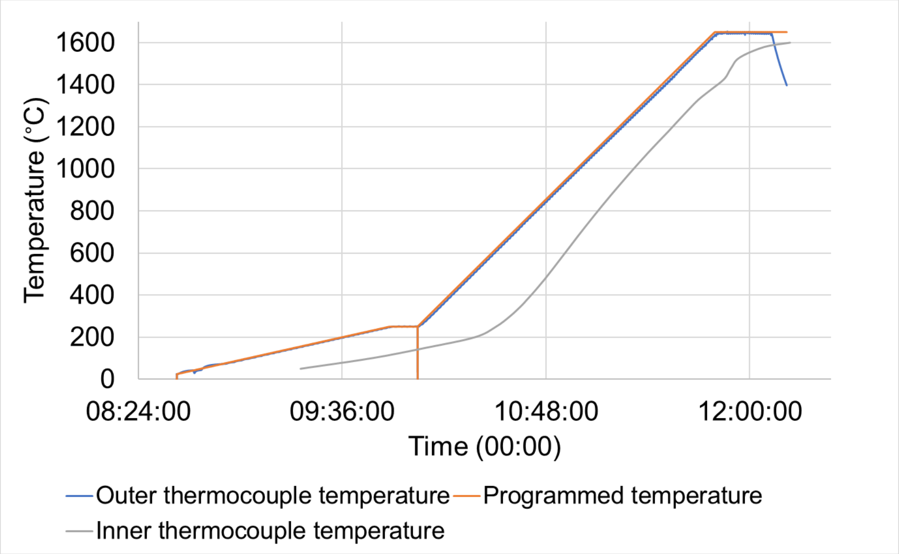

Figure 60. Temperature curve for the resistivity measurement of 63 %SiC 2 %Si from char, run 2b. The outer thermocouple is blue, the programmed temperature is orange, and the inner thermocouple temperature is gray.

4.1.3 Methods

This method is based on the work of SINTEF, which was improved by Pedersen [66]. The Mo wires are laced through the alumina tube and covered with additional alumina tubes before it is placed in the graphite crucible. The empty space between the walls of the two crucibles is then packed with Styrofoam to ensure it does not move or break during the setup. The sample is then top loaded into the alumina tube, followed by the thermocouple and the graphite block. To reduce the variations in the measurements, after the sample and block are loaded, the setup is manually compacted by dropping the setup onto Styrofoam from a height of 10 cm for 40 drops. The change in height as a function of the number of drops is shown in Figure 61 for 72 %SiC, 7 %Si from coal. After 40 drops the change in the bed begins to plateau and is considered to be sufficiently compacted. This of course has some variability depending on the strength of the material. The setup is then placed in the induction furnace (the same furnace that is explained in Chapter 3) along with the outer thermocouple and the stainless-steel weight. The graphite is then attached to the power source, which was a Kempower IPM15 welding transformer. The Mo wires are attached to a NI TB-9214 module for measuring the voltage.

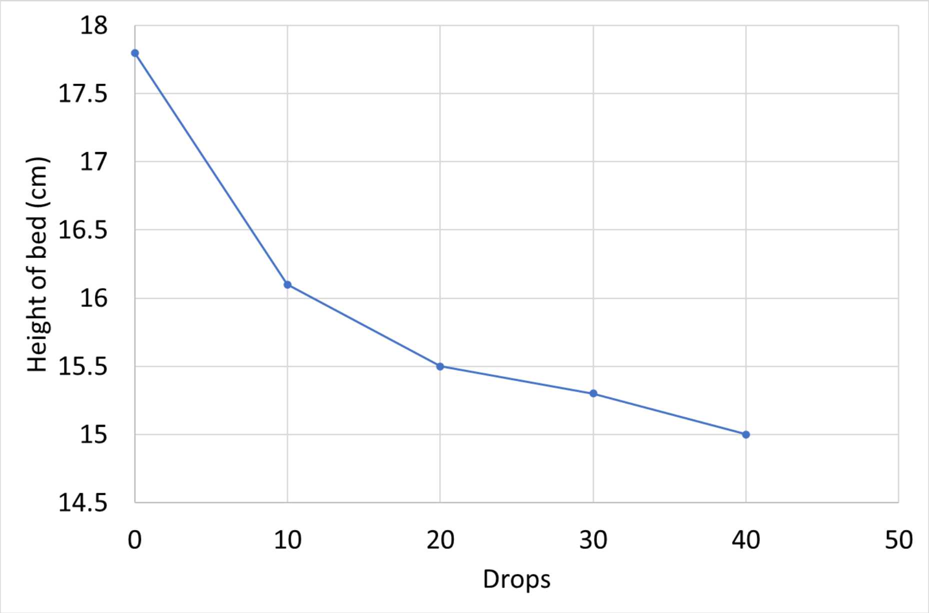

Figure 61. Graph showing the bulk resistivity at room temperature and the height of the particle bed as a function of the numbers of compaction drops.

The software used to control the resistivity measurements was developed by SINTEF. The software allows the user to input the maximum current and frequency of the measurements. The maximum current output was 100 A and the measurements were taken every 25 °C. A room temperature test is normally done to ensure that the pulse trains exist, and current is running through the setup without any issues. This is done in case wires need to be adjusted for better contact or if there is a problem with the software. After ensuring the setup is functioning, the induction furnace heating program is started, and the resistivity software is set to run every 25 °C. The experiment is monitored throughout in case adjustments need to be made.

For some of the experiments, the distance between the Mo-wires was 8 cm instead of 10 cm due to the lack of partially transformed materials, and no significant difference in resistivity was found between the two distances. The new length was accounted for in the resistivity calculations. The 10 cm measuring zone was reinstituted and instead the distance between the bottom Mo wire and the bottom of the alumina cylinder was shortened. This had the same effect of reducing the amount of material needed to perform an experiment. Additionally, fines were sometimes loaded below the bottom Mo wire to further reduce the amount of material needed. These could then easily be sieved out after the experiment.

The experimental procedure applies current in pulses every 25 °C so the voltage drop between the two wires can be measured. Figure 62 shows an example of a typical pulse train at any given temperature with respect to time using the sample containing 63 %SiC 2 %Si made from char at 1325 °C. Also shown on the graph by the red dotted line is the 1 V threshold, under which the data is filtered out for calculations, because this is idle time where the current is negligible. The resistance is calculated from the average voltage and current. Outliers in the pulse trains exist, but with a set of over 3000 data points, the removal of the outliers did not significantly change the result. Several samples were run multiple times. In some cases, the setup was not altered in between the measurements. In others, the setup was disassembled in between the measurements so the sample was essentially repacked into the setup with a different packing configuration. This will be discussed in the results. Samples were sieved in between measurements if fines were a factor. Averages and standard deviations, when presented, include all runs of the material.

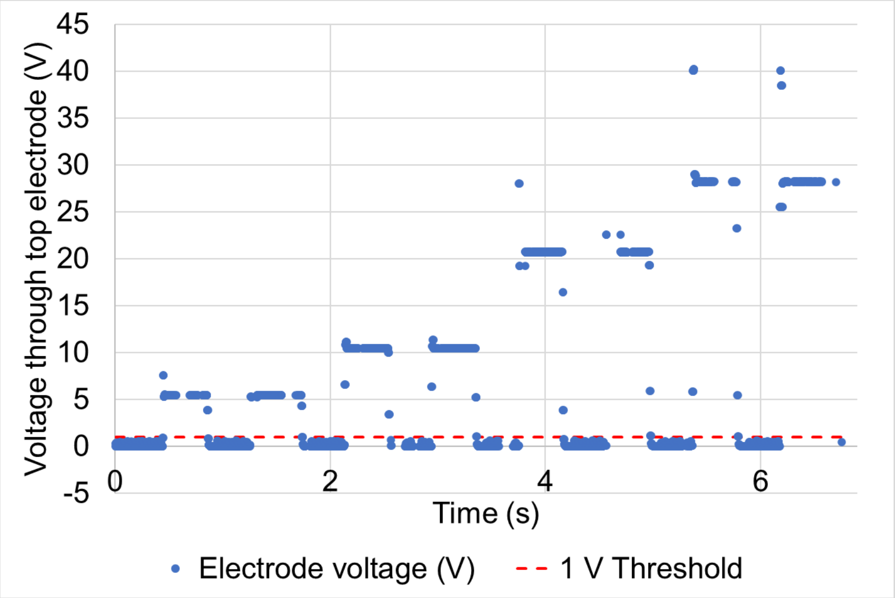

Figure 62. Graph depicting a sample pulse train from bulk resistivity measurements with the 1 V threshold shown in red. This is from 63 %SiC 2 %Si from char, run 2b, 1325 °C.

CT scans were taken of some of the crucibles before and after resistivity measurements. The scans were taken to evaluate the potential changes occurring during resistivity measurement that may affect the results. This includes changes in the wiring, placement of the thermocouples, shifting of material or of the alumina tube, and notable particles or signs of chemical reaction. This led to a modification in the procedure. Initially, the thermocouple was placed after compaction using a steel rod as a guide and then inserting the thermocouple. However, a CT scan of the 69 %SiC material from coal showed a bending in the top Mo wire. Afterwards, the alumina tube housing the thermocouple was placed before compaction, with the thermocouple being inserted afterwards. This fixed the bending in the top wire, as is shown in Figure 63 using a scan of 60 %SiC 6 %Si from charcoal. Figure 63 also shows that the thermocouple is placed lower in the bed using this method, since it will also shift down as the bed in compacted. Future experiments placed the thermocouple 2-3 cm higher to account for this, but there is some variation based on how much the height changes during compaction. Most samples saw a change in height of between 2-3 cm, so the thermocouple likely has ±1 cm difference in the bed for any given material.

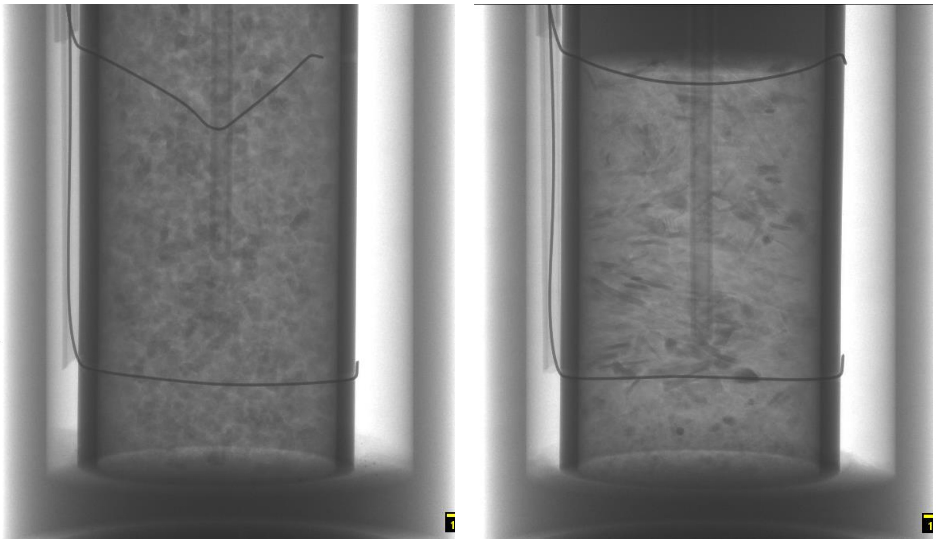

Figure 63. Unprocessed CT image of 69 %SiC from coal with the visible bending in the wire (left) and the 60 % SiC 6 %Si from charcoal with the readjusted method to keep the wire straight (right).

In order to quantitative determine the difference of the bed before and after, a method was developed by Mads Fromreide at NORCE that included the following steps:

- Aligning the images using landmarks such as the alumina cylinder and the molybdenum wires
- Converting the dataset to binary using a given threshold to determine if a voxel contained a particle and assigning it a "1" value if yes and a "0" value if not.
- Subtracting the after from the before scan, if there is no change, black is coded, material "appears" in the after is green, and "disappearing material" is red.

A simplified example of this is shown in Figure 64. If you start with a stack of particles (blue squares) in an enclosed space, you have areas where there is a particle and where there is empty space. After some external stimulus, there is a shift in the particles. If the method above is applied, it becomes clear based on the green and red that the material shifted to the left, as it disappears (red) on the right and "appears" green on the left.

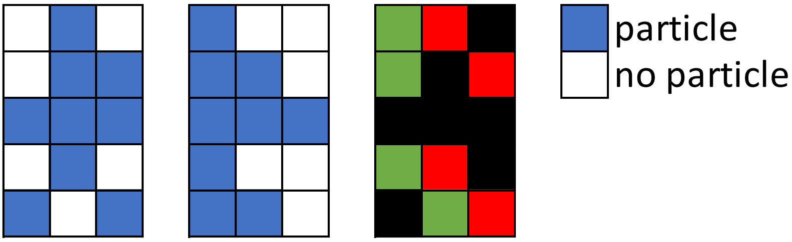

Figure 64. A simplified example of determining the material shift in an enclosed space using black for "no change", green for "appearance" of material, and red as "disappearance" of material.

Chemical analysis and EPMA WDS were used to characterize the SiC, C, and Si content of the materials and the slag composition in the charge mixes, respectively. The CT and EMPA characterization methods were described in Chapter 3 and will not be repeated here.

4.2 RESULTS

The resistivity curves for each grouping of materials are shown from 25-1600 °C and 1000-1600 °C. Temperatures from 25-1000 °C are taken every 50 °C, and from 1000-1600 °C every 25 °C. The high temperature area was chosen due to its relevance for the Si process. At lower temperatures, the resistivity will be higher, and have higher variation. Graphs of the averages of the partially transformed SiC material with standard deviation are also shown. Multiple measurements of the same material are differentiated using numbers and letters. The number indicates the experiment number *in that specific configuration*, and the configuration is specified by the letter. For example, the first time a material is measured it is designated as "1a". If the material is measured again *without* repacking, it will be 2a. If the material is repacked, it becomes "1b".

4.2.1 Resistivity of carbon materials

Figure 65-67 shows the resistivity of all the carbon materials (heat treated coal, char, and charcoal) versus temperature. Char is shown in green (Figure 66) and includes both heat treated and untreated char from three sources, charcoal is orange (Figure 67) and includes two industrial charcoals and one that was made in the lab from woodchips, and coal is blue (Figure

65) and includes only heat-treated coal from one source. The results show reasonable grouping among the various carbon materials, regardless of if the material was char A or char B for example. There is a difference if the material was heat treated, as the presence of volatiles will increase the resistivity. The heat-treated chars and the coal had a similar resistivity throughout the temperature range. Charcoal on the other hand, was nonconductive (over 1000 mΩm) until around 1000 °C, where the resistivity then decreases rapidly with increasing temperature. At 1600 °C, there is an area where all three materials overlap that ranges between 10-15 mΩm, with the exception of the homemade charcoal, which was higher. Overall, the charcoals have the highest resistivity over the temperature range, and the heat-treated chars and coal seems to be within the same range of each other.

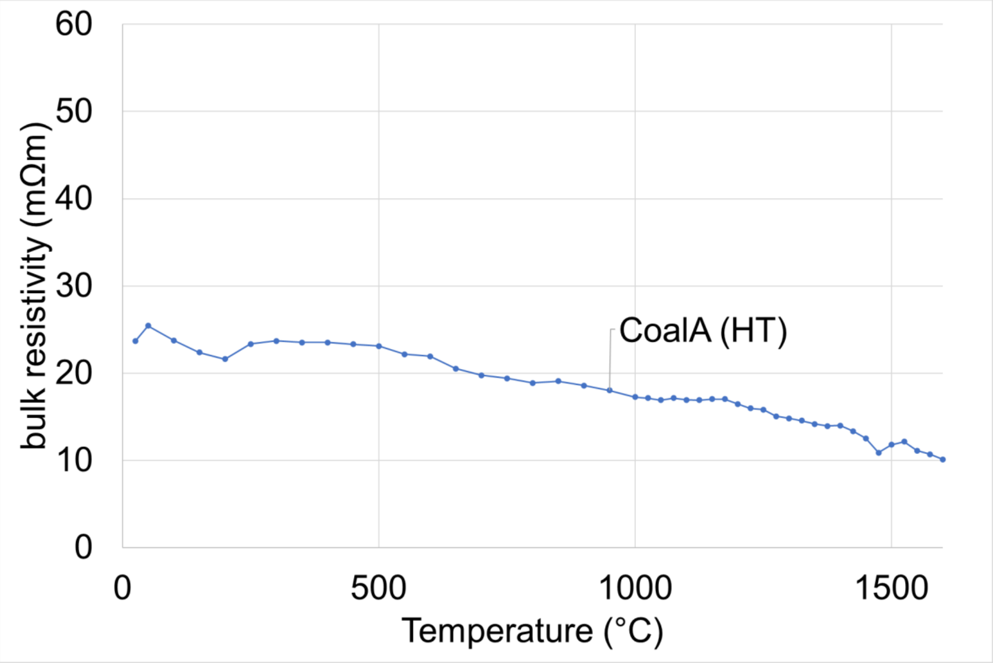

Figure 65. Resistivity with increasing temperature of Coal A (HT)

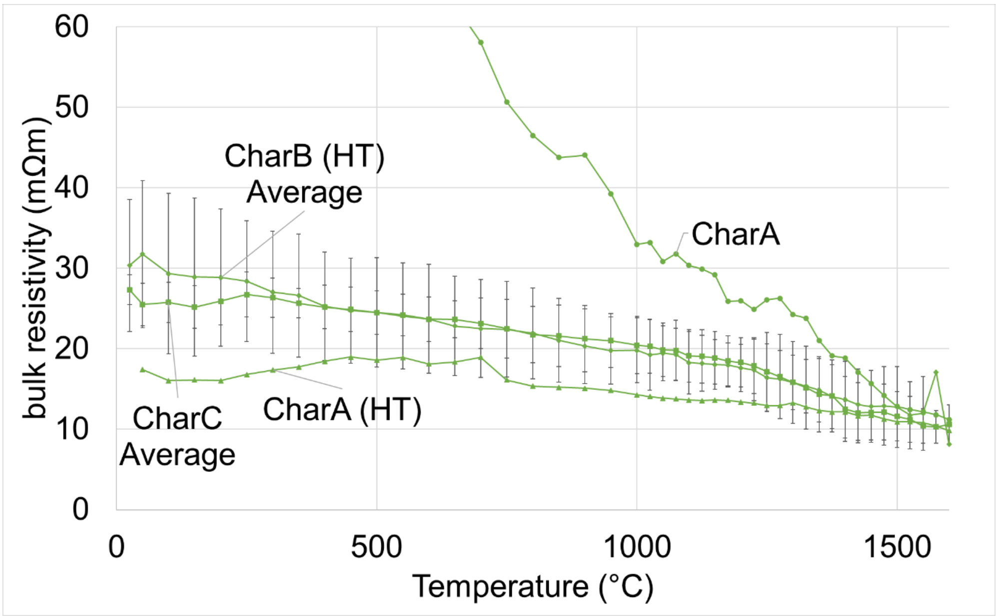

Figure 66. Resistivity with increasing temperature of all chars, both untreated and heat treated.

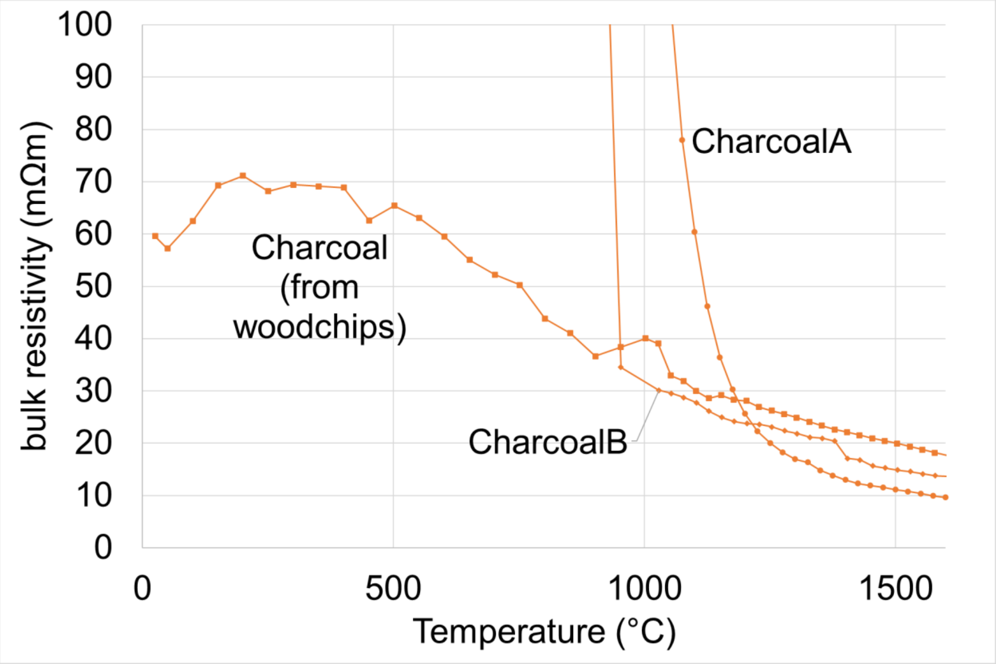

Figure 67. Graph of resistivity versus temperature for two industrial charcoal samples and one sample made in the lab from woodchips.

The homemade charcoal from recovered woodchips had a higher resistivity than the industrial charcoals after around 1200 °C, but it was conductive over the entire temperature range. This is likely because the “homemade” charcoal has been heat treated at 1600 °C, compared to charcoal’s typical manufacturing process. This resulted in a higher fixed carbon and lower volatiles. CharcoalB shows a similar trend to other charcoals, where a steep decrease is seen as the material becomes conductive as 1000 °C is approached. However, in the CharcoalB sample, this sudden drop in resistivity happens at a lower temperature, closer to 900 °C.

Figure 68 shows the resistivity of three types of char. The graph on the left shows untreated material and the graph on the right shows chars that were heat treated at 1200 °C for approximately 15 minutes in batches before the experiments. The untreated samples include CharA and CharC. CharA has a higher resistivity than CharC, whereas CharC, despite being untreated, has a similar resistivity to the heat-treated chars. According to Table 9, CharC has a lower volatiles content than CharA, indicating that it was produced at a higher temperature. Therefore, the resistivity could be less sensitive to temperature, similar to what is seen in the heat-treated materials, which presumably had most of their volatiles released during the previous heat treatment and not during the resistivity measurement. CharC also has the highest ash content, but this does not show any effect. At 1600 °C, all chars fall into the range of 7-11 mΩm.

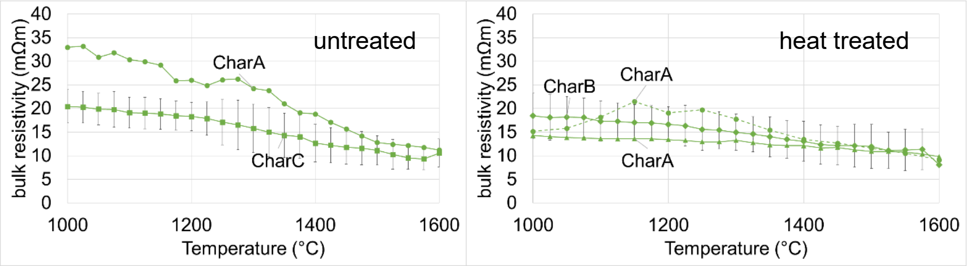

Figure 68. Graph of resistivity versus temperature for untreated (left) and heat treated (right) char samples. With the heat-treated samples, the dotted line is the result from Pedersen [7], who treated his materials to 1200 °C for 15 minutes. This method was also used for CharB. CharA was a repeated trial of the CharA run on the left, therefore the heat treatment temperature is 1600 °C.

4.2.2 Resistivity of partly transformed C to SiC materials

Figures 69-71 show the results of the resistivity of SiC materials from coal. The SiC content ranges from 30-72 % and silicon is present in the 72 % samples. The original heat-treated coal is also shown. The results show that the carbon material's conversion to SiC raises the resistivity, and upon the formation of elemental silicon, the resistivity begins to decrease. Both the individual experiments (Figure 69-70) and the materials as an average (Figure 71) are shown to display the trends and explain any variations more clearly. The two samples with high SiC content are 6 9% and 72 %SiC, which are close in value. It appears that the 69 %SiC may have the slightly higher resistivity in general. Therefore, the silicon that is present in the 72 % sample is likely responsible for the lower resistivity. The different trials of the same samples show good agreement, even when the experimental packing is changed. The 30 % SiC samples show slightly different results, with one experiment having a higher resistivity than the coal, and another having a slightly lower resistivity. This could be because of differences in packing or bulk density, or there simply is not enough SiC in the sample to discern if it fits the trend seen in the other two samples. When the average is taken of each of the materials, as shown in Figure 71, the trend of increasing resistivity with increasing SiC content remains true, with the HT coal being within the standard deviation of the 30 %SiC. The overall differences in resistivity between the coal and the SiC material decreases as the temperature increases. The CT scan of the crucible before and after (Figure 72) shows no discernable changes in the bed, aside from a slight shifting in the top of the bed, which could have happened during transport. This implies that any variations are due to the measurement method and not due to shifting or additional transformation of the material.

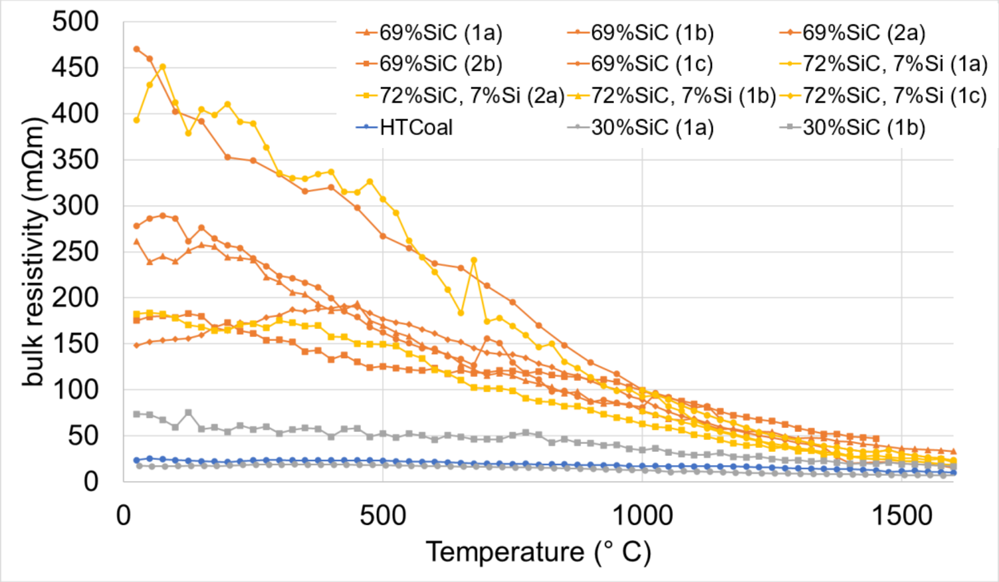

Figure 69. Resistivity with increasing temperature from 25-1600 °C for all SiC materials from coal and HT coal. The 69 %SiC samples are orange, the 72 %SiC 7 %Si samples are gold, the 30 %SiC samples are gray, and the HT coal is blue.

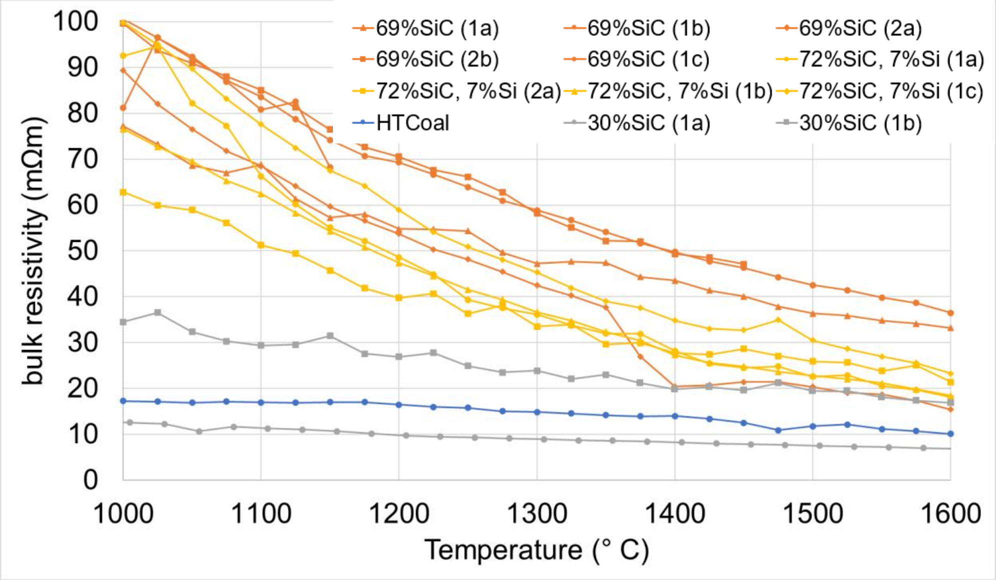

Figure 70. Enlarged part of Figure 11 showing resistivity with increasing temperature from 1000-1600 °C for all SiC materials from coal and HT coal. The 69 %SiC samples are orange, the 72 %SiC 7 %Si samples are gold, the 30 %SiC samples are gray, and the HT coal is blue.

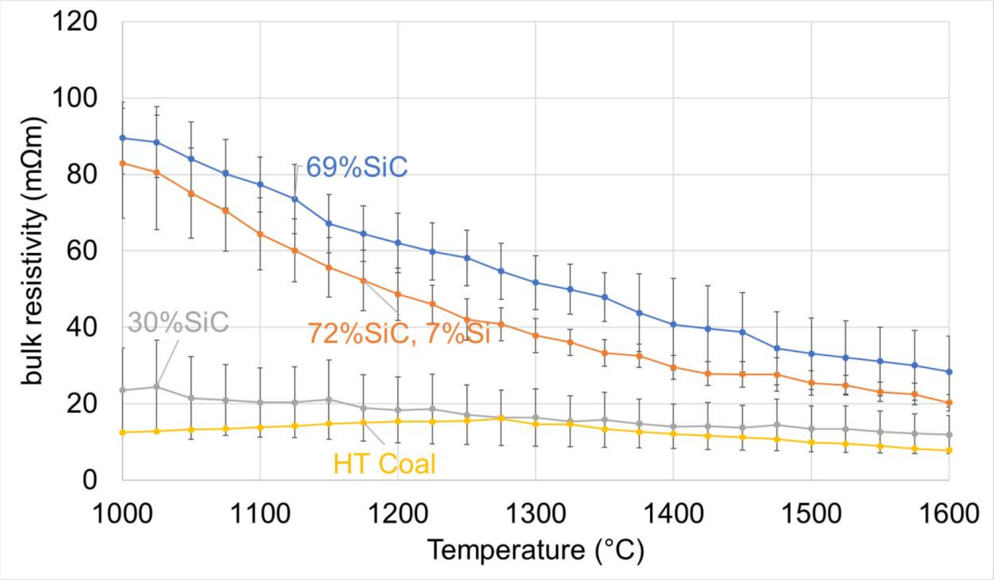

Figure 71. Average resistivity with increasing temperature from 1000-1600 °C for all SiC materials from coal and HT coal. The 69 %SiC samples are blue, the 72 %SiC 7 %Si samples are orange, the 30 %SiC samples are gray, and the HT coal is gold.

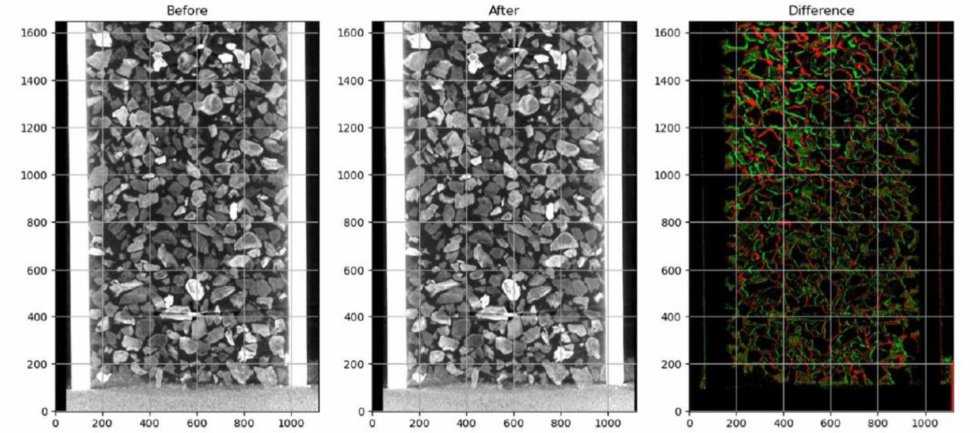

Figure 72. CT scans in YZ axis before (left) and after (middle) measuring resistivity of 69 %SiC from coal, and the calculated difference between the two (right). Green is before and red is after the measurement.

Figures 73-75 show the resistivity for the SiC materials made from CharA. Char and heat-treated char are also shown. At high temperature (Figure 74) the 63 %SiC, which contains some Si is slightly lower in resistivity than the 35 % SiC, but at lower temperatures the reverse is true. This is similar to the trend seen in the coal samples, but at low temperature the resistivity of the 69 %SiC and 72 %SiC from coal samples have the same range of resistivity. The 35 % SiC samples appear to have a similar resistivity to that of untreated char, whereas the 32 %SiC sample is close to that of the heat-treated char. However, the 32 %SiC sample is only measured to 1350 °C due to thermocouple failure during the experiment. A reason for the differences between the 32 %SiC and 35 %SiC could be in their production methods. The 35 %SiC sample all came from a more homogeneous sample, whereas the 32% SiC was a combination of more or less transformed layers that were mixed. This means that while the overall SiC content may be similar, one sample could contain a more heterogenous mix of char particles and SiC particles, and the other could be a more homogeneous mixture of only slightly converted SiC and carbon particles. This could change the current paths in the setup as the results from the coal have led to the possibility that the SiC has a higher resistivity than the carbon. Therefore, the 32 %SiC having more unreacted carbon particles could result in its lower resistivity. Based on the averages shown in Figure 75, above 1300 °C, the char, 35 %SiC, and 63 %SiC 2 %Si are all within the standard deviation of one another.

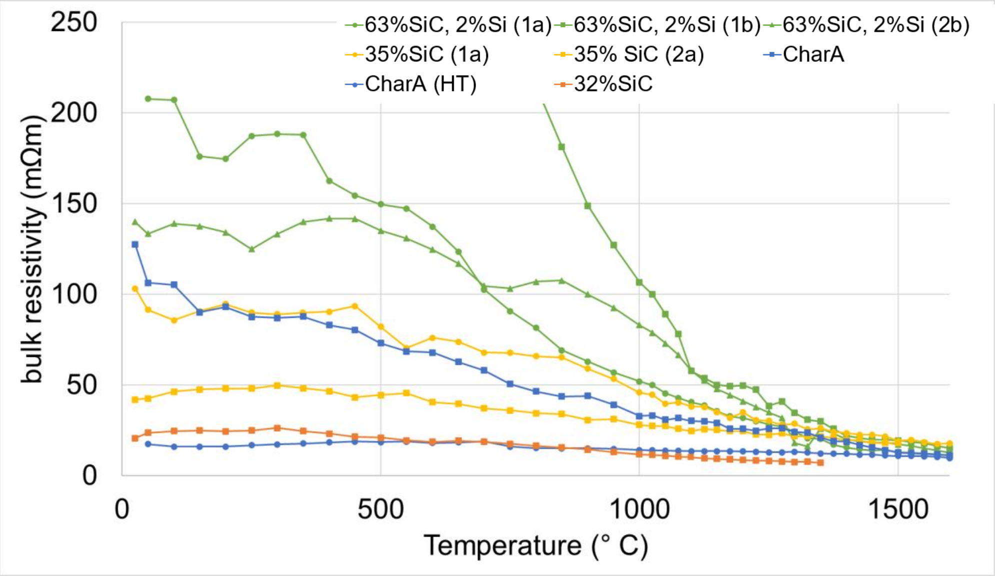

Figure 73. Resistivity with increasing temperature from 25-1600 °C for all SiC materials from char and charA. The 63 %SiC, 2 %Si samples are green, the 35 %SiC samples are gold, the 32 %SiC samples are orange, and the char is blue.

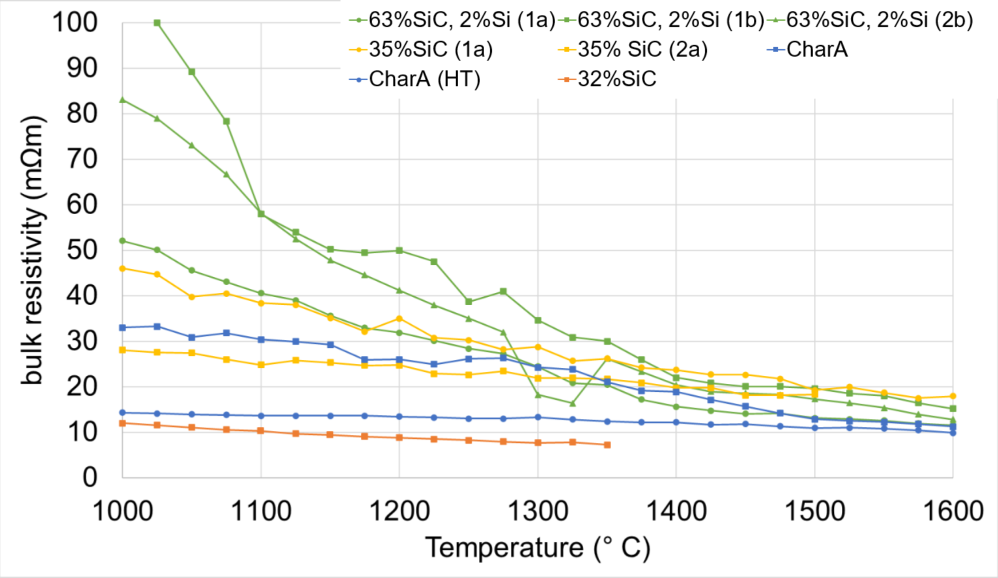

Figure 74. Enlarged part of Figure 15 showing resistivity with increasing temperature from 1000-1600 °C for all SiC materials from char and charA. The 63 %SiC, 2 %Si samples are green, the 35%SiC samples are gold, the 32 %SiC samples are orange, and the char is blue.

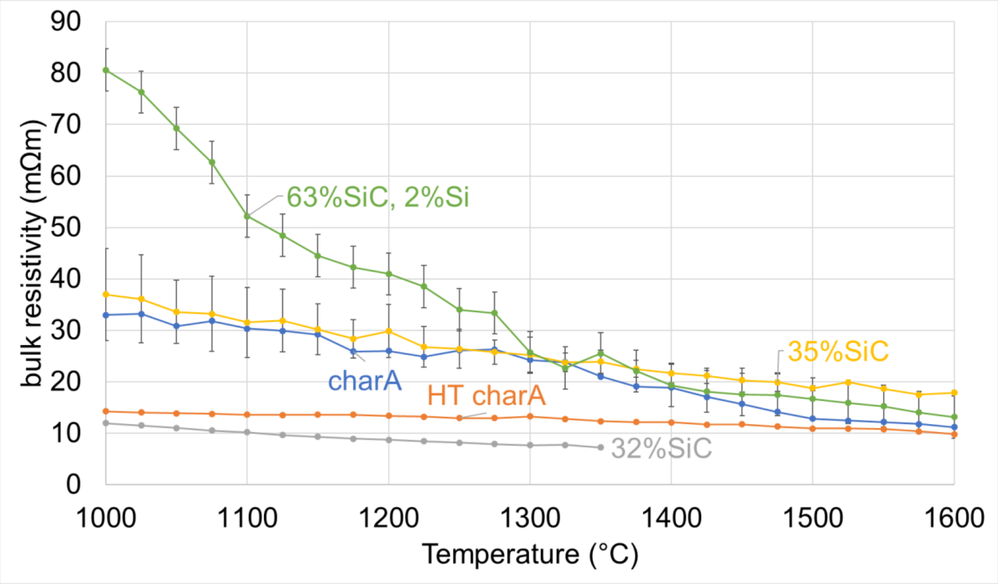

Figure 75. Average resistivity with increasing temperature from 1000-1600 °C for all SiC materials from char and charA. The 63 %SiC, 2 %Si samples are green, the 35%SiC samples are gold, the 32 %SiC samples are gray, and the char is blue, with HT char in orange.

Figures 76-78 show the resistivity for the SiC materials made from charcoal. In addition, charcoal is shown in blue. Two of the SiC materials have the same SiC content, but one has 6 %Si and the other has 36% Si. However, the amount Si seems to have no effect at these temperatures because the materials have similar resistivities. Additionally, the 54 %SiC sample has 6 %Si and has a lower resistivity than the 60 %SiC with the same Si content and the 56 %SiC 14 %Si seems the follow the 60 %SiC 6 %Si closely. If they are examined by their unreacted carbon contents, the three samples contain 4 %, 30 %, 34 %, and 36 % C. This higher carbon content could explain the differences at lower temperature, where the sample with the lowest carbon content has the highest resistivity. However, this effect is lessened at high temperature as all materials, charcoal included, fall within 10-15 mΩm at 1600 °C. This is seen more clearly in Figure 77. If the maximum temperature is lowered to 1575 °C to include the 54 %SiC, the range becomes 6-15 mΩm. The CT scan of the crucible before and after (Figure 79) shows no discernable changes in the bed, which is the same as the SiC from coal results.

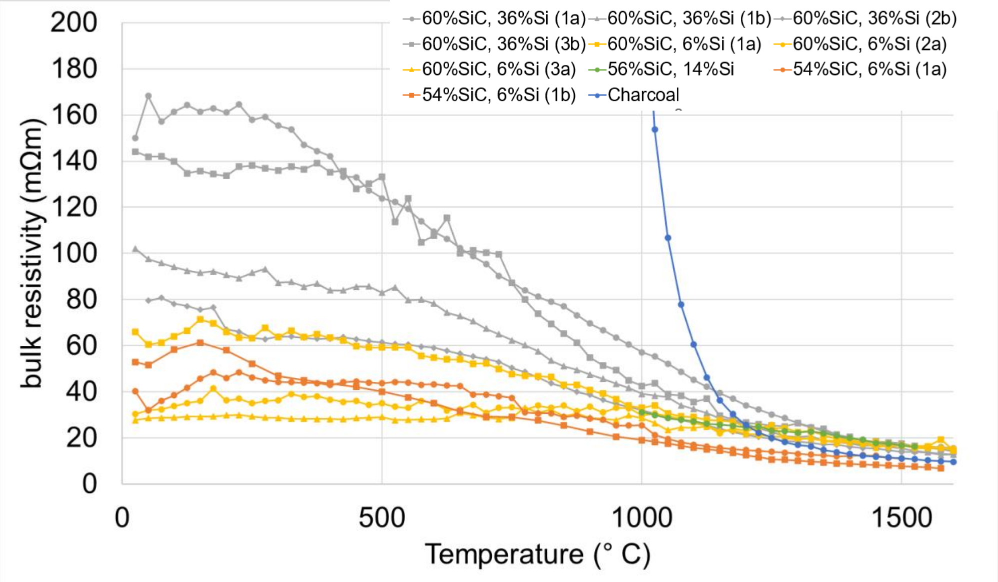

Figure 76. Resistivity with increasing temperature from 25-1600 °C for the partially transformed SiC from charcoal, including charcoal A. 60 %SiC, 36 %Si is shown in gray, 60 %SiC, 6 %Si is shown in gold, 56 %SiC, 14 %Si is shown in green, 54 %SiC, 6 %Si is shown in orange, and charcoal is shown in blue. The 56 %SiC, 14 %Si sample is only shown from 1000 °C due to error during experimentation.

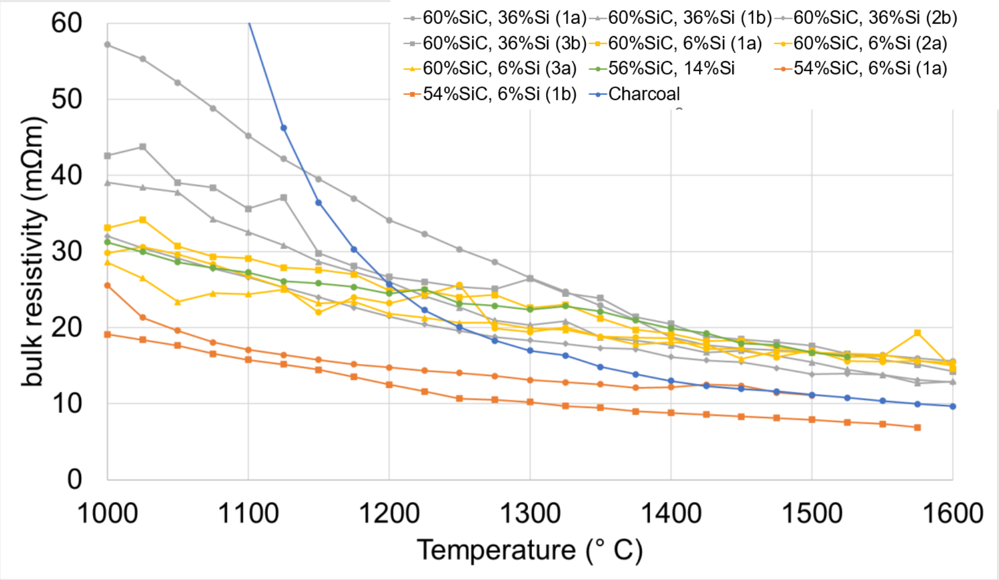

Figure 77. Enlarged part of Figure 18 showing resistivity with increasing temperature from 1000-1600 °C for the partially transformed SiC from charcoal, including charcoal A. 60 %SiC, 36 %Si is shown in gray, 60 %SiC, 6 %Si is shown in gold, 5 6%SiC, 14 %Si is shown in green, 54 %SiC, 6 %Si is shown in orange, and charcoal is shown in blue.

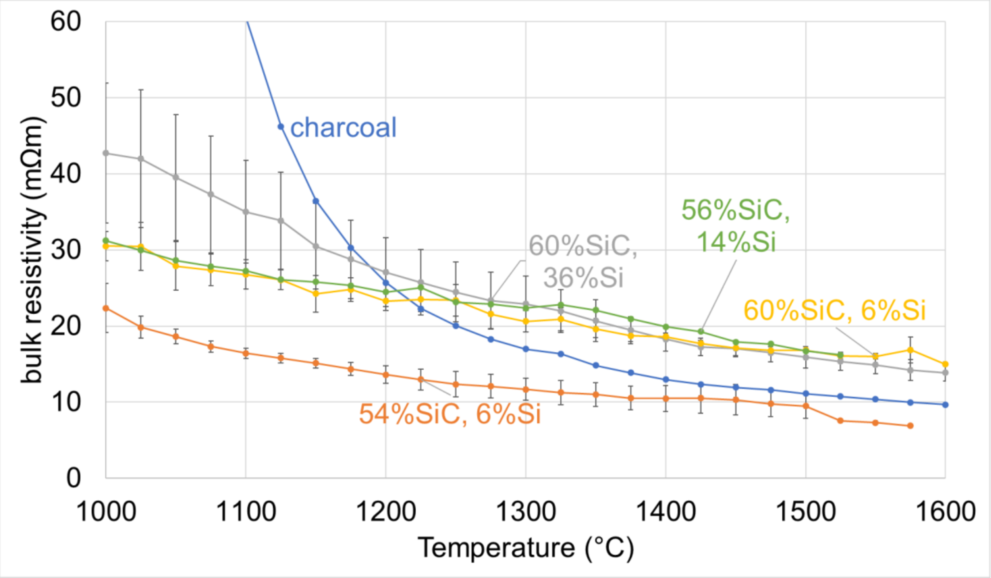

Figure 78. Average resistivity with increasing temperature from 1000-160 0°C for the partially transformed SiC from charcoal, including charcoal A. 60 %SiC, 36 %Si is shown in gray, 60 %SiC, 6 %Si is shown in gold, 56 %SiC, 14 %Si is shown in green, 54 %SiC, 6 %Si is shown in orange, and charcoal is shown in blue.

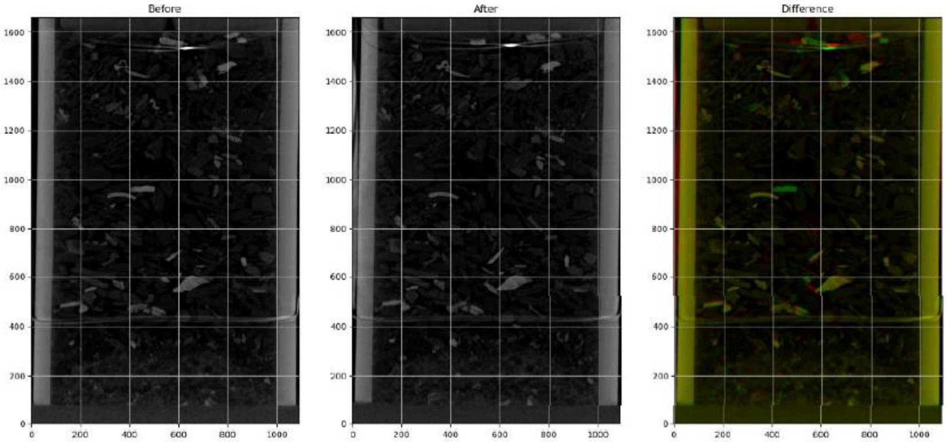

Figure 79. CT scans in YZ axis before (left) and after (middle) measuring resistivity of 60 %SiC 6 %Si from charcoal, and the calculated difference between the two (right).Green is before, red is after, yellow is overlapping.

4.2.3 Resistivity of charge mixes

Figure 80 shows the resistivity at 1400 °C for all charge mixes as a function of the volume of char (%). All results from char alone are also shown. Even with high variations among some of the mixes (char+quartz+silica-iron for example) there is a clear trend that increasing the volume of char in the bed decreases the resistivity at 1400 °C. The lowest resistivity at this temperature is in the char+quartz mixture with a 1:0.5 ratio, which is in the same area as the char itself. The highest is the mixture containing all raw materials with the lowest amount of char.

The samples that contained silica-iron ore formed a slag in the crucible upon heating, which is visible in the CT scans shown in Figure 81. Samples of the slag were taken and a WDS analysis showed the compositions, which are shown in Table 13. The slag had a high SiO_2 content of around 70 %, 10 % Al_2O_3 and 5-10 % FeO.

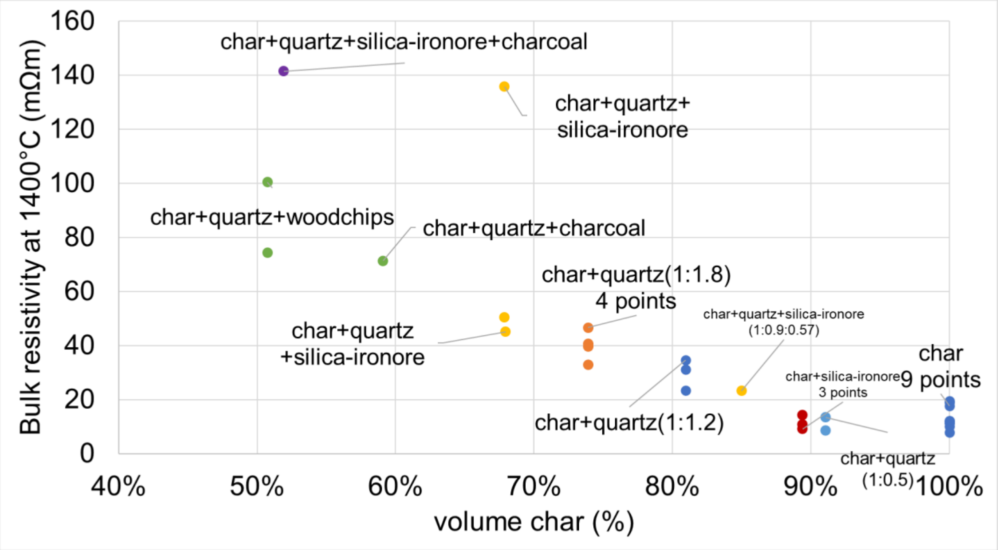

Figure 80. Resistivity at 1400 °C for all charge mixes as a function of the volume of char (% of total volume). Data points are labeled with their mixtures.

Table 13. Point analysis for the slag samples (average of 6 points)

		SiO_2	FeO	Al_2O_3	MgO	K_2O	CaO	Na_2O	SO_3
Slag sample 1	Average of 6 points (%)	69.90± 1.63	5.79± 1.17	11.21± 0.96	4.09± 0.36	2.09± 0.22	6.43± 0.46	0.8± 0.04	0.03± 0.01
Slag sample 2	Average of 6 points (%)	69.94± 3.29	11.16± 2.28	10.49± 2.18	3.23± 0.74	3.13± 0.34	1.66± 0.42	0.84± 0.12	0.18± 0.11

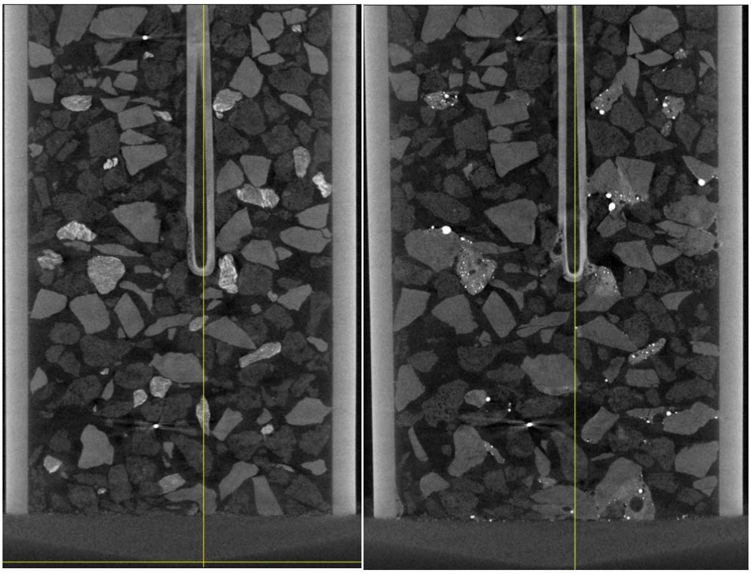

Figure 81. CT scans in YZ axis before (left) and after (right) measuring resistivity of char+quartz+silica-iron ore

4.2.4 Change of resistivity with multiple measurements

Multiple resistivity measurements were taken of most of the materials. This was done to see the variation in the measurement and the variation if the same particle were loaded into the setup differently. In some cases, the setup was untouched between the trials. This means that the particles were in the same packing and ordering configuration as they were in the previous measurement. However, in some cases the material was removed, sieved for fines, and then placed back into the setup for another measurement. This means the material was the same, but the ordering of the particles will be different since the sample was reloaded in a different configuration. This is differentiated using numbers and letters. The number indicates the experiment number *in that specific configuration*, and the configuration is specified by the letter. For example, the first time a material is measured it is designated as “1a”. If the material is measured again *without* repacking, it will be 2a. If the material is repacked, it becomes “1b”.

Since 69 %SiC from coal and 60 %SiC 36 %Si from charcoal have the most measurements, these will be the examples to show the effect of different packing on the resistivity results. Others will be shown in Appendix B. All 5 experiments with the 69 %SiC from charcoal are shown in Figure 82. In general, the first two experiments (1a and 2a) were lower than the subsequent experiments, with 1b, 2b, and 1c being slightly higher. However, with the materials from charcoal the trend is the opposite. In Figure 83 the results from the 60 %SiC 36 %Si from charcoal are shown, where the initial experiment has the higher resistivity. Therefore, the effect of the packing is seemingly random. Similarly, there is no clear correlation between experiments with the same packing. For example, with runs 1b, 2b, and 3b of 60 %SiC 36 %Si from charcoal, the results are mixed with 3b being the highest and 2b being the lowest. Thus, while it can be said that the ordering and packing of the particles will affect the resistivity, as is seen in the variations shown here, there is no clear pattern upon repacking or remeasuring the material that can be detected by this method.

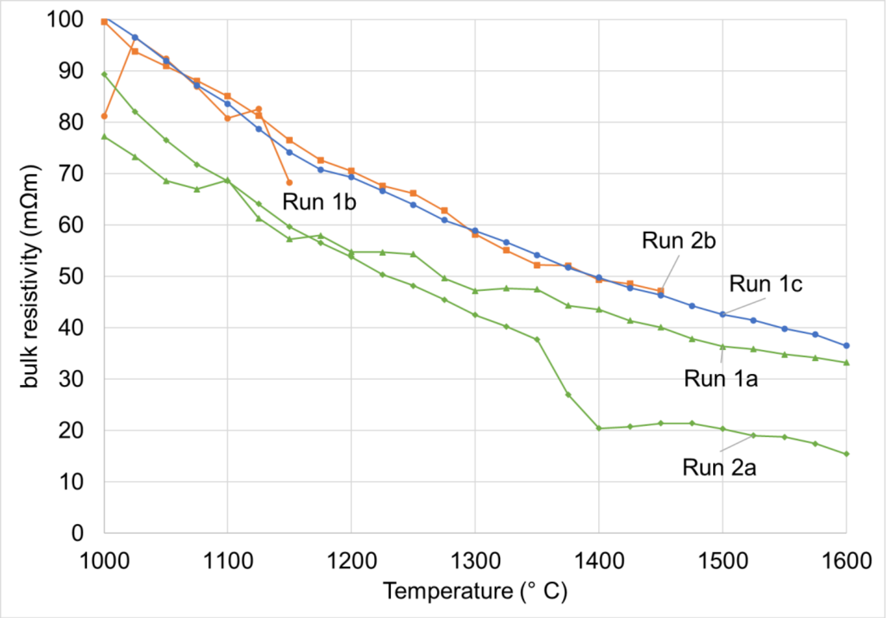

Figure 82. Resistivity with increasing temperature of all experiments with 69 %SiC from coal. Runs are labelled and colors show different packing.

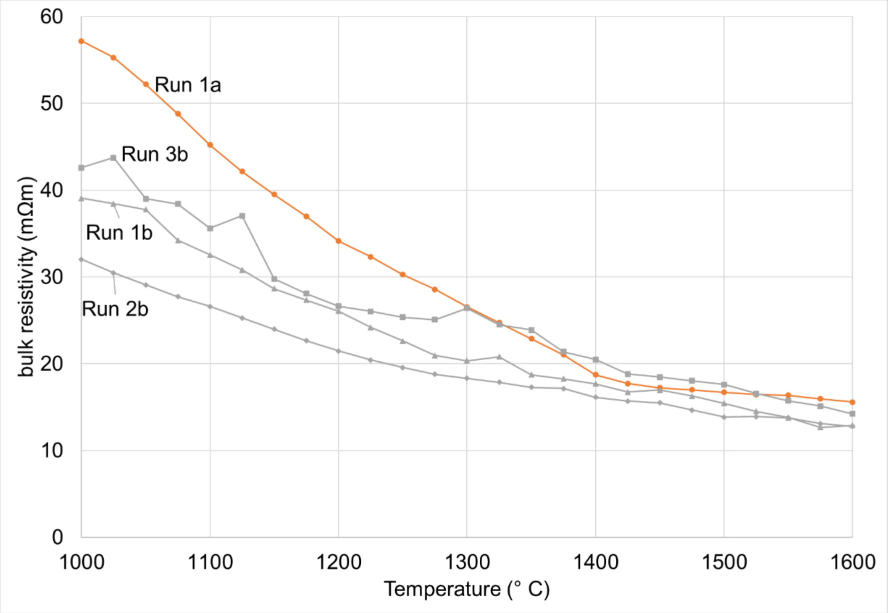

Figure 83. Resistivity with increasing temperature of all experiments with 60 %SiC 36 %Si from charcoal. Runs are labelled, and colors show different packing.

4.2.5 Bulk density before and after compaction

The bulk density before compaction (same as Figure 56 in Chapter 3) is shown in Figure 84 with the bulk density as measured after the bed was compacted for one of the resistivity measurements. The results show that the bulk density increases slightly for all materials after compaction, but the overall trend of which samples have the highest or lowest densities does not change. This shows that the compaction is effective at increasing the bulk density evenly across all the material, and any variations due to the strength of the material are likely small.

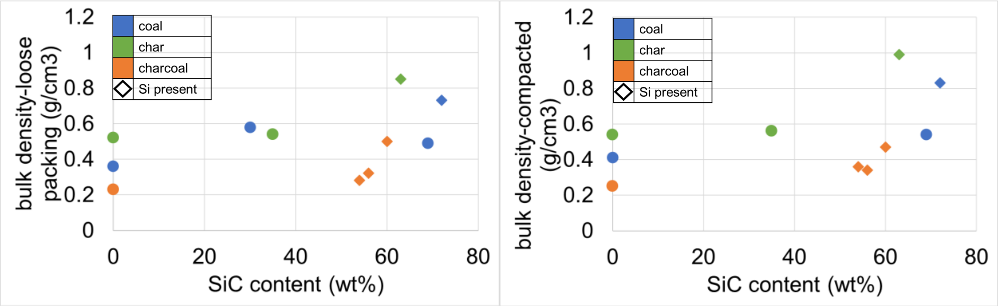

Figure 84. Bulk density versus SiC content for the partially transformed materials before (left) and after (right) compaction. Coal samples are blue, charcoal is orange, and char is green. Diamond markers indicate the presence of silicon. 30% SiC from coal is not shown on the right graph because it was not measured.

5 DISCUSSIONS

This chapter builds on the results presented in Chapters 3 and 4 through summarizing and discussing the knowledge and how it relates to what has been previously investigated. The chapter is split into three main parts. The first discusses the transformation of the carbon to SiC. The second discusses the effect of the transformation to SiC on the resistivity and how this relates to other materials in the Si furnace. The final part discusses the resistivity of the charge mix.

5.1 TRANSFORMATION OF CARBON TO SIC

This section discusses the mechanisms for the transformation of carbon to SiC and the formation of elemental Si, followed by the changes in strength.

5.1.1 Mechanism for transformation

There are two primary mechanisms for the transformation of carbon materials to β-SiC. The first is SiC crystals forming on the surface of the pore walls. The second is the pore walls themselves being transformed from carbon to SiC. The surface crystals can vary in size and shape but were primarily either surface crystals or whiskers, as has also been reported by Jayakumari [41]. Both were seen in the partially transformed SiC. The carbon materials used in this work were heat treated coal, char, and charcoal. All three carbon materials showed both surface crystal and whisker formation, however coal and char seem to have the higher amount of whiskers compared to charcoal. Two SEM pictures each of the SiC material from coal, char, and charcoal showing both whisker and large crystals are shown in Figures 85-87.

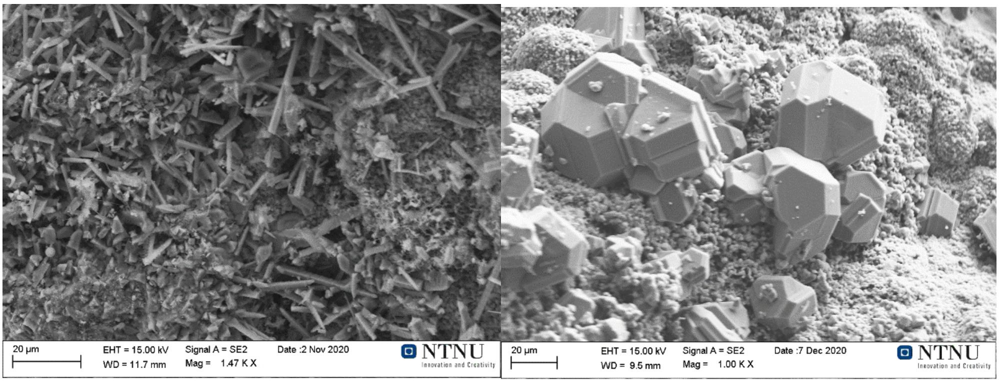

Figure 85. SEM images of SiC whiskers (left) and SiC crystals (right) from SiC materials made from coal

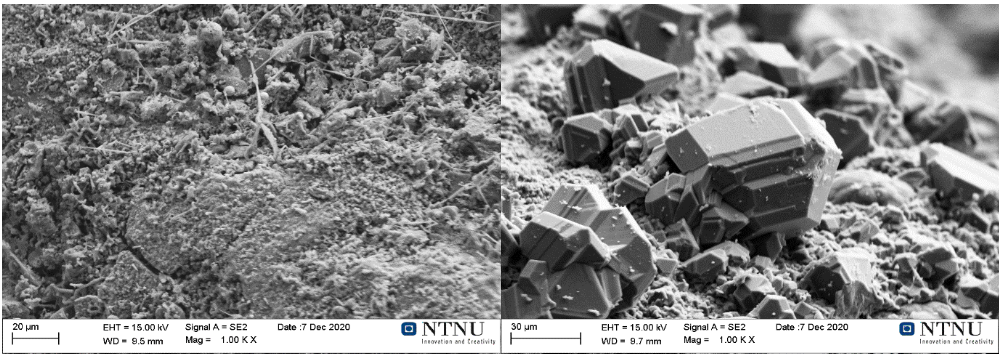

Figure 86. SEM images of SiC whiskers (left) and SiC crystals (right) from SiC materials made from char

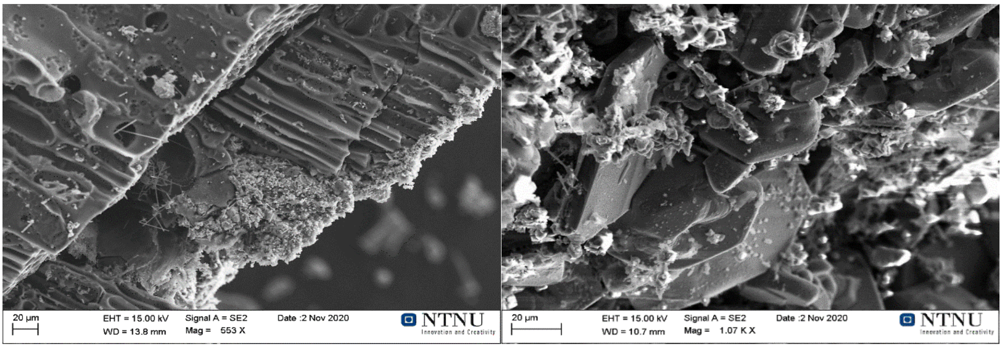

Figure 87. SEM images of SiC whiskers (left, same as Figure 50 in Chapter 3) and SiC crystals (right) from SiC materials made from charcoal

The transformation of carbon pore walls to SiC is clearly seen in the 72 %SiC, 7 %Si sample, shown in Figure 88. The proposed pores are drawn in red. The area around the pores shows SiC formation, with the pores remaining intact. This is evidence of the second mechanism wherein the pore walls are transformed to SiC. This is likely via the gas-solid reaction ($SiO+2C=SiC+CO$). A schematic of the mechanism is shown in Figure 89, with the following steps:

1. It begins with a carbon particle with spherical shape and irregular edges, with approximately 50 % porosity.
2. SiC layers begin to form around the outer pores and the outer edges of the particle in a shrinking core model.
3. The SiC layer becomes thicker. Based on the placement of the pores, some areas will overlap and have thicker layers of SiC. The particle behaves like the grain model, as the SiC is distributed across the particle surface.
4. As the SiC layer becomes thicker, areas with sufficient SiC and SiO pressure will form elemental silicon, even if there are some areas of carbon remaining on the particle.
5. The remaining carbon disappears as the entire particle is converted to SiC. Elemental silicon forms in the pores.
6. Silicon, which will be liquid at these temperatures and thus is not really a particle as such, will form large drops which are mixed with SiC.

All three carbon materials showed this behavior. Overall, the mechanism appears to follow the grain model, but due to diffusion through the pores there will be a nonreactive carbon “core” early in the process. This agrees with Myrhaug’s [28] conclusion that the shrinking core model gives a good mathematical description for the transformation of the carbon, due to factors such as pore distribution and diffusion.

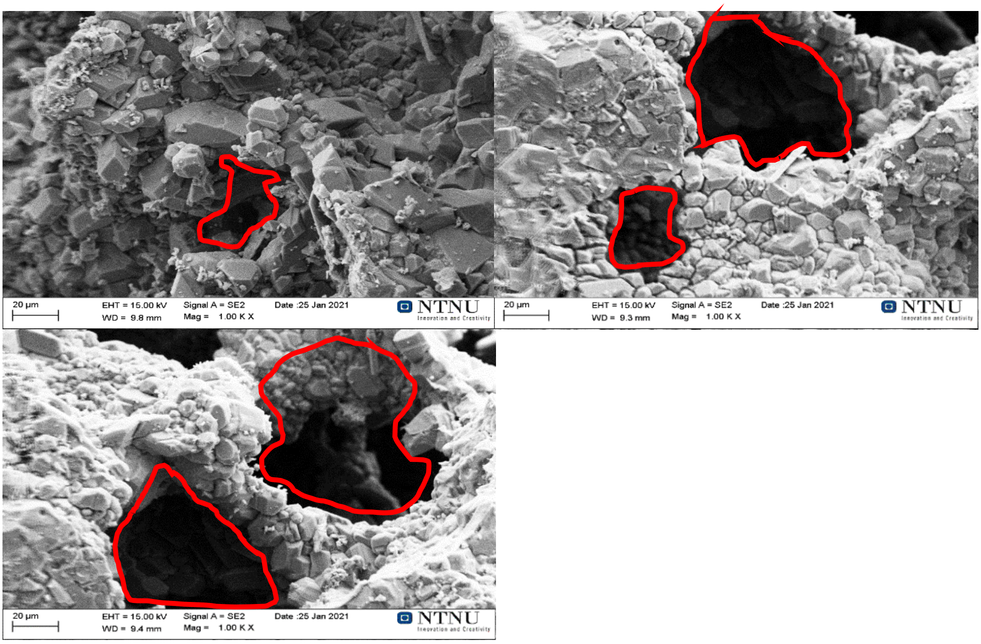

Figure 88. Three SEM images from the 72%SiC 7%Si material from coal. Crystals form around the pores, which are drawn in red.

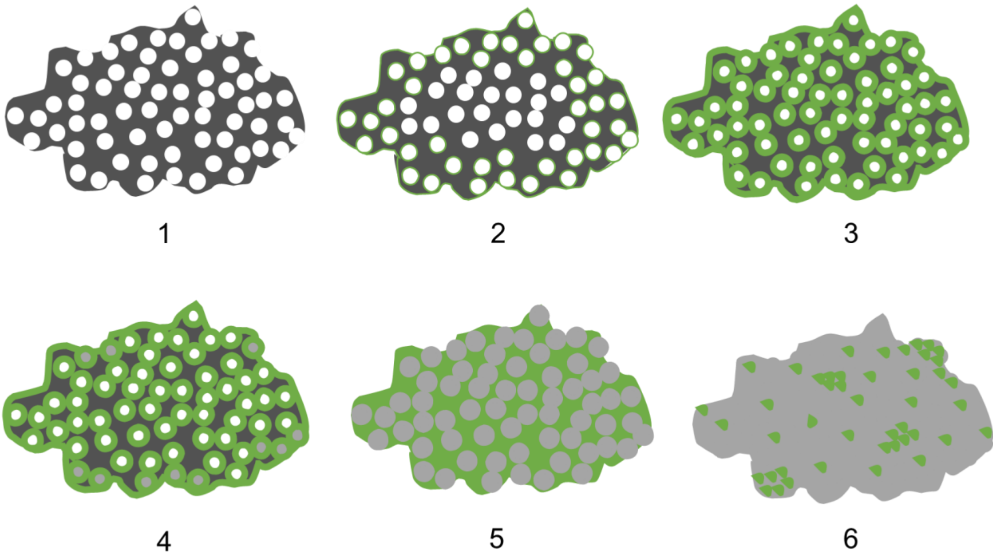

Figure 89. Drawing of the mechanism for the transformation of carbon to SiC using a spherical carbon particle with approximately 50 % porosity. Black is carbon, green in SiC, and gray is Si.

The overall transformation of a carbon particle to SiC will depend on the physical properties of the carbon material. The high porosity of charcoal, for example, allows SiO to diffuse easily throughout the particle. The thin cells walls also allow for more complete transformation. In contrast materials such as coal or char tend to have uneven pore distribution. Therefore, there will be areas on the same particle that will receive the SiO gas differently. This extends to the transformation in a bed of particles. Based on the physical properties and packing of the particles, as well as the direction of gas flow, the diffusion of SiO gas through the individual particle may be different. This will explain why the particles in the same layer in the crucible are not equally transformed to SiC and Si.

In Figure 90, a schematic of gas flow through a bed of coal and charcoal is shown. These particles are made with approximately 50 % porosity for the coal and 60 % porosity for the charcoal. The gas will reach the surface and areas around the pores and begin to form SiC. If the particles were not in a stationary packed bed, there would likely be more equal gas flow around the particle and thus even conversion that follows the mechanism shown in Figure 5. However, due to the packing, the gas does not have equal access to the entire particle. The result looks more like an uneven grain model, where individual grains of the particles, in this case in the area closest to the gas, will react as their own shrinking cores on the particle. This creates areas of high conversion to SiC and possibly the formation of silicon, with other areas of the particle remaining carbon. Furthermore, due to the packing there may be entire particles in the bed that the SiO gas takes longer to reach, and thus see little to no conversion to SiC, even when near a particle that is transformed. An example of this is shown in Figure 91, where CT scans of particles from the same layer in the crucible are shown. Although it is not clearly proven that the light=SiC and dark=carbon, this is still likely the case. The 35 %SiC from char shows maybe 2 particle that are highly converted, the rest appear mostly unreacted carbon or just beginning to form SiC on the outside of the particle.

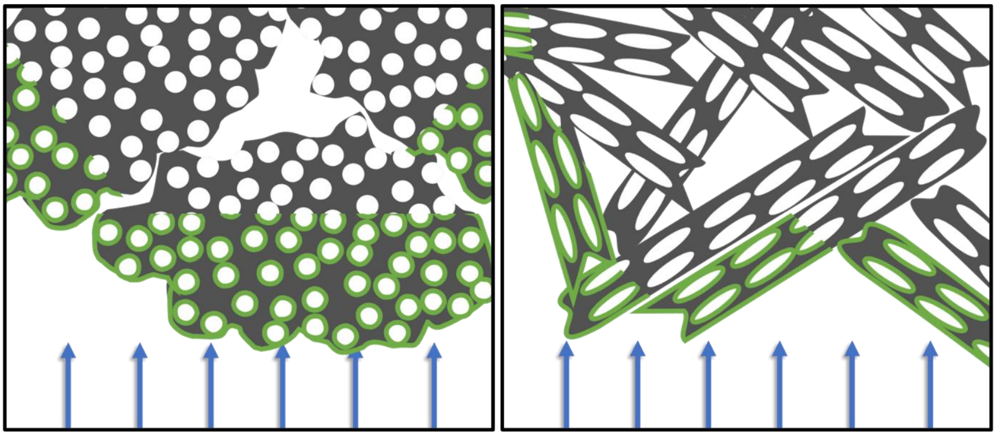

Figure 90. Drawing of an example of the transformation of SiC in a bed of coal (left) and charcoal (right). Black is carbon and green is SiC. Blue arrows represent SiO gas flow.

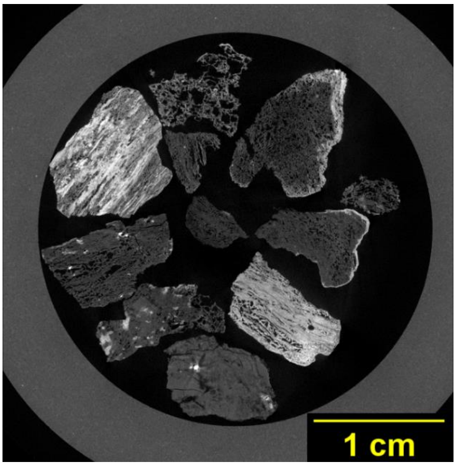

Figure 91. CT scan of 35%SiC from char that was taken from the middle layer of the crucible only. This is the same image seen in Figure 24 in Chapter 3. It is believed that the dark color corresponds to carbon and the light gray to SiC.

Silicon may form at temperatures lower than the 1800 °C that is thermodynamically predicted depending on the SiO pressure. It has also been shown that the quantity of silicon produced is based on the carbon source [41]. There does, however, seem to be a minimum required amount of SiC needed before silicon can form. Figure 92 shows the Si content of the samples compared to their SiC content. Samples in the figure are labeled if they came from a single layer in the crucible with the temperature shown based on the temperature at the bottom of the carbon bed. The samples with less than 40 %SiC have no silicon. Samples with at least 50 %SiC mostly contain silicon, with the exception of the 69 %SiC from coal. With the coal samples, silicon does not form until there is at least 70 %SiC. The charcoal, in general, also formed more silicon. Charcoal might meet this minimum threshold for SiC content more easily, due to its higher porosity, and more rectangular shape. The external factors are the same, such as temperature and SiO pressure. The denser, more spherical coal and char may require more SiC to form before silicon forms. This is why silicon forms even in the middle layers of the charcoal material, but not the char or coal. Furthermore, at the lower temperature of 1750 °C, charcoal still forms silicon in the middle layer. It has also been seen by Jayakumari [41] that the silicon is formed more easily in charcoal compared to coal and petcoke.

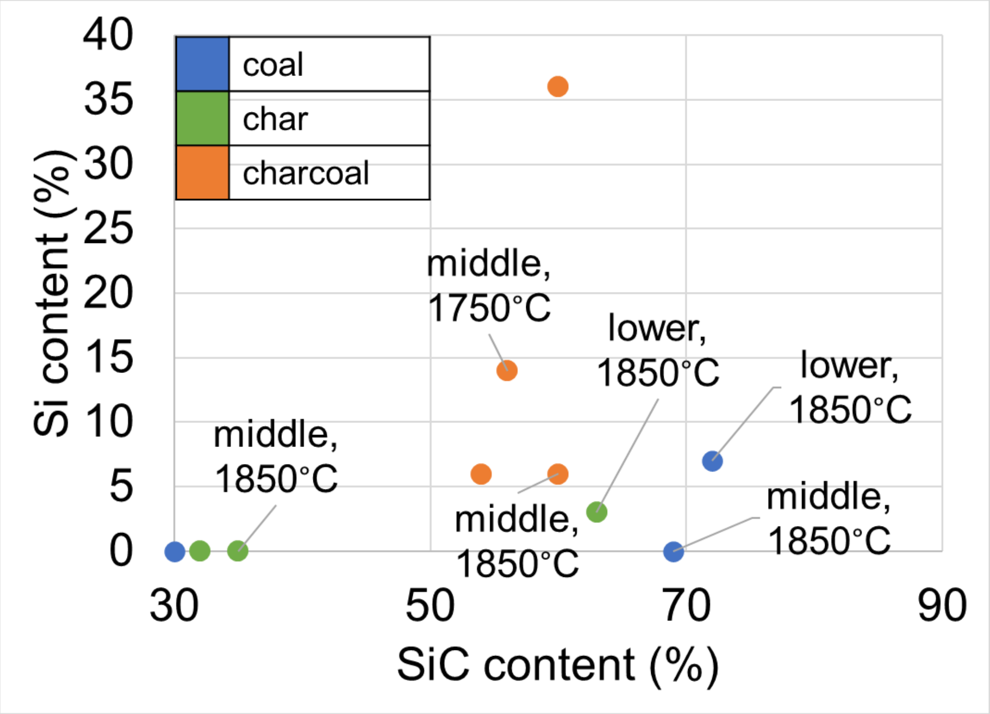

Figure 92. SiC content versus Si content in the partially transformed materials. Charcoal is orange, char is green, and coal is blue. Samples are labeled if they came from a single layer in the crucible and what the holding temperature was for that experiment.

5.1.2 Density and strength

Figure 93 shows a comparison in strength between the coal and char through both the average and the median. The coal appears to be stronger than the char since more force was required to crush the particles after the initial breakage began. This would be in contrast with Surup's [8] results with 4.75-9.5 mm particles. They found that coal had a weaker compressive strength than char. When considering the coal was heat treated and the char was not, based on Surup's results the difference in compressive strength becomes smaller, but they reported that the char would still be stronger. Figure 94 shows the transformed SiC from coal and char side by side with the same axes. More force was required to crush the material from char, regardless of SiC or Si content.

In Chapter 3, the results showed that the transformation to SiC weakened the material from coal, but the opposite was seen in the char. Based on literature values of polycrystalline and single crystal SiC films, the Young's modulus is 417 GPa and 388 GPa, respectively [77].

Comparatively, the Young's modulus for various coals is between 2.5-5 GPa [78]. This would imply that with high transformation to SiC, the material would be stronger, however, this appears to not be the case with regards to SiC materials made from coal, and also probably not for the char and charcoal. The reason for the difference could partly be in the porosity, since the mechanism has shown that the porosity will remain intact during the transformation until silicon forms in significant quantities.

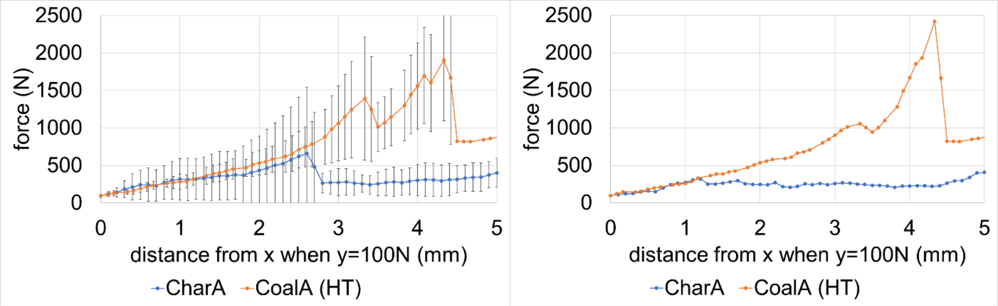

Figure 93. On the left, the average and standard deviation of the force needed to crush multiple particles of char (shown in blue) and coal (shown in orange) is shown. On the right, the median for the same particles is shown, with char is blue and coal in orange. X-values are corrected to filter out forces below 100 N.

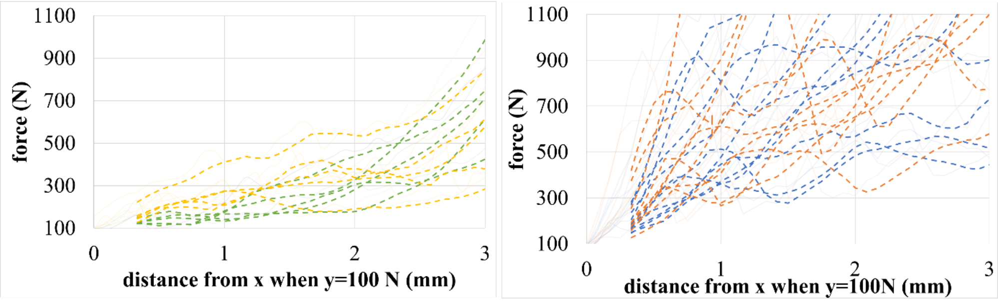

Figure 94. 5-period moving average for the force needed to crush particles of SiC from coal (left) and SiC from char(right). In general, the SiC from char is stronger than the SiC from coal. X-values are corrected to filter out forces below 100 N.

5.2 ELECTRICAL RESISTIVITY

This section discusses the electrical resistivity results, focusing on the high temperature zone of 1000-1600 °C. Results in this work are compared to literature and their difference are discussed. The carbon materials are discussed first, followed by the SiC materials, and then the charge mixes.

5.2.1 Bulk resistivity of carbon materials used in the Si/FeSi furnaces

The resistivity of the coal, chars, and charcoals measured in this work are compared to each other as well as literature values from [8] [7] [6] in Figures 95-97. Pedersen [7] and Surup [8] used the same carbon materials as this work, although Surup calls the coal "coal" not "coalA" and char as "semicoke". The axes in all three figures are the same for easy comparison. The charcoals generally have the highest resistivity, with a steep drop occurring around 1000 °C. The exceptions are the charcoal made from woodchips, and Eidem's charcoals, which were heat treated to 850 °C for 1 hour prior to measurement. The charcoals also have the largest range. At 1600 °C, they range from 10-20 mΩm, whereas the chars are around 10-15 mΩm and the coals are around 5-10 mΩm. Heat treated coals and chars have a slightly lower resistivity and are conductive at lower temperatures. In Figure 13, the coal used by Surup was not heat treated. This could explain its lower resistivity, as there was probably some caking, which would lower the resistivity by eliminating contact resistance between some of the coal particles.

In the industrial furnace, coal and char will be indistinguishable from one another, as was seen in the pilot scale experiment results. This likely remains true in terms of the resistivity, as the values of the coal almost entirely overlap the range of the chars. They also have similar densities. This is not surprising since heat treated coal was used in this work, which should resemble that of char (semicoke). In the furnace, both coal and chars will be heat treated before they are transformed and thus will look and behave similarly. In contrast, in the pilot scale experiment, the charcoal structure could be discerned from the other carbon materials.

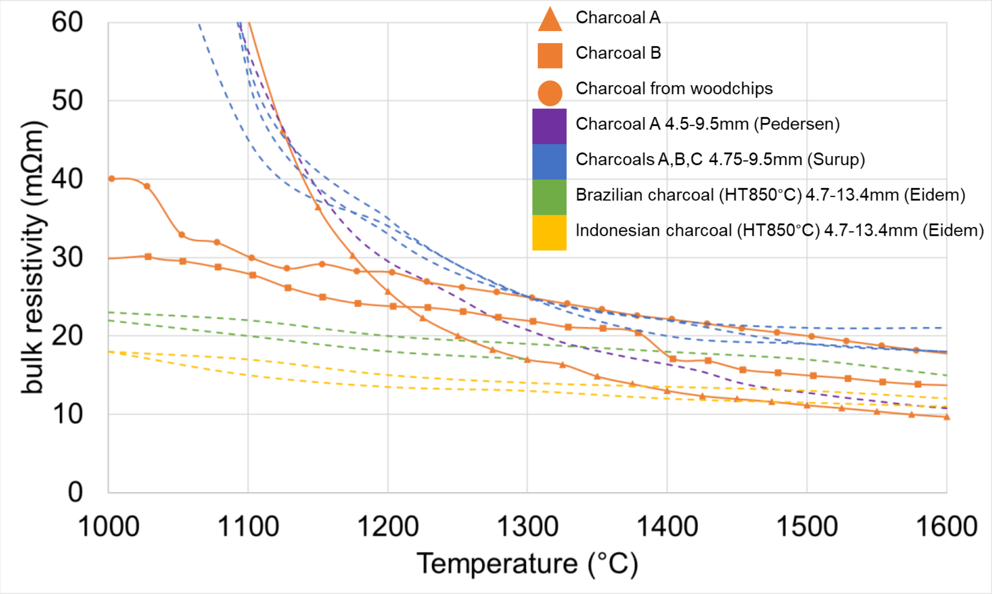

Figure 95. Bulk resistivity with increasing temperature for the charcoals (orange) compared to literature of similar materials and similar particle sizes.

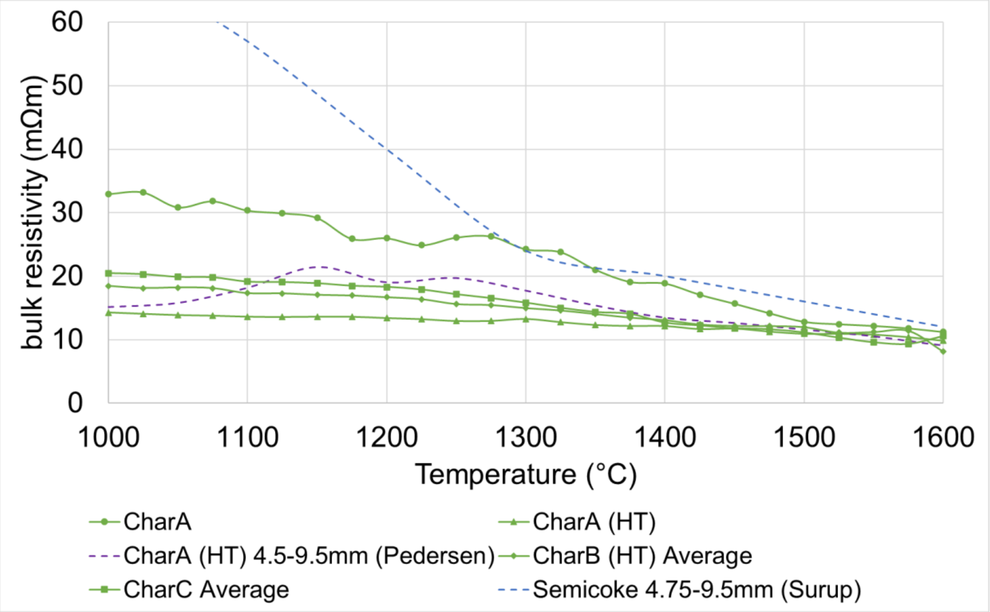

Figure 96. Bulk resistivity with increasing temperature for the chars (green) compared to literature of similar particle size.

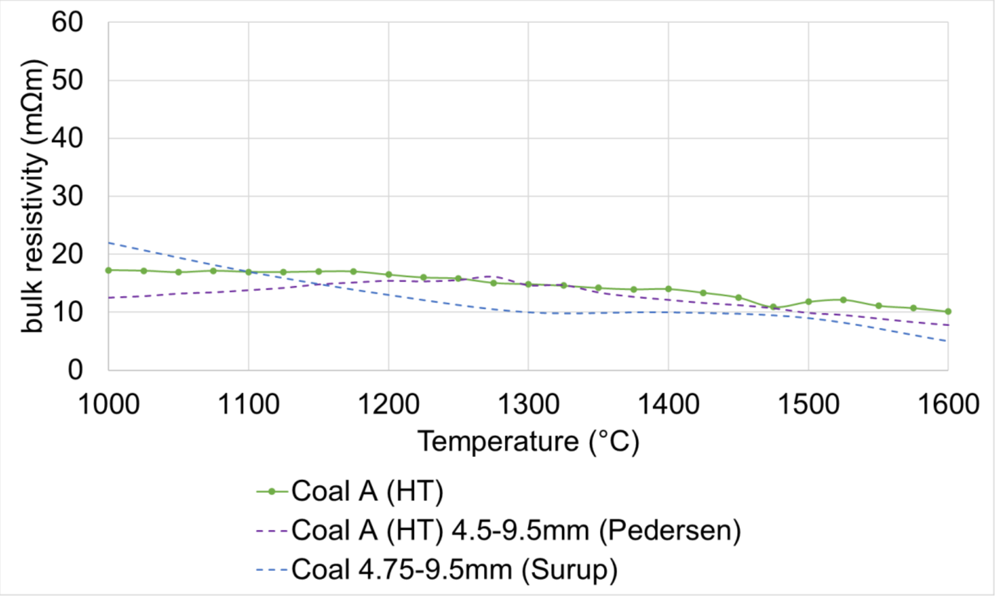

Figure 97. Bulk resistivity with increasing temperature for the coal (green) compared to literature of similar particle size.

Literature suggests that density is responsible for different resistivity in different carbon materials, as charcoal will be less dense, and the heat-treated coals and chars will have similar densities. Although coke was not measured in this work, it fits well with the trend as coke will have the largest density and tends to have a lower resistivity than all the other carbon materials [6]. However, as shown in Figure 98, the trend of "less dense, higher resistivity" holds true at temperatures as high as 1000 °C, but not for 1500 °C. At 1000 °C, charcoal has a much higher resistivity than the coal or char. At 1500 °C, the charcoal has the lowest density and the lowest resistivity. The difference at 1500 °C is also quite small, within 2 mΩm of each other. Homemade charcoal from woodchips is also shown by the square markers. At 1000 °C, the homemade charcoal has a lower resistivity than the industrial charcoal and is more similar to the char and coal. At 1500 °C, this trend reverses, as the industrial charcoal is similar in resistivity to the char and coal, whereas the homemade charcoal has a higher resistivity than all others.

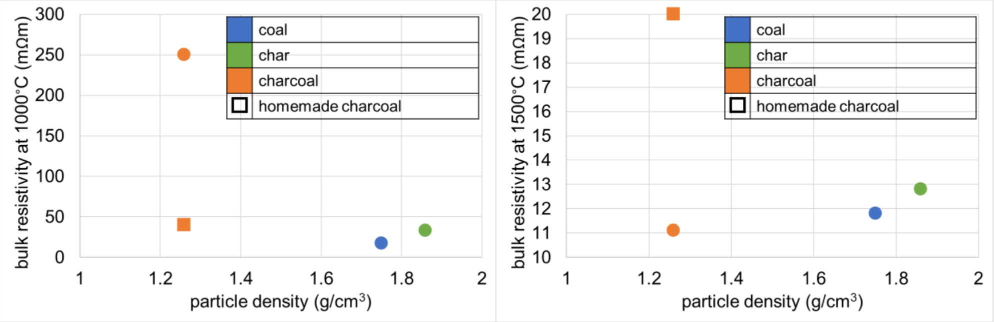

Figure 98. Bulk resistivity versus particle density for the charcoal, coal, and char at 1000 °C (left) and 1500 °C (right). Charcoal is orange, char is green, and coal is blue. Homemade charcoal is shown with a square marker, and it is assumed it has the same density as industrial charcoal.

Comparison between industrial charcoal and homemade charcoal from recovered woodchips (Figure 99) showed that the homemade charcoal was less sensitive to temperature and more conductive at lower temperatures but had a higher resistivity than industrial charcoal at high temperature (above 1200 °C). Standard temperature produced charcoals, which are typically made around 500 °C do not become conductive until around 900-1000 °C, where there is a steep drop in the resistivity. This is seen in other studies in both bulk [7] [10]and material [4] resistivity of charcoals.

Bharat [4], which tested the resistivity of charcoals at room temperature after heat treatment at increasing temperatures, reported that the higher heat treatment temperature of the charcoal would result in a lower resistivity at room temperature. However, at their highest heat treatment temperature of 1800 °C, both types of charcoal tested had similar resistivities. They believed this was leading to an asymptotic value. This agrees with the results shown in Figure 99 where all four charcoal measurements coming closer in range to one another as the maximum temperature of 1600 °C is reached.

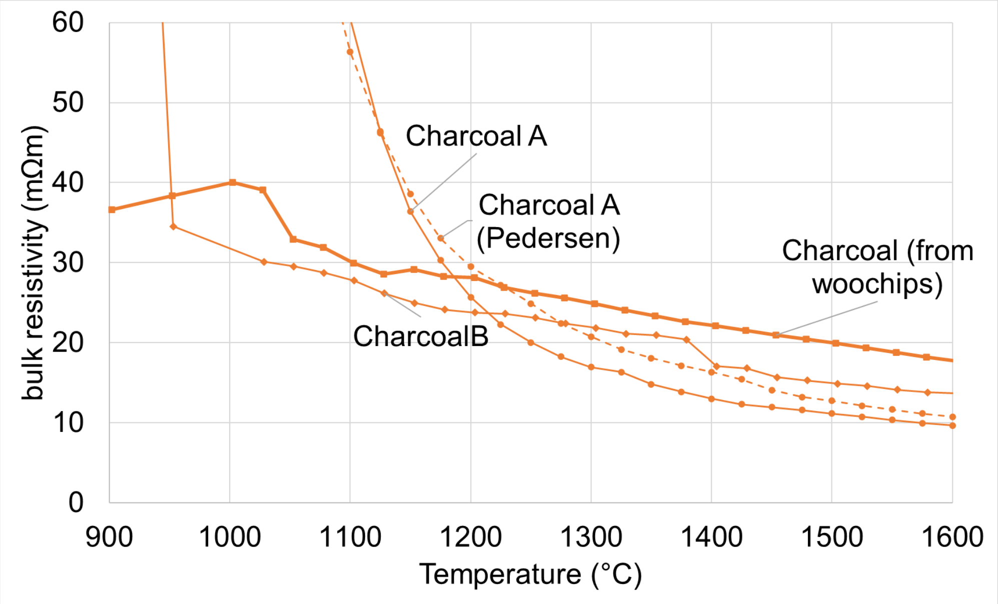

Figure 99. Bulk resistivity with increasing temperature for all charcoals measured, including the results from Pederson shown by the dotted line. The homemade charcoal line is in bold.

Furthermore, Surup showed that heat treatment of charcoals increased their mechanical strength [8]. In a bed of particles, this means that the bed would be more loosely packed as the particles cannot be "crushed" together as easily with the same amount of force. This would lower the contact area between the particles and thus increase the contact resistance. This increase in contact resistance would raise the overall resistivity. This means that the homemade charcoal would have the higher resistivity compared to the industrial charcoal, which has the lower heat treatment temperature. This agrees with the experimental results only after the industrial charcoal becomes conductive. However, this would be lessened at higher temperature since the overall contribution of contact resistance is also lessened at high temperature [6].

5.2.2 Effect of SiC transformation and Si formation on the resistivity

As the individual carbon materials are converted to SiC, the resistivity is increasing. Figures 100 and 101 show the resistivity at 1000 °C and 1500 °C for all the partially transformed SiC materials and the carbon materials as a function of the SiC content. The samples from coal are shown in blue, charcoal in orange, and char in green. Samples containing elemental Si are shown with diamond markers. There is an increase in resistivity when going from the original carbon material (0 %SiC) to partially transformed SiC and carbon material. The increase is clear for the coal and char materials, which have samples that do not contain silicon. At 1000 °C, the samples generally increase in resistivity with increasing SiC content, except for the charcoal. At 1000 °C, the resistivity of charcoal is still high compared to the other materials (around 250 mΩm). In contrast, the homemade charcoal from woodchips (square marker in figure) is much lower than the industrial charcoal at 1000 °C. At 1500 °C, the industrial charcoal becomes as conductive as the other carbon materials, and the homemade charcoal has the higher resistivity.

Additionally, for the char and coal materials, the presence of Si seems to slightly lower the resistivity. This is likely due to the silicon forming in the pores and increasing the density and decreasing the porosity. Furthermore, at 1000 °C, silicon will be solid in the samples and nonconductive. At 1500 °C, the silicon will be liquid and should be highly conductive [59]. This trend cannot be seen in the charcoal samples as all of them contain some Si. For the charcoal samples, the Si content ranges from 6-36 %, yet their resistivities are very close in range. This implies that the specific *quantity* of Si present (up to 36 %) is not so much what is changing the resistivity, but its *presence* and the corresponding lower porosity/higher density is what can have an effect.

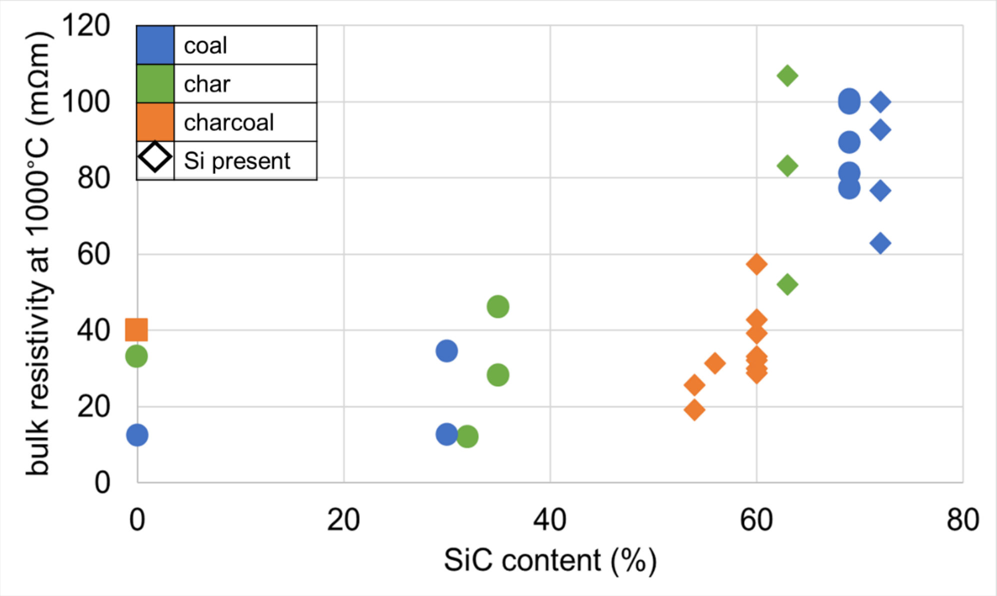

Figure 100. Resistivity at 1000 °C for all the SiC and carbon materials as a function of the SiC content. The coal is shown in blue, charcoal in orange, and char in green. Samples with Si are shown with diamond markers. Charcoal is not shown since the resistivity at this temperature is around 250 mΩm. Homemade charcoal is shown by the orange square marker.

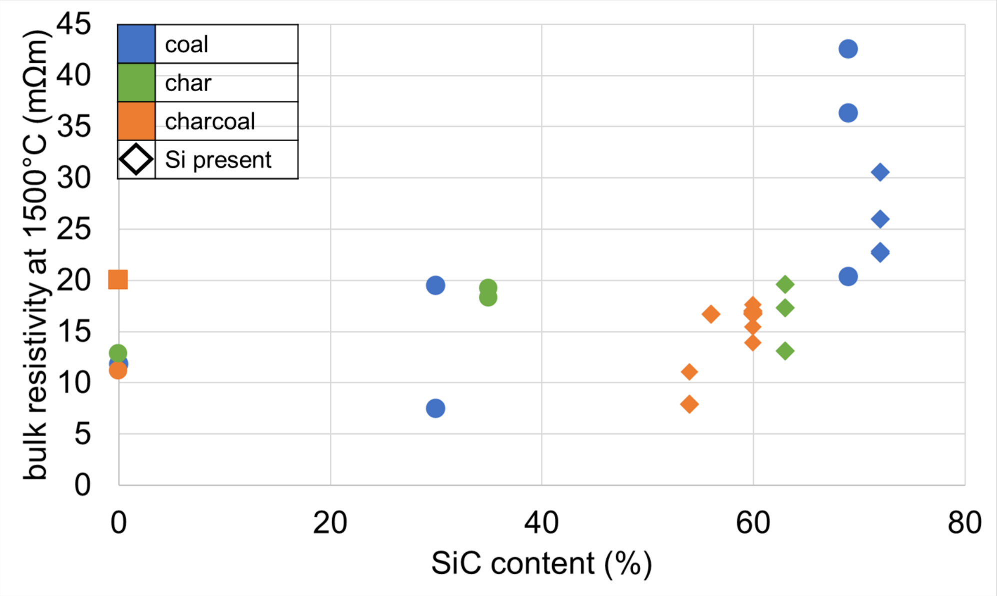

Figure 101. Resistivity at 1500 °C for all the SiC and carbon materials as a function of the SiC content. The coal is shown in blue, charcoal in orange, and char in green. Samples with Si are shown with diamond markers. Homemade charcoal is shown by the orange square marker.

No clear trend was seen between the bulk density and the resistivity for the partially transformed SiC materials. Figure 102 shows the bulk resistivity at 1500 °C versus the bulk density. The importance of the bulk density on the resistivity is likely lessened at higher temperatures due to the lessening effect of the contact resistance [6]. This was also seen in the carbon materials results, where the charcoal, which had the lowest density, had the lowest resistivity at 1500 °C.

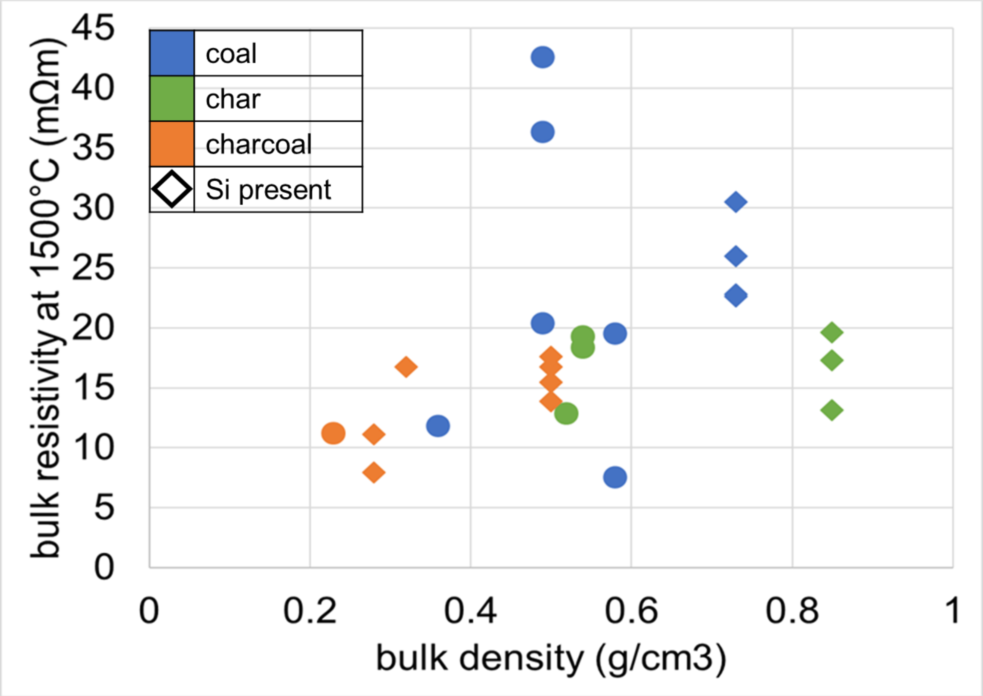

Figure 102. Bulk resistivity at 1500 °C versus the bulk density of both carbon materials and the partially transformed SiC materials. Coal is blue, char is green, charcoal is orange, and diamond markers indicate the presence of silicon.

Comparing the SiC materials to carbon materials and SiC crust from literature shows that partially transformed SiC will be as conductive or less conductive than carbon at high temperature. Figure 103 shows the resistivity of various materials in the Si process with increasing temperature from 1000-1600 °C. Measurements were graphed every 100 °C. The totality of partially transformed SiC materials from this work are shown in blue. The carbon materials from this work are shown in orange. Industrial α-SiC crust samples from Krokstad [3] are shown in pink, bulk resistivity of various cokes from Eidem [6] are shown in green. Finally, silicon from Law et al and [58] Sasaki et al [59] is shown in purple, although in this temperature range, the resistivity is so low that it is not properly visible on the graph.

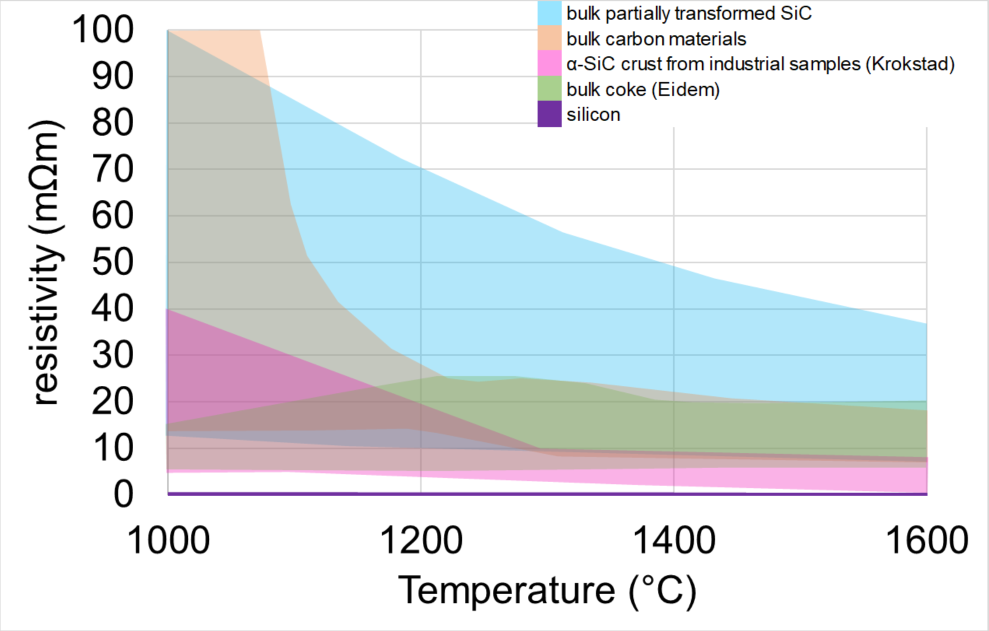

Figure 103. Resistivity with increasing temperature for partially transformed SiC materials, carbon materials excluding coke, industrial SiC crust samples, coke, and silicon.

The partially transformed SiC has both the largest range and the highest resistivity. However, it overlaps with most of the materials over the whole temperature range. The exception is above 1300 °C, where the industrial SiC crust becomes more conductive with no overlap of the other materials. However, since these samples were cylinders rather than a bed of particles, the contact resistance could be partly responsible for the difference. Eidem's bulk measurements of various cokes fit nicely within the range of carbon materials, with the lower range of coke being slightly lower. However, Eidem tests various size ranges from 6-10 mm to 15-20 mm. All samples in this work were 4-8 mm. Overall, at high temperatures, it can be said that as carbon is transformed to SiC and Si begins to form, the resistivity may be higher or in the same range as the carbon materials. Therefore, at temperatures above 1300 °C current will most likely pass through the SiC crust.

In addition to the lack of contact resistance in the SiC crust results, it is a different type of SiC. As mentioned, the SiC crust will be α-SiC and Si, in contrast to the partially transformed SiC which contains β-SiC, C, and Si measured in this work. SiC crust will have a higher density, and usually is filled with silicon in the pores. This will also lead to lower resistivity.

5.2.3 Resistivity in the charge mix

The amount of the main conductor, char in our case, seems to determine the bulk resistivity at high temperatures. This is seen in Figure 104, which shows the resistivity at 1400 °C for all charge mixes as a function of the volume (%) of char with a shaded region as a trendline. According to Surup [9], 40 % of the bed must contain conductive material for the entire bed to be conductive. Depending on the threshold for what is considered conductive, this applied to Figure 104 as well.

The transformed woodchips (charcoal) appears to have an insulating effect on the resistivity since the experiments with charcoal seem to agree with the char volume trend. This charcoal would mimic what was seen in the homemade charcoal measurements, where the resistivity is higher than for traditionally made charcoal and char and could therefore contribute to its more insulating effect at 1400 °C. The volume (%) of carbon in the bed versus the bulk resistivity at 1400 °C is shown in Figure 105. The linear trendline is similar to the volume of char alone, except in the case of the mixture of char+quartz+woodchips(charcoal), where the resistivity is higher than the trend predicts. This further implies that charcoal made from woodchips in the furnace has a higher resistivity than industrial charcoal. Therefore, in this case char is the main conductor. Overall, it appears that despite the competing factors and the individual conductivities of the materials in the mixtures, the amount of the main conductor is proportional to the bulk resistivity at high temperature.

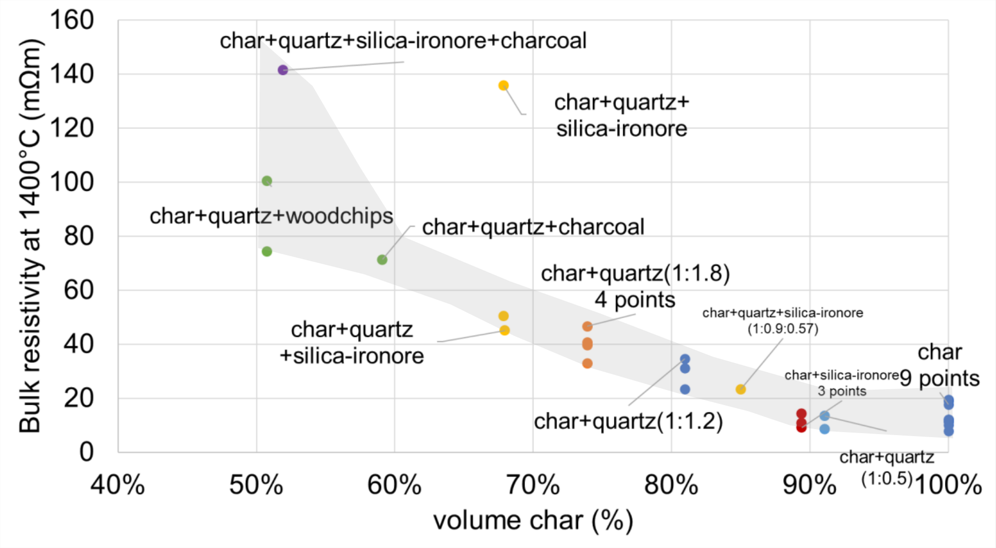

Figure 104. Resistivity at 1400 °C for all charge mixes as a function of the volume%char. Some points are labeled with their weight ratios.

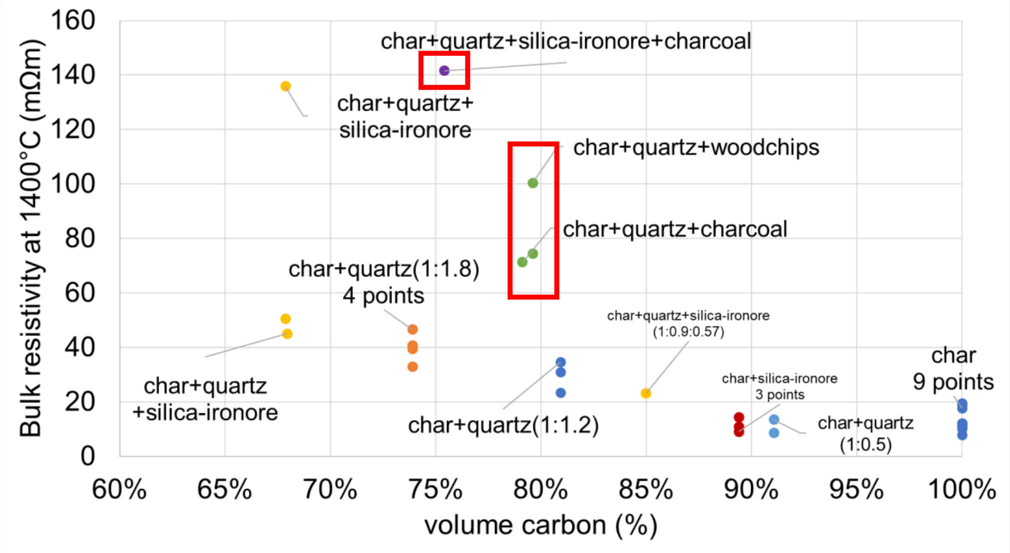

Figure 105. Resistivity at 1400 °C for all charge mixes as a function of the volume%carbon. Points are labeled with their weight ratios. The samples containing charcoal are outlined in red.

The possible current paths in a mixed bed are shown in a simplified 2D figure of a bed of mixed particles containing conductors (gray and black) and insulators (blue) in Figure 106. All particles are the same size and shape but are not perfect spheres. In theory, there are four basic scenarios that can determine the ability for current to pass through the bed. These scenarios are not exclusive and since they are 2D they do not account for the whole system.

In scenario one all the particles are conductive, and they have good contact so many possible current paths can travel through the bed of particles. In scenario two, insulators, represented by blue particles, have been introduced such that the bed is 60 % conductors, 40 % insulators. The current paths are somewhat restricted as they must circumvent the insulators to travel the path of least resistance. However, current can pass through the bed. In scenario three, there is a mixture of insulators and conductors where the bed is 40 % conductive, 60 % insulating. The current path is even more limited here and there is a localized "dead zone" on to the right where current cannot pass through that area. In scenario 4, the bed is only 30 % conducting and is 70 % insulating and there is no path for the current to travel.

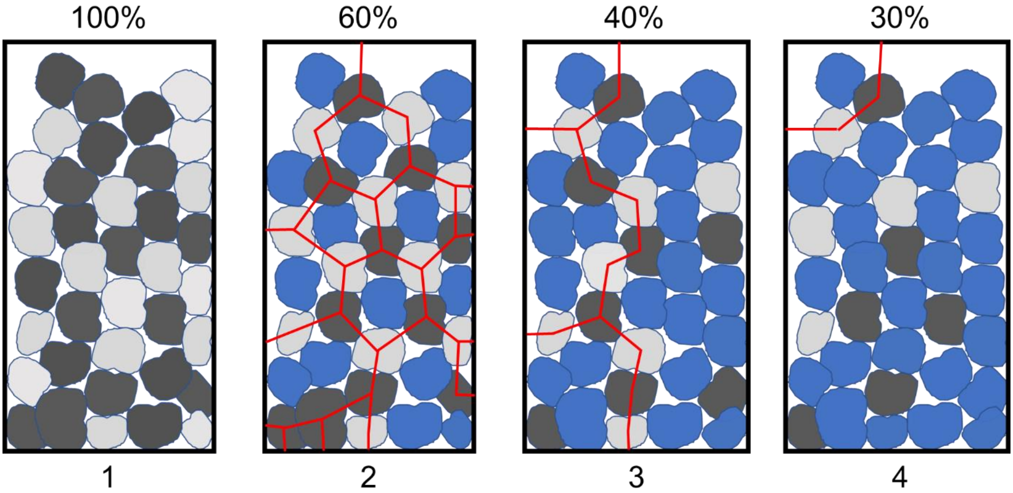

Figure 106. Simplified diagram of 4 scenarios of current running through a bed of conducting (gray and black) and insulating (blue) particles, beginning with 100 % conductors to 30 % conductors.

In an industrial furnace, these scenarios are more complex working in three dimensions and with different temperatures and gases reacting with the material. However, dead zones could still be possible in both the active and inactive zones in the furnace. In smaller scale experiments these dead zones are more significant as they can potentially change the current paths in a smaller measuring zone.

Slag may also be a conductive element. Based on the composition of the slag formed in the charge mixes, the conductivity would be quite low and compared to the other charge materials would be nonconductive [71] [70]. For some of the experiments, such as the char+silica-iron ore, it is possible that the slag is not in the measuring zone, or it is just not present in sufficient quantities to overcome the conductivity of the char. This is plausible since the ore only accounts for around 10 % of the volume in the char+silica-iron ore experiments. With this small volume, the experiments with the slag forming silica-iron ore and char are not significantly different from the char itself.

6 EXCAVATION OF 160 KW PILOT SCALE SI FURNACE

Excavations are a useful tool for studying the various zones and reactions in the Si process in comparison to the theory. Several excavations have been done on industrial and small-scale Si/FeSi furnaces. Each furnace excavation is unique because the zones in the furnace will depend on the history of its operations. However, there are commonalities among most of them regarding the formation of SiC, condensates, and Si production. This chapter details an excavation of a 160 kW pilot scale single electrode Si furnace. Excavations are not easily available. As the zones and materials are giving information about reactions and mechanisms in the industrial furnace, every new excavation may verify previous theories or give new information on the industrial process. The goal of this excavation is hence to verify existing theories from previous excavations or find gaps in existing knowledge.

6.1 MATERIALS AND METHODS

The pilot furnace was run using a single electrode with 1 phase current and target load of 160 kW. Operations lasted for approximately 80 hours of total continuous operation. The more detailed discussion of the operation is discussed in [79]. A schematic and physical picture of the pilot scale furnace is shown in Figures 107-108. The carbon materials were similar to that used in industrial operations, with the chemical analysis and composition of the raw materials summarized in Tables 14-16. Two different quartz sources were used, the main difference between them being different amounts of Al_2O_3 and CaO.

Figure 107. Furnace tapping during pilot scale furnace operations (Photo: Haley Hoover).

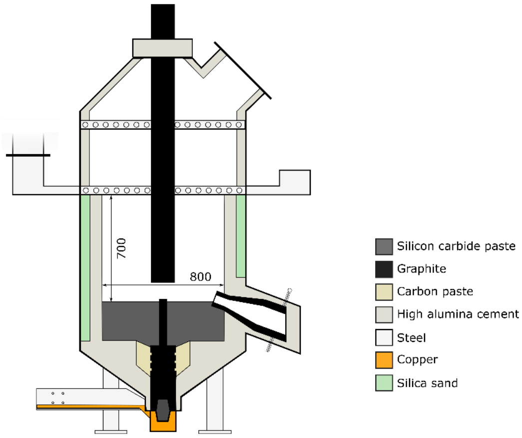

Figure 108. Schematic of pilot scale furnace from NTNU/SINTEF, used with permission from [79] Copyright © 2022 by The Minerals, Metals & Materials Society. Used with permission.

Table 14. Composition and amounts of carbon materials

Material	Fixed%C (dry)	Moisture%	% of Fixed%C total	Amount for 100% carbon coverage
Coal	57.67 %	13.92 %	40 %	4.03 kg
Coke	94.25 %	4.00 %	15 %	0.83 kg
Charcoal	85.20 %	4.66 %	30 %	1.85 kg
Woodchips	25 %	4.75 %	15 %	3.15 kg

Table 15. Composition of quartz 1and 2

	Quartz 1 Wt% (%)	Quartz 2 Wt% (%)
SiO_2	97.2	98.6
Fe_2O_3	0.87	0.31
Al_2O_3	0.81	0.69
CaO	0.60	0.06
K_2O	0.17	0.14
MgO	0.13	0.17

Table 16. Main impurities in carbon materials used in the pilot scale furnace

Element	Coal Amount (ppmw)	Charcoal Amount (ppmw)	Coke Amount (ppmw)
Si	6650	1260	15300
Al	2280	225	2420
Fe	2460	398	2240
Ca	695	11300	477
K	268	292	121
Mg	398	824	322
Na	710	114	448
P	20	515	28.8
S	3910	243	2090
Ti	100	8.02	89.6
Mn	18.3	480	22.8

The furnace was tapped discontinuously and shut down approximately halfway through the tapping cycle, including stoking and charging, and the electrode was left in position. Each tapping was estimated to last around 90 minutes including tapping, stoking, and charging which in practice led to approximately 60 minutes of uninterrupted operation. After the furnace was cooled, epoxy was added and left to cure for approximately 1 week. Vertical core drilling was done according to the Figure 109, where a total of nine cores were drilled, two in each compass direction and one through the electrode. As typically most of the production is occurring close to the electrode, the cores were focused close to the electrode. The inner diameter of the furnace was 80 cm with a height of around 70 cm. The diameter of the electrode was 15 cm.

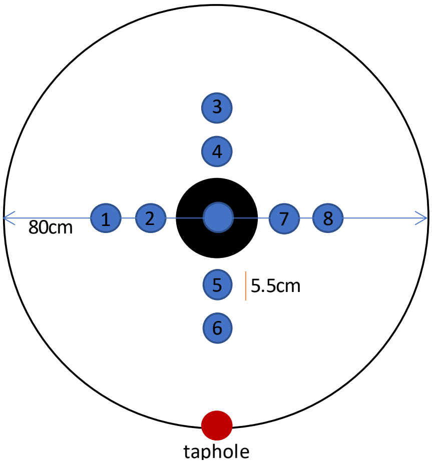

Figure 109. Diagram of core drilling samples taken from the pilot scale furnace where the circle represents the inner lining, core samples are numbered and colored, and the taphole is shown in red.

For cores 1 and 2, samples were taken from the cores approximately every 5 cm using a Labotom-5 cutting machine which was water-cooled and fitted with a diamond coated blade. The remaining cores has samples taken every 10 cm. The samples were recast in epoxy if needed, and polished. The diameter of the samples was 3-3.6 cm, compared to the 5.5 cm that were drilled. An electron probe micro-analyzer (EPMA) was used to identify different phases and specific compositions for mixed samples. Samples were cast in iodoform epoxy to give better contrast. EPMA works similarly to the SEM but is more precise in its quantitative analysis using wavelength dispersive spectroscopy (WDS) [74]. EPMA and WDS was performed using XA-8500F Field Emission Electron Probe. Characterization methods were explained in Chapter 3 and will not be repeated here in more detail.

6.2 RESULTS

The resulting cores were visually examined and characterized into 5 material zones based on physical appearance. The height of each material zone was used to create an estimated cross section in the two compass directions. These cross sections can be seen in Figure 110 and 111. These estimated zones include:

- Charge with condensate (dark blue)
- Top gas cavity (gray)
- Partly reacted charge materials (yellow)
- Silicon and slag (light blue)
- Lining (green)

In addition, there were some holes due to the drilling process, shown in orange.

The condensate and charge layer was around 10 cm high and relatively even throughout the investigated part. The glassy condensate acts as a glue which keeps the charge in place. There was a cavity directly below this layer, referred to as a top cavity.

The top cavity was uneven across the cores. Cores 1 and 2 had a cavity size of 10 and 15 cm, respectively. Across the electrode in the same axis, cores 7 and 8 saw cavities of 40 and 35 cm respectively. In the other direction, cores 3-6 are similar in their depth, but cores 3 and 4 saw little to no condensate/charge layers above the top cavity, whereas cores 5 and 6 saw similar results to the other cores. Cores 3 and 4 are the furthest from the taphole, and cores 5 and 6 are the closest.

Below the top cavity was partly reacted charge material. This layer is also relatively small, with some cores only having a couple of centimeters of partly reacted charge materials. The largest material layer is the liquid silicon with some slag and SiC. The layer is mostly consistent, with a moderate spike in core 2. No cavity was seen around the electrode tip in this work.

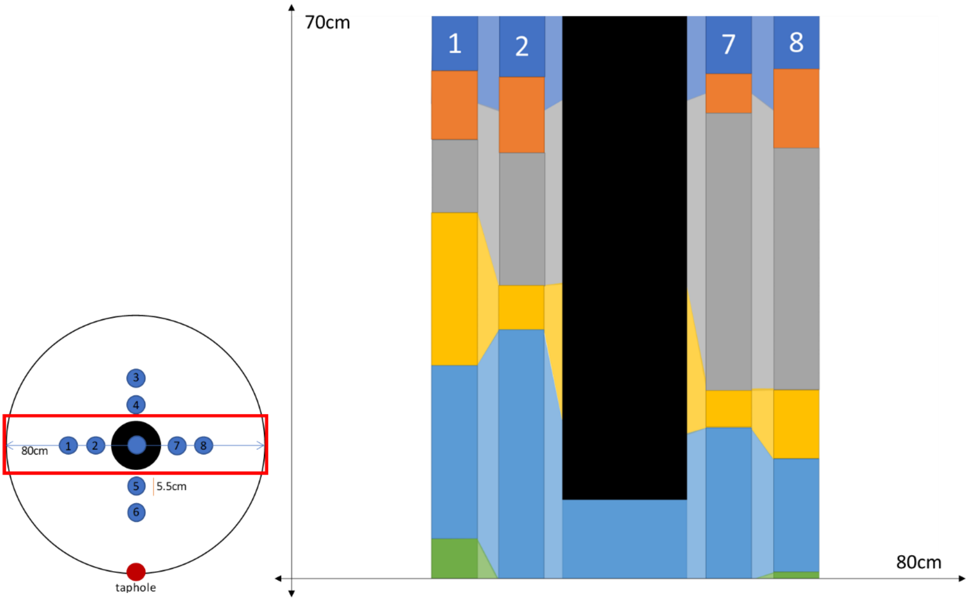

Figure 110. Diagram of various materials in the furnace based on cores 1, 2, 7, and 8. Opaque colors describe the cores and transparent shading is an extrapolation.

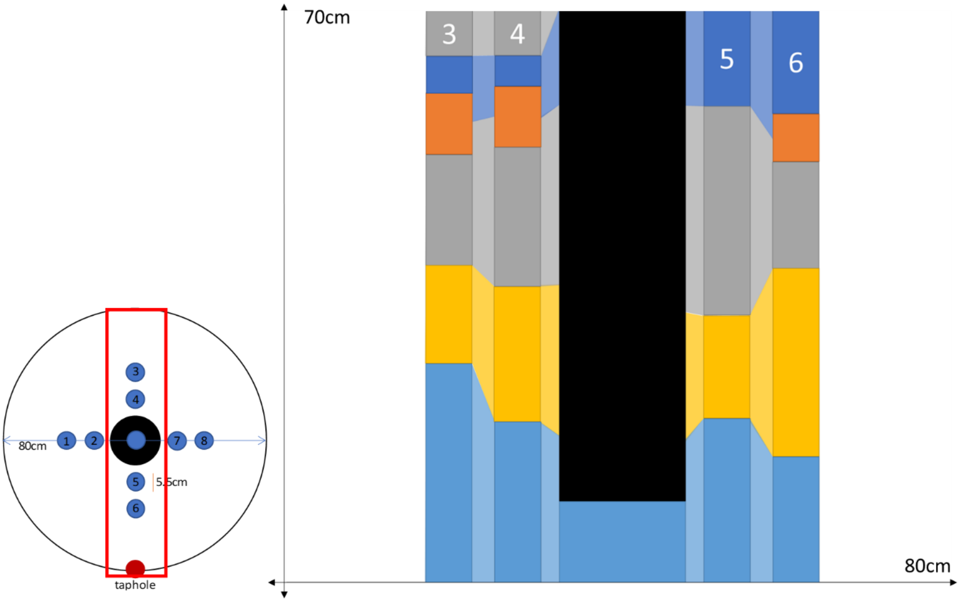

Figure 111. Diagram of various materials in the furnace based on cores 3, 4, 5, and 6. Opaque colors describe the cores and transparent shading is an extrapolation.

6.2.1 Charge with condensate

Due to the temperature gradient in the furnace, the top usually contains condensate and sometimes loose charge, depending on when the furnace is stopped in its stoking cycle. A top cavity was seen in this furnace, which was held in place by the glassy mixture of condensate and loose charge. All three samples taken in this region (Figures 112-114) have a depth of 5cm from the top of the furnace. The loose charge consists of quartz, seen in all three samples with a cracked surface, and carbon materials. The charcoal may be distinguished from the coal and coke from its structure, visible in sample 2.1 (Figure 113). However, the coal and coke cannot be distinguished individually so they are labelled as "coal/coke."

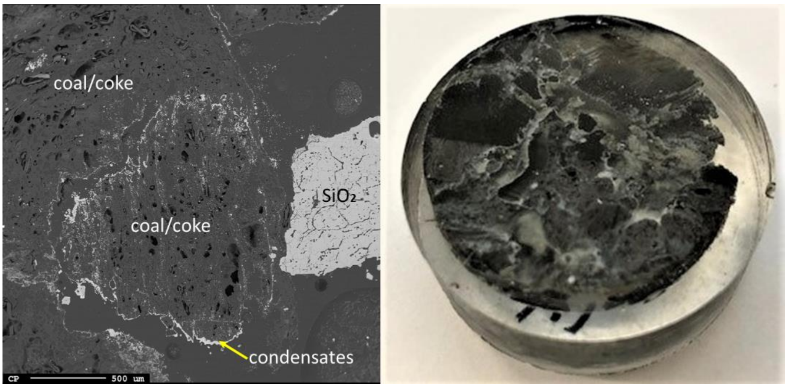

Figure 112. EPMA of sample 1.1 (left) and Image of sample 1.1 (right)

In samples 1.1 and 2.1 (Figure 112 and 113) the carbon particles are lined with condensate. A WDS analysis was done on six points of the condensate in sample 2.1, and the results are shown in Table 17 that the condensate contained K_2O (5.4±1%), Al_2O_3(18.3±3%), and Na_2O(1.8±1%). It is believed that the alumina comes from the ash in the coal/coke, while the potassium mainly comes from the gas phase, as potassium will be vaporized in the high temperature part of the furnace. Sample 2.1 also contains visible brown condensate. Both in the EPMA picture and in the picture one can visually see that the condensate layer being several mm thick. Sample 6.1 (Figure 114) is the only sample in this region to show SiC, as the carbon particles have been fully converted, although their original structure is still visible. Gas blows could have provided the temperature and SiO pressure needed at this level in the furnace for Equation 3 to begin to form SiC. Additionally, the condensate in this sample is mixed with SiC and a band of Si droplets. The droplet structure implies the reverse of Equation 2 rather than the silicon producing reaction (Equation 4) due to the low temperature this high in the furnace.

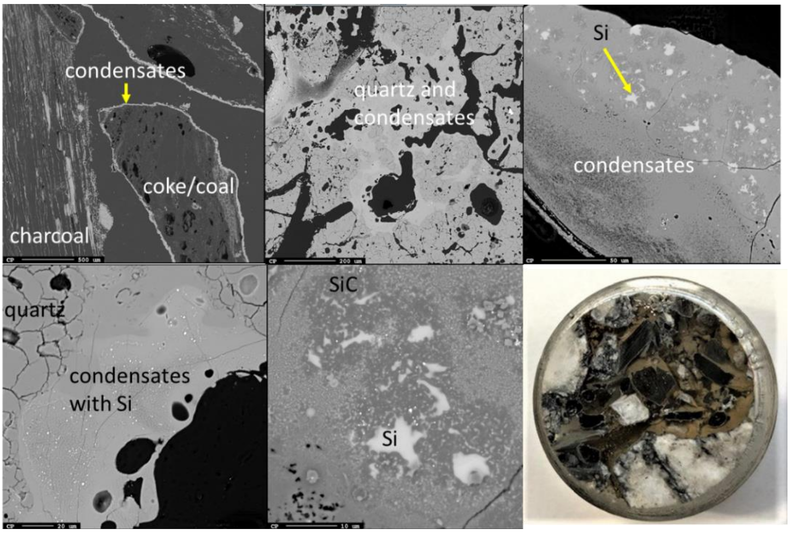

Figure 113. EPMA of five different areas of sample 2.1 and image of sample 2.1

Table 17. Mass percent results from the point analysis of the condensate in sample 2.1 (top right in Figure 113)

No.	SiO_2	Al_2O_3	K_2O	Na_2O	Total
Average	74.7	18.3	5.4	1.8	100.1
Standard Deviation	3.8	3.2	1.0	1.1	1.0

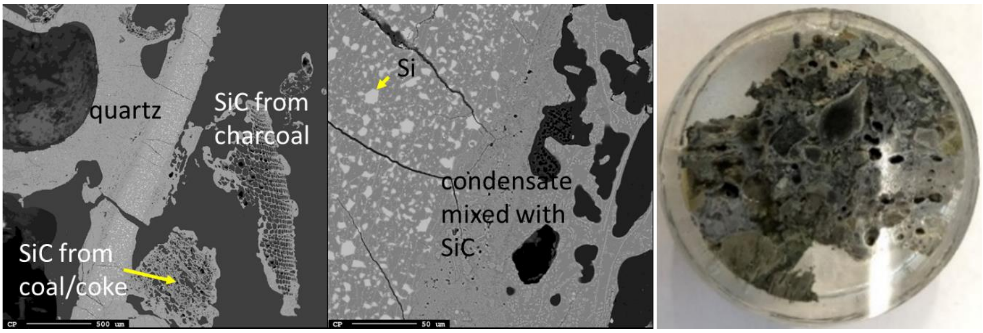

Figure 114. EPMA of two different areas of sample 6.1 and image of sample 6.1

6.2.2 Partly reacted charge materials

Just below the top cavity, the material has been exposed to higher temperatures and has begun to react or melt. However, during stoking and charging, unreacted materials may also fall into this zone. Seven samples were taken from this region just below the top cavity with a depth range of 15-40 cm (Figures 115-122). Partly reacted materials were found this low in the furnace.

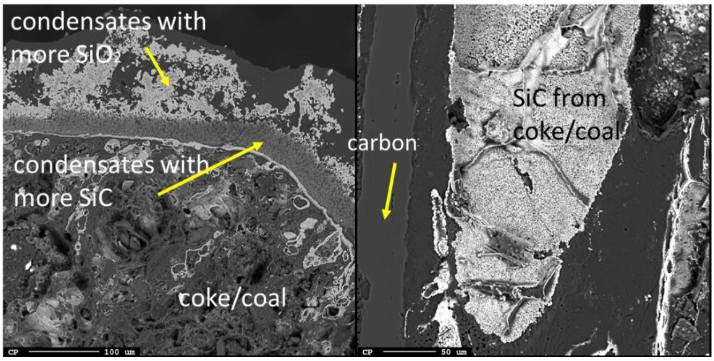

Figure 115. EPMA of two areas of sample 1.3

Areas of quartz were found in this region. Most of the areas where a carbon structure was visible had been converted to SiC. The only sample containing unreacted carbon was sample 1.3 (Figure 115). Samples 1.3 (Figure 115), 3.3 (Figure 119), and 4.3 (Figure 120) show SiC made from carbon with a green color. Condensate is also present in this region as shown in sample 2.3 (Figure 117). The nature of the condensate was difficult to determine as two chemically similar phases are seen. Elemental mapping was done on two areas of the condensate in sample 1.3 (Figure 115) to show that the condensate contains some areas which are richer in SiO_2 and some which are rich in SiC with SiO_2.

More substantial areas of Si are also seen in this region, such as with samples 2.5, 8.3 and 5.4. Sample 2.5 (Figure 118) shows an example where almost all SiC is transformed to Si according to Equation 4. Typically, one sees a thin rim of SiC according to the original C particle, while most of the interior is filled with Si. The Si is surrounded by either condensate (sample 2.5) or slag (samples 8.3 and 5.4). Small white drops of FeSi are also visible throughout. Three areas of the slag in sample 8.3 were used for a point analysis to determine its composition. The results are shown in Table 18, where the majority is silica (65.4±1%), alumina(26.5±1 %), and calcia(7.5±0.1 %), with 0.8±0.1 % K_2O and trace amount of the other oxides.

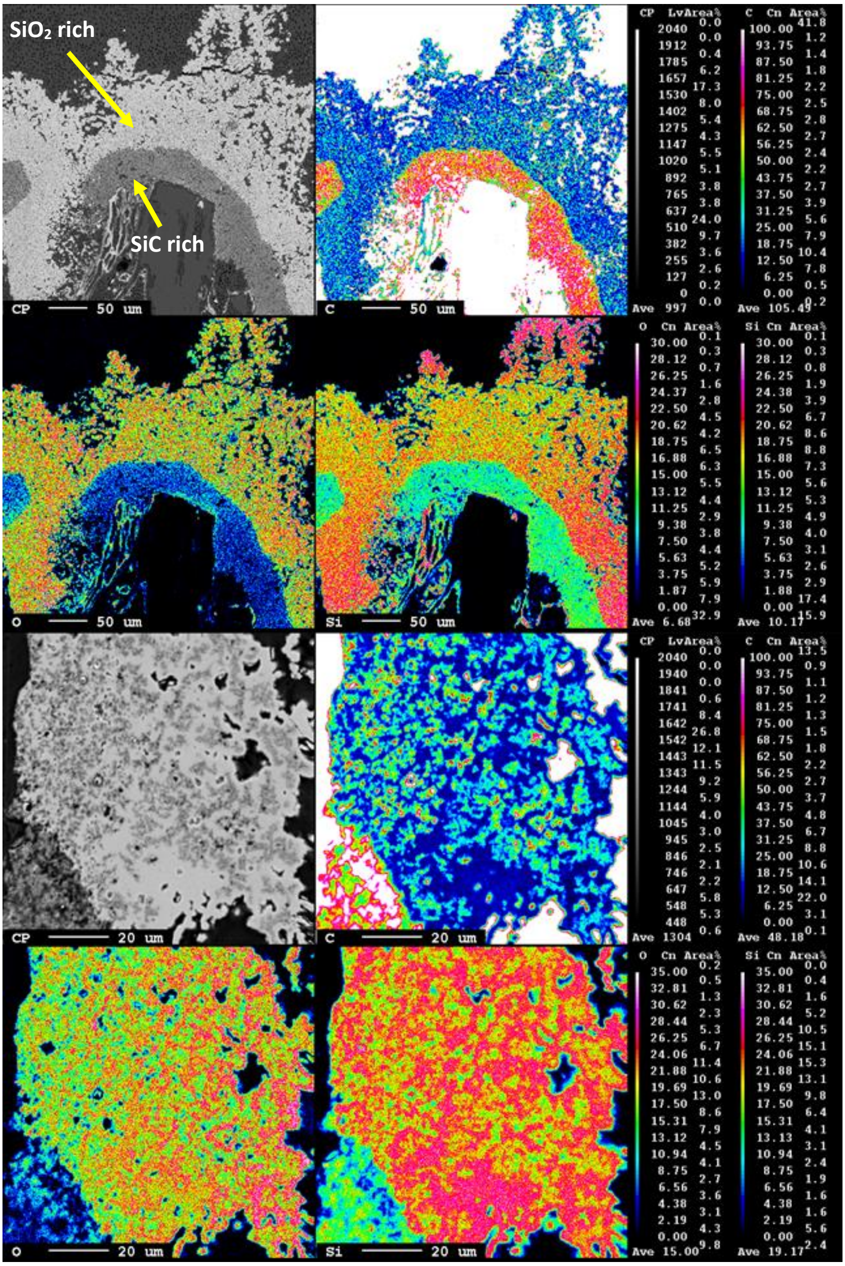

Figure 116. Elemental mapping of two areas of the condensate in sample 1.3

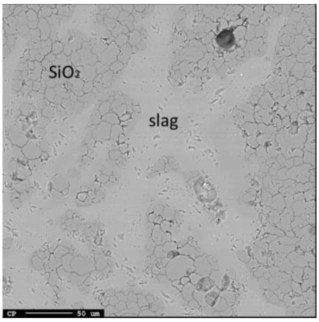

Figure 117. EPMA of sample 2.3

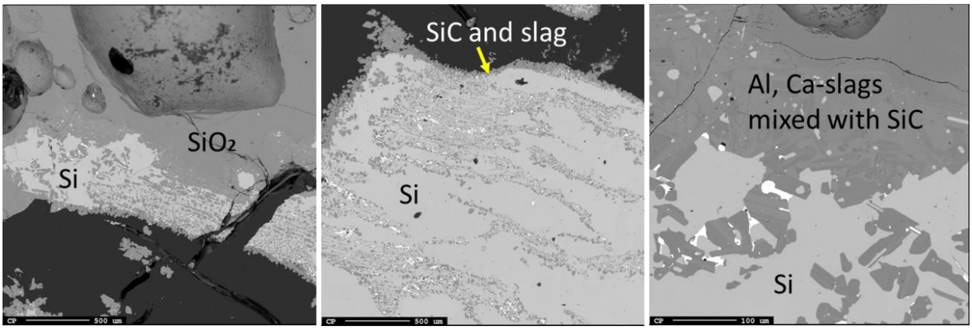

Figure 118. EPMA of three different areas of sample 2.5

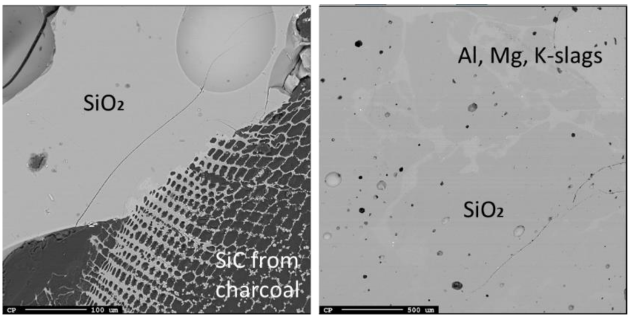

Figure 119. EPMA of two different areas of sample 3.3

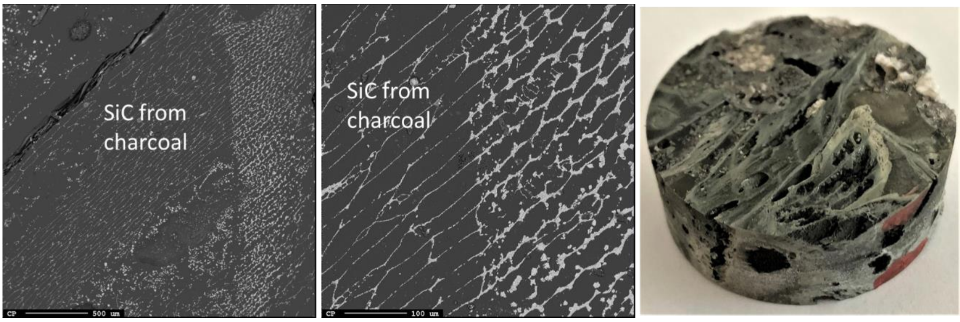

Figure 121. EPMA of two different areas of sample 4.3 and image of sample 4.3

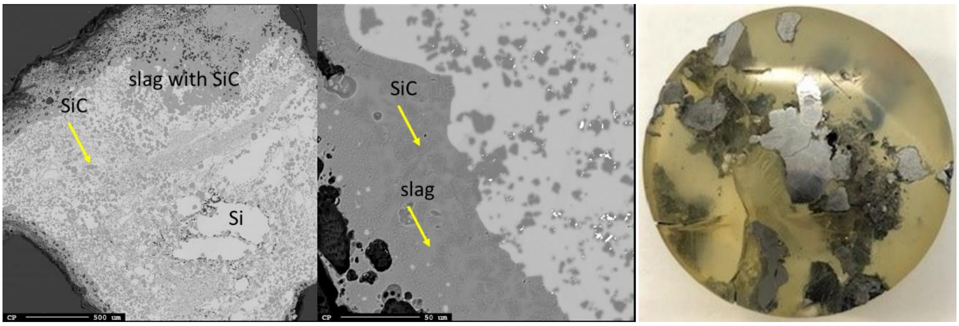

Figure 120. EPMA of sample 8.3 and image of sample 8.3

Table 18. Mass percent results from the point analysis of the slag in sample 8.3

No.	SiO_2	Al_2O_3	K_2O	CaO	Total
Average	65.4	26.5	0.8	7.5	100.2
Standard deviation	1.4	1.5	0.1	0.1	1.0

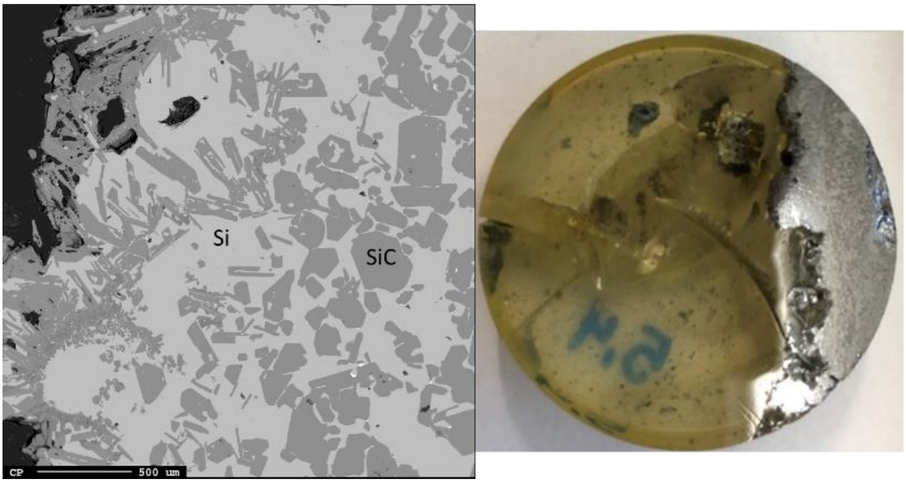

Figure 122. EPMA of sample 5.4 (left) and image of sample 5.4 (right)

6.2.3 Liquid silicon and slag

There was no small cavity or crater seen around the electrode tip position, but rather a lot of silicon and slag. Below around 35cm below the charge top, all the samples appear metallic and was considered the liquid Si/slag region. A total of three samples were analyzed (Figures 123-125). All three samples contained large amounts of Si and slag. As the metal phase solidified upon cooling, Fe also precipitated out and formed FeSi upon the phase boundary, as is visible in Sample 1.7 (Figure 123). Sample 7.4 (Figure 125) also saw an area of SiO_2 that appears to be a piece of quartz that fell during stoking. No SiC crust was found in this region and all the SiC was distributed in the slag. Table 19 shows a point analysis of the slag in sample 7.4. It has a high silica content (69.7±0.8 %) with alumina (22.0±0.8 %) and calcia (9.3±0.3 %). Small amount of K_2O were also present. This composition is similar to the slag found in sample 8.3 (Table 18) even though there are 10cm difference in the depth of the samples.

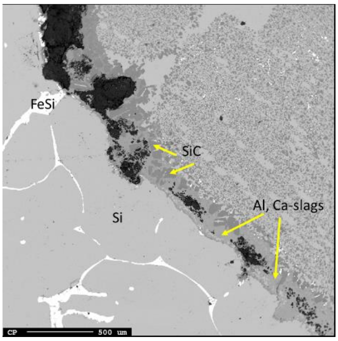

Figure 123. EPMA of sample 1.7

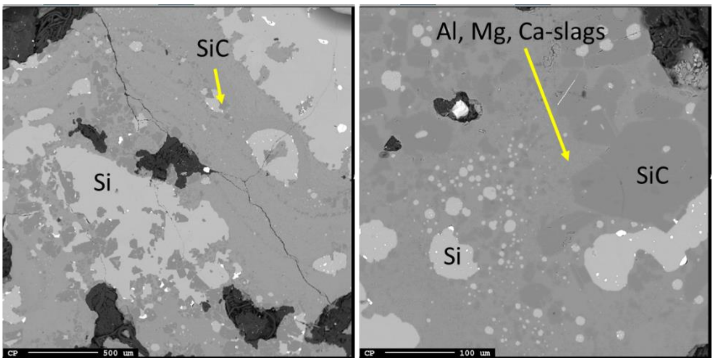

Figure 124. EPMA of two different areas of sample 1.8

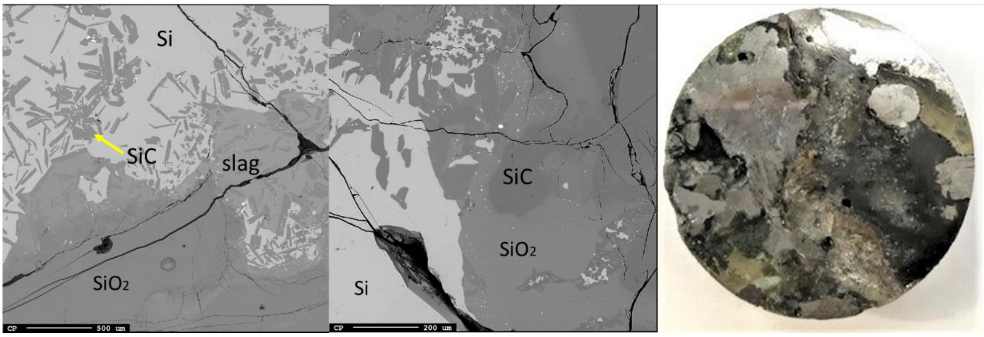

Figure 125. EPMA of sample 7.4 and image of sample 7.4

Table 19. Mass percent results from the point analysis of the slag in sample 7.4

No.	SiO_2	Al_2O_3	K_2O	CaO	Total
Average	69.7	22.0	0.3	9.3	101.5
Standard Deviation	0.8	0.8	0.0	0.3	0.3

6.2.4 Lining

Two samples (Figures 126 and 127) were taken in the region that appeared to be the SiC lining of the furnace. They are around 50-60 cm deep in the furnace. As expected, the samples were mostly SiC, with pockets of Si and FeSi throughout. Sample 6.5 (Figure 127) also contained some slag with the same composition seen in other areas of the furnace. The cores were taken close to the electrode, so the bottom lining appears to have eroded and silicon and slag have penetrated the original lining.

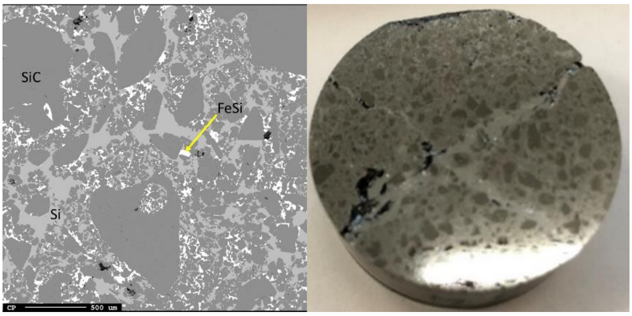

Figure 126. EPMA of sample 5.6 (left) and image of sample 5.6 (right)

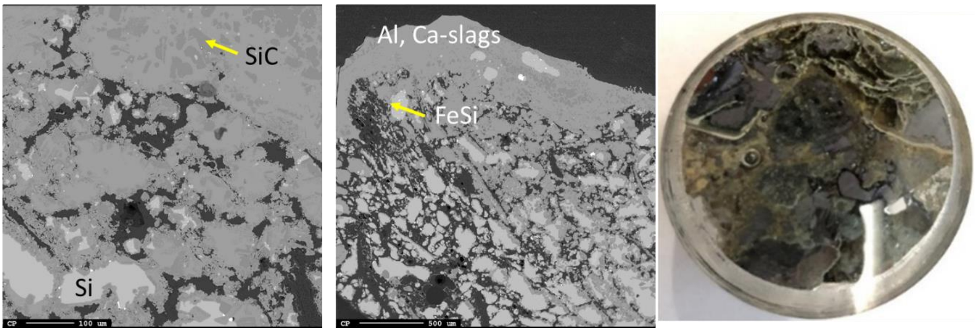

Figure 127. EPMA of two different areas of sample 6.5 and image of sample 6.5

6.3 DISCUSSIONS OF ZONES IN THE FURNACE

While each furnace is unique based on history of operations, pilot scale furnace experiments offer insight into how well the theory is executed in the large scale. This section will compare what was found in the excavation of the pilot scale with other pilot scale and industrial excavation results. These can further be compared to what the theory predicts, and how and why some results may deviate from the theory.

Figure 128 shows the recreated cross section of the furnace based on the excavation. The charge and condensate layer is shown in dark blue. The top cavity is outlined in gray. Partly reacted material is gold, and the silicon and slag layer is light blue. Areas outside these zones are labeled as "inactive charge" shown in blue-gray, as these areas are low in temperature and SiO pressure and will likely not be very reactive. An estimated bottom cavity is shown by a dotted line. The bottom cavity is assumed to be around the electrode tip and not in direct contact with the silicon-slag layer, even though this layer was found at heights that could reach the electrode. However, the high conductivity of liquid silicon would likely cause a short circuit. Nevertheless, the ratio of silicon to slag will also play a factor here, as increased slag content will increase the resistivity and the viscosity of the silicon-slag mix.

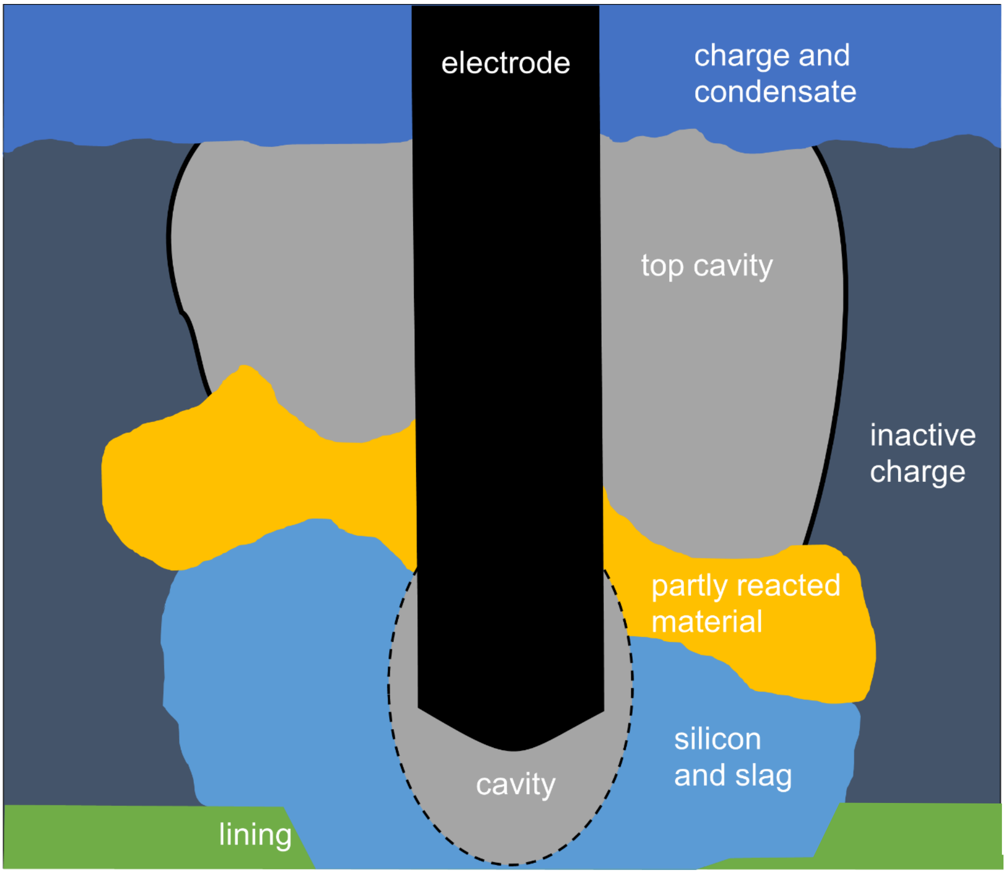

Figure 128. Cross section of pilot scale furnace with estimated cavity based on Myrhaug [28]*. The charge and condensate layer is shown in dark blue. The top cavity is outlined in gray. Partly reacted material is gold, and the silicon and slag layer is light blue. Areas outside these zones are labeled as "inactive charge" shown in blue-gray.*

The glassy condensate at the top of the silicon furnace acts as a glue which keeps the charge in place. In the pilot scale experiment, there was a cavity directly below this layer, referred to as a top cavity. This is consistent with Myrhaug's [3] work which also saw a cavity higher up in the furnace. This would typically be an example of how the furnace will form top cavities between the stoking cycles, as this furnace was not stoked after the last tapping. However, this was not previously believed to be the case as Schei et al [2], for example, did not report top cavities. When stoking the furnace industrially, this top cavity is destroyed, not the bottom, as previously thought.

Furthermore, there was no small cavity or crater seen around the electrode tip position, but rather a lot of silicon and slag. This has also been seen in previous excavations [28, 29]. As the arc is typically around about 10cm [13], the cavity can be quite small, even though also larger cavities are seen [23]. When a small cavity exists, this may be hidden during the excavation by charge materials descending after the shut-down. In the electric pattern measured, one has shown that Si production is heated by arcs [13], and hence by definition it is believed that a cavity exists even if that is not seen in the excavations.

Characterization of the condensate showed the presence of alumina, K_2O and Na_2O. It is believed that the alumina comes from the ash in the coal/coke, while potassium is found in both the carbon materials and the quartz. In addition, brown condensate consistent with other excavations was seen. As seen in previous investigations, the Si in the brown condensate will separate from the condensate over time and temperature, hence from excavations the enveloping layer is often only SiO_2 [22] [30] [80].

Below the top cavity was partly reacted charge material. This layer was also relatively small, with some cores only having a couple of centimeters of partly reacted charge materials. This is in contrast with Vangskåsen's [7] work, which saw a large layer of partly reacted materials both high and low in the furnace. Myrhaug's [3] work seems to be in closer agreement, as there is not a lot of partly reacted material in that area and this layer is lower in the furnace.

A large silicon and slag layer was seen in this pilot scale. This layer appears larger than both Myrhaug [3] and Vangskåsen's [7] results. In Myrhaug's [3] work the area around the electrode tip is more complex, containing both SiC crust and a bottom cavity. Vangskåsen's [7] silicon pool was not as large and separated from the electrode by both a cavity and a layer of partly reacted charge.

SiC is found in four main forms in the silicon furnace. The first is solid β-SiC that has formed via SiO gas reacting with solid carbon. The original structure is maintained, and it appears green in color. The second is dense β-SiC that is found mixed in liquid slag. The third is SiC whiskers formed via the gas-gas- reactions $3SiO+CO=SiC+2SiO_2$ and $SiO+3CO=SiC+CO_2$. The fourth is α-SiC, also called "black SiC" or "SiC crust", which is formed at high temperature from solid β-SiC or through the gas phase. SiC of the first three types were found in the pilot scale experiment. However, no SiC crust was found.

In the charge and condensate layer, the carbon materials are typically not transformed to SiC. A sample taken from high in the furnace showed green SiC (sample 6.1, Figure 114) was the exception. The color and structure was consistent with previous works of SiC made from carbon materials [27] [40]. However, SiC needs sufficient temperature and SiO pressure to transform the carbon. High up in the furnace, this would be unlikely, implying the presence of hot gas channels. Sample 2.5 (Figure 118), in the partly reacted material zone, shows an example where almost all SiC was transformed to Si. Typically, one sees a thin rim of SiC according to the original C particle, while most of the interior is filled with Si. This is also seen in previous investigations [10] [11] [12]. Sample 2.5 is lined with SiC and slag mixed.

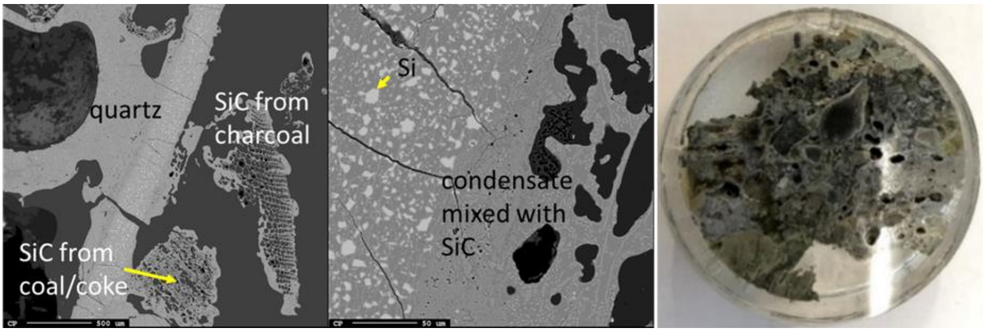

Figure 129. Sample 6.1 and it's BSE images, same as Figure 114, taken from the top of the furnace in core 6.

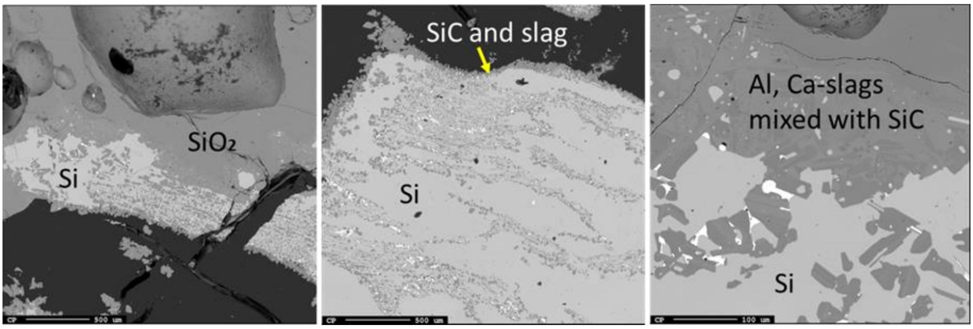

Figure 130. BSE images of sample 2.5, same as Figure 118, taken from the area below the top cavity.

The slag seen in this pilot scale contained mostly silica, alumina, and calcia, which is consistent with what is expected in the Si furnace [69]. Based on the literature, this slag will have a low conductivity and high viscosity due to the high silica content and the low CaO/Al_2O_3 ratio [70]. The sample from deeper in the furnace (sample 7.4) has a slightly higher silica content, 69.7±0.8 % compared to sample 8.3 with 65.4±1.4 %, which is surprising since the silica content generally decreases in the slag as one goes deeper in the furnace [69]. However, the difference is small and perhaps the presence of the quartz particle in this area is responsible for the small amount of additional silica.

The estimated resistivity in the various zones is shown in Table 20. The resistivity of the arc is not discussed.The charge and condensate as well as the inactive charge zone are probably not conductive due to the high amount of SiO_2 and the low temperature. The partly reacted materials layer can be very diverse, so it is taken separately. There is the charge mix excluding SiC and Si, and partly reacted materials that are only SiC, C, and Si. In the furnace these two would coexist in different ratios depending on temperature and SiO pressure. The resistivity of the silicon-slag layer is suspected to be between the literature value for silicon and slag (with a similar composition to the pilot scale slag) at 1600 °C. However, the real value would depend on the silicon to slag ratio.

Table 20. Estimated temperature and resistivity of various zones in the pilot scale furnace

Material zone	Estimated temperature (°C)	Estimated resistivity (mΩm)
Charge and condensate	1000	Nonconductive
Charge mixes with char, quartz, and woodchips/charcoal (excluding SiC and Si)	1400	70-100
Partly reacted SiC materials (SiC, C, and Si only)	1600	10-35
Silicon [59] and slag [70]	1600	0.007-300
Inactive charge zone	<1000	Nonconductive

6.4 CONCLUSIONS

The excavation of this pilot scale furnace showed several points of interest, mainly the presence of only a top cavity and no cavity around the electrode tip. The top cavity was held in place by a layer of loose charge and condensate, the latter consisting of mainly silica, alumina, and K_2O. Significant amounts of silicon were found just below the top cavity, however droplets were also seen above the top cavity. Additionally, no α-SiC crust was found, but SiC was seen in other forms throughout the furnace. Slag containing silica, alumina, and calcia was found throughout the furnace, usually mixed with SiC. Based on the estimated resistivity of each of the layers, the silicon-slag layer should be the most conductive, followed by the partly reacted materials at higher temperatures. The resistivity in the furnace, therefore, should be lowest at the bottom of the furnace, and higher towards the outer edges and the top.

7 CONCLUSIONS AND FUTURE WORK

This chapter summarizes the main findings in this work, beginning with the transformation to SiC, followed by the electrical resistivity, and finally the pilot scale excavation. Suggestions for further work are then given.

7.1 CONCLUSIONS

The transformation of coal, char and charcoal to SiC was examined and the resulting material was characterized. All three materials saw both SiC surface crystals and surface whiskers, however less whiskers were seen in the charcoal. In general, the SiC will begin to form on the outer edges of the particle and around the pores according to the shrinking core model. As the SiC layer thickens, elemental silicon can begin to form in the pores where there is high conversion to SiC, even with other areas of the particle still containing carbon. This is according to the grain model. As the remaining carbon disappears, the particle becomes SiC with elemental silicon forming in the pores. Although transformation in a bed of particles can be heterogeneous due to gas flow and the temperature gradient, the mechanism could still be seen in all three carbon materials. In a bed of particles, there will be unequal access to the gas, creating some areas which are highly converted to SiC and others which are not even within the same area of the setup. Using CT to image groups of particles was able to give an indication of SiC and carbon but could not definitively show the different phases.

Mechanical strength decreased with conversion to SiC for the materials from coal, until silicon began to form. The opposite was seen in char, where the strength increased with conversion to SiC for the materials from char. The char was seen to be weaker than the coal. Both of them were however much weaker than the strength reported in the literature of commercial β-SiC. Charcoal produced the most elemental silicon, even when the temperature was lower compared to coal and char. Coal and char required at least 60-70 %SiC before silicon was detectable in the sample, while charcoal required 50 %. This is likely due to the ability of SiO gas to diffuse into the charcoal.

The resistivity of partly transformed carbon materials containing SiC and Si was measured between 25-1600 °C. The resistivity of the carbon materials was between 7-20 mΩm at 1600 °C, where the charcoal had the largest range, since it accounted for both the highest and lowest measurement. The chars had a range between 10-15 mΩm and the coals between 5-10 mΩm, when including literature values with similar particle sizes. Density can explain these trends at lower temperatures, but at high temperatures density cannot predict the resistivity. Comparisons between the heat treated and untreated chars showed that the lower volatile content lowers the resistivity and makes it less sensitive to temperature. Comparison between industrial charcoal and homemade charcoal from recovered woodchips showed that the homemade charcoal was also less sensitive to temperature, and it was conductive at lower temperatures but had an overall higher resistivity than industrial charcoal at high temperature. This is likely due to the higher heat treatment temperature and the increased mechanical strength.

The resistivity of partially transformed materials increased with conversion to SiC and then began to decrease as elemental Si formed in the pores. While the presence of Si lowered the resistivity, the actual quantity of the Si in the sample, up to 36 %, did not seem to have an effect. This could be because the porosity is decreasing. CT scans of the resistivity setup before and after measurement show that the SiC material is not visibly changing or transforming in the crucible during measurement. Comparing the SiC materials to carbon materials and SiC crust from literature shows that partially transformed SiC will be as conductive or less conductive than carbon at high temperature, but after 1300 °C the α-SiC crust will be more conductive. Resistivity of mixtures of the charge mixes used in Si/FeSi was also investigated. At 1400 °C, the resistivity of the charge mixes that included char, quartz, woodchips, and silica-iron ore showed that the resistivity is dependent on the amount of the main conductive material, in this case char.

The results of the excavation of the 160 kW pilot scale furnace were similar to those of other pilot scale experiments and excavations but had several unique points of interest. A top cavity was seen high up in the furnace and held in place by a layer of condensate and loose charge. The condensate contained alumina, K_2O, and a small amount of Na_2O, likely from impurities in the carbon and quartz. Additionally, Si was found above the cavity in droplets, but more significant amounts of Si were seen at a depth of about 25 cm, just below the top cavity. No cavity was seen around the electrode tip. No areas of SiC crust were identified, and it is believed to be absent because it would likely form close to the electrode tip. Other forms of SiC were found throughout the furnace from both solid-gas and gas-gas reactions. Slag of similar compositions, usually alumina and calcia with small amounts of trace oxides, were also found throughout the furnace, usually mixed with SiC.

7.2 FUTURE WORK

As mentioned in Chapter 3, the formation of the partially transformed SiC was initially done to provide the raw materials for the resistivity measurements. Therefore, a lot of liberties were taken. In future studies of the formation of SiC in a bed of particles, there are three main recommendations worth mentioning. First, the use of the graphite sieve should become standard, in addition to using a coating of boron nitride to prevent wetting of the SiO_2-Si mixture. The second recommendation would be adding a graphite lid to the top of the setup, this prevents heat loss and oxidation of the top of the carbon bed. It would also keep the thermocouple in place. The final recommendation would be to experiment with casting the crucible in epoxy after the experiment and defining and characterizing the layers using that method. This reduces the variability in the layers, as well as showing any gas channels and the temperature gradient. Samples can then be drilled from precise locations and characterized.

CT as a method for investigating the transformation of carbon to SiC and the formation of Si is promising, but more verification is needed. Scanning one particle at a time would ensure maximum resolution to better differentiate the phases. These suspected phases could then be verified in the SEM or EPMA to definitively prove that the color differences seen on the CT correspond to the SiC and carbon phases in the particles.

The electrical resistivity measurements of the partially transformed SiC were novel at the time, so the primary recommendation for future work is to build on these results. Additional samples with differing SiC content are needed, in particular for the charcoal, in which all samples contained elemental silicon. Furthermore, smaller setups for bulk resistivity may be more prudent if the materials are self-made to reduce the preparation time and resources. Furthermore, modifications to the setup, such as changing the alumina, could allow for higher temperatures to be measured.

In addition, the bulk resistivity is measured in this work, but measuring the material resistivity of carbon as it is transformed to SiC would also be of great importance. This was tried using charcoal cylinders during the final part of this PhD, however, there were problems with the setup that prevented any measurements from being done within the time frame.

Additional research into the bulk resistivity of the charge mixes would also be of great interest. To the author’s knowledge there have been no other measurements of the resistivity of the charge mix. As such, the results here are very preliminary and there was a lot of variability due to the size of the setup and the large amount of insulative material. Future work should verify the dependence of the resistivity on the main conductor and more clearly define the minimum threshold needed for the bed to be conductive.

8 REFERENCES

1. U.S. Geological Survey. 2020. *Mineral Commodities Summary: Silicon.* U.S.G.S.

2. Schei, Anders, Johan Kr. Tuset, and Halvard Tveit. 1998. *Production of High Silicon Alloys.* Trondheim: Tapir Forlag.

3. Krokstad, M. 2014. *Electric Resistivity in Industrial SiC-slag.* MSc Thesis, Department of Natural Sciences, Institute of Material Technology, Trondheim: NTNU.

4. Bharat, S. 2022. *Influence of high temperature thermal cycles on the electrical resistivity of charcoal.* BEng Final Project, Department of material science and metallurgical engineering, University of Pretoria, Faculty of Engineering.

5. Cromarty, R., and J. Nhiwatiwa. 2021. "Evaluation of coke resistivity for the manganese alloy market." *INFACON XVI.* Trondheim.

6. Eidem, Per Anders. 2008. *Electrical Resisitivity of Coke Beds.* PhD Thesis, Department of Material Science and Engineering, Faculty of Natural Sciences and Technology , Trondheim: NTNU.

7. Pedersen, T. 2020. *Electrical Resistivity in Carbon Materials Converting to SiC.* MS Thesis, Department of Natural Sciences, Institute of Material Technology, Trondheim: NTNU.

8. Surup, G. R., T. A. Pedersen, A. Chaldien, J. P. Beukes, and M. Tangstad. 2020. "Electrical resistivity of carbonaceous bed material at high temperature." *Processes.*

9. Surup, G.R., N. Smith-Hanssen, and M. Tangstad. 2021. "The properties of carbon blends in submerged arc furnaces." *INFACON XVI.* Trondheim.

10. Surup, G. 2019. *Renewable reducing agents for the use in ferroalloy industries.* PhD Thesis, Department of engineering sciences, University of Agder, Agder: Faculty of Engineering and Science.

11. Tangstad, Merete. 2013. *Metal production in Norway.* Trondheim: Akademika Publishing.

12. Monsen, B.E., T. Lindstad, and J.K. Tuset. 1998. "CO2 Emissions from the Production of Ferrosilicon and Silicon metal in Norway." *Electric Furnace Conference Proceedings.* Norwegian University of Science and Technology. 371-378.

13. Sævarsdottir, G., and J.A. Bakken. 2010. "Current distribution in submerged arc furnaces for silicon metal/ferrosilicon production." *The Twelfth International Ferroalloys Conference.* Helsinki, FInland. 717-728.

14. Tesfahungegn, Y.A., T. Magnusson, M. Tangstad, and G. A. Sævarsdottir. 2018. "Effect of Carbide Configuration on the Current Distribution in Submerged Arc Furnaces for SIlicon Production- A Modelling Approach." *CFD Modeling and Simulation in Materials Processing* 175-185.

15. Tefsahunegn, Y.A., T. Magnusson, M. Tangstad, and G. Sævarsdottir. 2020. "The Effect of Side Arcs on Current Distributions in a Submerged Arc Furnace for Silicon Production." Chap. 16 in *Materials Processing Fundamentals 2020*, 177-188. TMS Springer.

16. Gerritsen, T., P. Tracy, and F. Saber. 2015. "Electrode Voltage Measurement in Electric Furnaces: Analysis of Error in Measurement and Calculation." *INFACON Energy efficiency and environmental friendliness are the future of the global Ferroalloy industry* 338-348.

17. Magnussen, T.E. 2018. "Basic parameters in the operation and design on submerged arc furnaces, with particular reference to production of high-silicon alloys." *The Journal of the Southern African Institute of Mining and Metallurgy* 118: 631-636.

18. Westly, J. 1974. "Resistance and Heat Distribution in a Submerged-arc Furnace." *INFACON 1* 121-127.

19. Nurmukhanbetov, Zh., O. Privalov, and L. Prokopyev. 2013. "Reducibility and electric resistance of carbonaceous materials within ferroalloy smelting processes." *The thirteenth International Ferroalloys Congress: Efficient technologies in ferroalloy industry.* Almaty.

20. Tesfahunegn, Y.A., T. Magnusson, M. Tangstad, and G. Sævarsdottir. 2018. "Effect of electrode shape on the current distribution in submerged arc furances for silicon production- A modelling approach." *The Journal of the Southern African Institute of Mining and Metallurgy* 118: 595-600.

21. Tesfahunegn, Y. A., T. Magnusson, M. Tangstad, and G. Sævarsdottir. 2021. "The Effect of Electrode Movemetns on Inductive Reactance in a Submerged Arc Furnace."

INFACON XVI: International Ferro-Alloys Congress. Trondheim : SINTEF/NTNU/FFF. 1-9.

22. Ksiazek, M., M. Tangstad, and E. Ringdalen. 2016. "Five furnaces five different stories." *Silicon for the chemical and solar industry XIII.* Kristiansand.
23. Tranell, G., M. Andersson, E. Ringdalen, O. Ostrovski, and J.J. Steinmo. 2010. "Reaction zones in a FeSi75 furnace - results from an industrial excavation." *The Twelth International Ferroalloys Congress.* Helsinki. 709-715.
24. Tangsatd, M. 2021. "The Si SAF process- an overview." Course Lecture and Powerpoint Presentation, Trondheim: NTNU.
25. Tangstad, M., and M. Ksiazek. 2021. *Picture book: zones and materials in Si/FeSi furnaces.* Trondheim: NTNU.
26. Vangskåsen, J. 2012. *Metal-producing mechanisms in the carbothermic silicon process.* MSc Thesis, Trondheim: MSc Thesis, Department of materials science and engineering, Faculty of Natural Science, Norwegian University of Science and Technology.
27. Bø, S. M. 2016. *Phases and zones in the silicon process.* MSc Thesis, Department of materials technology, Trondheim: NTNU.
28. Myrhaug, E. H. 2003. *Non-fossil reduction materials in the silicon process- properties and behaviour.* PhD Thesis, Department of materials technology, Trondheim: NTNU.
29. Tangstad, M., M. Kiazek, V. Andersen, and E. Ringdalen. 2010. "Small Scale Laboratory Experiments Simulating an Industrial Silicon Furnace." *The Twelth International Ferroalloys Congress.* Helsinki. 661-670.
30. Broggi, A., M. Tangstad, and E. Ringdalen. 2019. "Characterization of a Si-SiO2 Mixture Generated from SiO(g) and CO(g)." *Metallurgical and Materials Transactions B* 50: 2667-2680.
31. Jayakumari, Sethulakshmy, and Merete Tangstad. 2018. "Silicon Carbide formation from coal or charcoal in the silicon/ferrosilicon process." *Infacon XV: International Ferro-Alloys Congress.* Cape Town: South African Institute of Mining and Metallurgy. 1-14.

32. Bouanga, C.V., S. Savoie, M.F. Frechette, H. Couderc, and E. David. 2012. "Electrical Resitivity Characterization of Silicon Carbide by Various Methods." *IEEE* 43-47.

33. Harris, Gary. 1995. *Properties of Siicon Carbide.* London: Institution of Electrical Engineers.

34. Ayalew, Tesfaye. 2004. "SiC Semiconductor Devices Technology, Modeling, and Simulation." PhD Thesis, Faculty of Electrical Engineering and Information Technology, Technical University of Vienna, Vienna.

35. Izhevskyi, V.A., L.A. Genova, J.C. Bressiani, and A.H.A. Bressiani. 2000. "Silicon Carbide Structure, Properties, and Processing." *Ceramica* 46 (297).

36. Haynes, W. M. 2011. *CRC Handbook of Chemistry and Physics.* Boca Raton: CRC Press.

37. Myrvågnes, Viktor. 2008. *Analyses and Characterization of Fossil Carbonaceous Materials for Silicon Production.* PhD Thesis, Department of Material Science and Engineering, Faculty of Natural Sciences and Technology, Trondheim: Norwegian University of Science and Technology.

38. Smith-Hanssen, N. 2021. *SiO Reactivity Test.* SINTEF. Accessed April 30, 2021. https://www.sintef.no/en/all-laboratories/process-metallurgical-laboratories/sio-reactivity-test/#/.

39. Ramos, Diego Correa. 2018. *Quality of Eucalyptus Charcoal for use in Silicon Production.* PhD Thesis, Minas Gerais: Universidade Federal de Viscosa.

40. Norbø, Eirik Andre. 2019. *Interaction of SiO-gas and Charcoal and the Formation of SiC and Si.* MSc Thesis, Trondheim: MSc Thesis, Department of Material Science and Engineering, Faculty of Natural Sciences, Norwegian University of Science and Technology.

41. Jayakumari, S. 2020. *Formation and Characterization of Β- and a- Silicon Carbide Produced During Silicon/Ferrosilicon Process.* PhD Thesis, Trondheim: PhD Thesis, Department of Material Science and Engineering, Faculty of Natural Sciences, Norwegian University of Science and Technology.

42. Szekely, J., J.W. Evans, and H. Y. Sohn. 1976. *Gas-Solid Reactions.* New York: Academic Press.

43. Myrhaug, E. H., J.K. Tuset, and H. Tveit. 2004. "Reaction Mechanisms of Charcoal and Coke inthe Silicon Process." *Tenth International Ferroalloys Congress.* Cape Town. 108-121.

44. Abolpour, B., and R. Shamsoddini. 2019. "Mechanism of reaction of silica and carbon for producing silicon carbide." *Progress in Reaction Kinetics and Mechanism* 45: 1-14.

45. Chen, Z., S. Zhou, W. Ma, X. Deng, S. Li, and W. Ding. 2018. "The effect of the carbonaceous materials properties on the energy consumption os silicon production in the submerged arc furance." *Journal of Cleaner Production* (Elsevier) 191: 240-247.

46. Arnold, B. J. 2013. *The Coal Handbook.* Elsevier Science & Technology. Accessed October 2018. doi:10.1533/9780857097309.1.31.

47. University of Kentucky. n.d. *Coal.* www.uky.edu/KGS/coal/index.php.

48. EIA. 2018. *Coal Explained.* November. www.eia.gov/energyexplained/index.php?page=coal_home.

49. Crelling, J. C. 2008. "Chapter 7- Coal Carbonization." In *Applied Coal Petrology The Role of Petrology in Coal Utilization*, 173-192. Elsevier.

50. Tiwari, H.P., and V. K. Saxena. 2019. "Industrial perspective of the cokemaking technologies." In *New trends in coal conversion*, 203-246. UK: Elsevier.

51. Elkem. 2019. *Important milestone on the road to carbon-neutral metal production.* Elkem. November. https://www.elkem.com/sustainability/carbon-neutral-metal-production-charchoal/.

52. FAO. 1985. *Industrial Charcoal Making.* Manual, Mechanical Wood Products Branch, Forest Indsutries Division, Rome: Food and Agricultural Organization of the United Nations.

53. Monsen, B., M. Tangstad, and H. Midtgaard. 2004. "Use of Charcoal in Silicomanganese Production." *INFACON X.* Cape Town. 392-404.

54. Tangstad, Merete, Johan Paul Beukes, Joalet Steenkamp, and Eli Ringdalen. 2019. "Coal-based reducing agents in ferroalloys and silicon production." In *New Trends in Coal Conversion*, 405-435. UK: Elsevier.

55. Jusnes, K. F. 2020. *Phase transformations and thermal degradation in industrial quartz.* PhD Thesis, Department of material science and engineering, Norwegian Univeristy of Science and Technology, Trondheim, Norway: Faculty of Natural Sciences.

56. Serway, R., and J. Jewett. 2004. *Physics for Scientists and Engineers.* 6th. Thomson Brooks/Cole.

57. Smith, William, and Javad Hashemi. 2009. *Foundations of Materials Science and Engineering.* 5th. Ann Arbor, Michigan: McGraw Hill Education.

58. Law, J.T., and E.E. Francois. 1956. "Adsorption of gases on a silicon surface." *The Journal of Physcial Chemistry* 60 (3): 353-358.

59. Sasaki, H., A. Ikari, K. Terashima, and S. Kimura. 1995. "Temperature Dependence of the Electrcial Resistivity of Molten SIlicon." *Journal Applied Physics* 34: 3426-3431.

60. Seydel, U., and W. Fucke. 1977. "Sub-Microsecond Pulse Heating Measurements of High Temperature Electrical Resistivity of the 3d-Transition Metals Fe, Co, and Ni." *Zeitschrift für Naturforschung A* 32 (9): 994-1002.

61. Pelissier, K., T. Chartier, and J.M. Laurent. 1997. "Silicon Carbide Heating Elements." *Ceramics International* 24 (2): 371-377.

62. Singh, Yadunath. 2013. "Electrical Resistivity Measurements: A Review." *International Journal of Modern Physics* 745-756.

63. Heaney, Michael B. 2003. "Electrical Conductivity and Resistivity." In *Electrical Measurements, Signal Processing, and Displays*, 7-1 - 7-14. Berkeley: CRC Press LLC.

64. Krogerus, H., T. Lintumma, and P. Jokinen. 2006. "Laboratory Investigations of the Electrical Resistivity of Cokes and Smelting Charge for Optimizing Operation in Large Ferrochrome Furnaces." *Southern African Pyrometallurgy* 309-328.

65. Hasannezhad, H., and A. Meysami. 2018. "Effects of Porosity and Electrical Resistance of Metallurgical Coke and Semicoke on Silicon Recovery in a Electric Arc Furnace." *Electric Arc Smelting* 336-341.

66. Pedersen, T. 2019. *Method for measuring bulk resisitivity in particulate carbon materials.* Project Report for TMT4500, Department of Material Science and Engineering, Trondheim: Norwegian University of Science and Technology, 1-8.

67. Kim, G., Y. Kim, I. Song, and K. J. Kim. 2020. "Effects of carbon and silicon on electrical, thermal, and mechanical properties of porous silicon carbide ceramics." *Ceramics International* (Elsevier) 4: 15594-15603.

68. Jusnes, K.F., R. Hjelmseth, M.B. Folstad, N.S. Ditlefsen, and M. Tangstad. 2021. "Investigation of slag compositions and possible relation to furnace operation of a FeSi75 furnace." *INFACON XVI: International Ferroalloys Congress.* Trondheim.

69. Folstad, M.B., and M. Tangstad. 2021. "SiO2-CaO-Al2O3 slags in the Si/FeSi furnaces." *INFACON XVI: International Ferroalloys Congress.* Trondheim.

70. Liu, J.H., G.H. Zhang, and K.C. Chou. 2015. "Study on electrical conductivities of CaO-SiO2-Al2O3 slags." *Canadian Metallurgical Quarterly* 54 (2): 170-176.

71. Allibert, M., H. Gaye, J. Geiseler, D. Janke, B.J. Keene, D. Kirner, M. Kowalski, et al. 1995. *Slag Atlas.* Edited by Verein Deutscher Eisenhuttenleute (VDEh). Dusseldorf: ECSC Research.

72. Sahito, A. R., R. B. Mahar, Z. Siddiqui, and K. M. Brohi. 2013. "Estimating Calorific Values of Lignocellulosic Biomass from Volatile and Fixed Solids." *International Journal of Biomass and Renewables* 1-6.

73. Swapp, S. 2017. *Scanning Electron Microscopy (SEM).* SERC. University of Wyoming: SERC. https://serc.carleton.edu/18401.

74. Goodge, J. 2019. *Electron probe micro-analyzer (EPMA).* University of Minnesota Duluth: SERC. https://serc.carleton.edu/17054.

75. Micromeritics. n.d. *Gas Displacement Pycnometry System: Accupyc II 1345.* Micromeritics. https://www.micromeritics.com/wp-content/uploads/Accupyc-II-1345-Brochure_0.pdf.

76. Ketcham, R. 2017. *X-ray computed tomography (CT).* University of Texas at Austin: SERC. https://serc.carleton.edu/18399.

77. Pabst, O., M. Schiffer, E. Obermeier, T. Tekin, K. D. Lang, and H. Ngo. 2011. "Measurements of Young's modulus and residual stress of thin SiC layers for MEMS high temperature applications." *Proceedings of SPIE, Smart Sensors, Actuators, and MEMS V.* Prague. doi:https://doi.org/10.1117/12.886453.

78. Pan, J., Z. Meng, Q. Hou, Y. Ju, and Y. Cao. 2013. "Coal strength and Young's modulus related to coal rank, compressional velocity, and maceral composition." *Journal of Structural Geology* (Elsevier) 54: 129-135. doi:https://doi.org/10.1016/j.jsg.2013.07.008.

79. Andersen, V., I. Solheim, H. Gaertner, B. Sægrov-Sorte, K. Einarsund, and G. Tranell. 2022. "Pilot scale test of flue gas recirculation for the silicon process." *TMS.* Anaheim.

80. Sindland, C., and M. Tangstad. 2021. "Production Rate of SiO Gas from Industrial Quartz and Silicon." *Metallurgical and Materials Transactions B* 52: 1755-1771.

9 APPENDIX A: OVERALL TRANSFORMATION OF CARBON TO SIC

Sample layers from one batch each of coal and charcoal were studied separately to study SiC formation in large scale setups. The temperature was kept constant at 1850 °C and the holding time was varied from 1-3 hours. Based on the values of free carbon, total carbon, and total Si, the amount of SiC, C, and Si were calculated based on equations A1-A5, which were also used by [41]. The total Si is measured using X-ray fluorescence (XRF). The total carbon is measured using LECO CS-444 and the free carbon using a LECO RC-612.

$$\%SiC = (\%C_{total} - \%C_{free}) \times \frac{MM_{SiC}}{MM_C} \tag{A1}$$

$$Si\ in\ SiC = \%SiC \times \frac{MM_{Si}}{MM_{SiC}} \tag{A2}$$

$$\%Si = \%Si_{total} - Si\ in\ SiC \tag{A3}$$

The total amount of SiC that is formed will then be the amount of SiC found in the crucible plus the amount of SiC consumed: (A4)

$$total\ SiC_{produced} = total\ SiC_{measured} + total\ SiC_{consumed}$$

From the produced amount of SiC to the total theoretical amount (if the entire carbon bed were transformed to SiC), one can then find the total conversion of carbon to SiC:

$$conversion\ to\ SiC(\%) = \frac{total\ SiC_{produced}}{total\ SiC_{theoretical}} \times 100 \tag{A5}$$

Table A1 shows the amounts of SiC and Si produced, and the percent converted of the original carbon material to SiC compared to its theoretical amount. Surprisingly, there was not a large difference between the two carbon materials. The most highly converted sample was the coal held at 2 hours (39 %), and the sample with the lowest conversion was charcoal 1 with a holding time of 1 hour (22 %). However, among the samples there was little difference between the different holding times as most of the samples fall between 25-35 %. There was also little correlation with the holding times and the amount of silicon produced. In the coal samples, the amount of silicon is similar, and in the charcoal samples the range still falls between 10 and 20 grams, except with charcoal 1 (1 hour holding time). However this may be an outlier given the corresponding 1 hour sample (charcoal 4) had 28.6 grams, the highest of all the charcoal samples. In general, coal produced more silicon than the charcoal.

Table A1: Amount and conversions to SiC from each carbon material and holding time

Carbon Material	**holding time (hrs)**	**g SiC produced**	**g Si produced**	**gSiCproduced/gSiCtheoretical (%)**
charcoal 1	1	127.2	0.5	22%
charcoal 2	2	196.3	22.7	34%
charcoal 3	3	189.6	16.3	33%
coal	1	195.2	22.5	31%
coal	2	248.8	23.8	39%
coal	3	193.3	27.6	30%
charcoal 4	1	138.1	28.6	24%
charcoal 5	2	142.1	19.9	25%
charcoal 6	3	141.9	10.8	25%

10 APPENDIX B: CHANGE OF RESISTIVITY WITH MULTIPLE MEASUREMENTS

Materials which were measured at least three times are shown in Figures 131-133. Different runs are labeled.

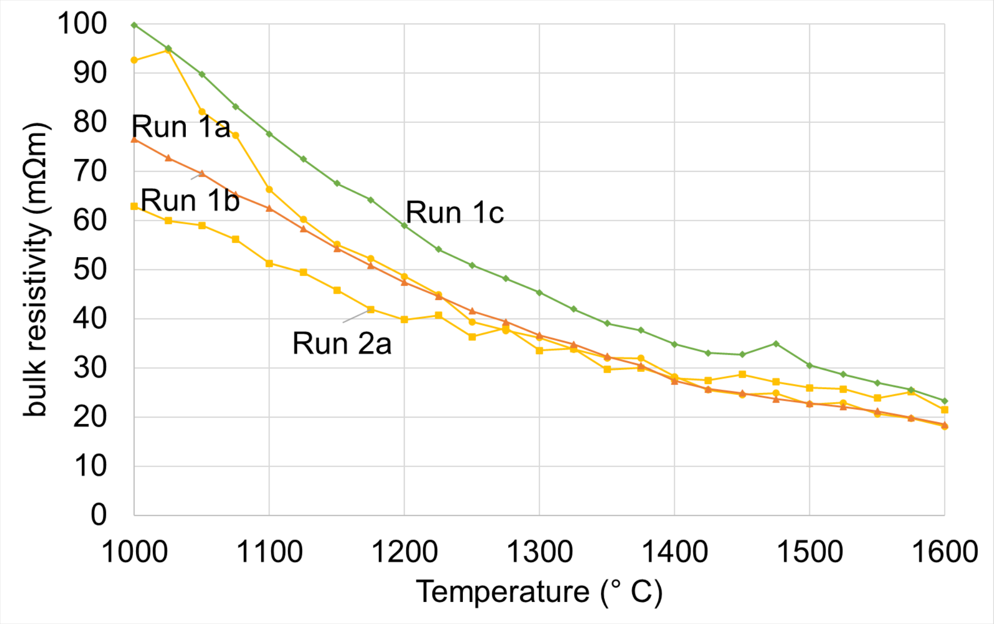

Figure 131. Resistivity with increasing temperature of all experiments with 72%SiC 7%Si from coal. Runs are labelled and colors show different packing.

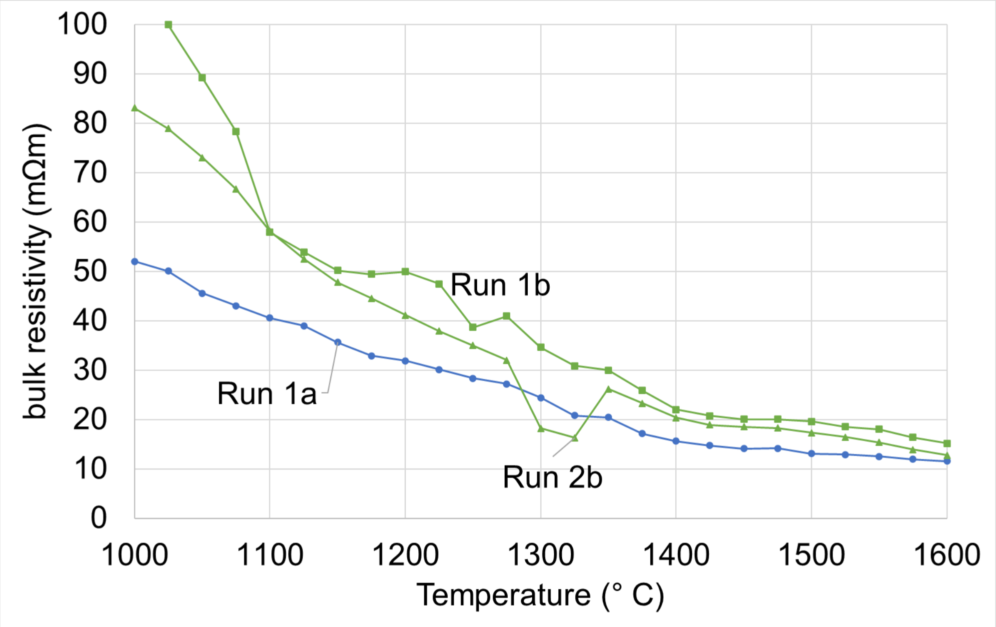

Figure 132. Resistivity with increasing temperature of all experiments with 63%SiC 2%Si from char. Runs are labelled and colors show different packing.

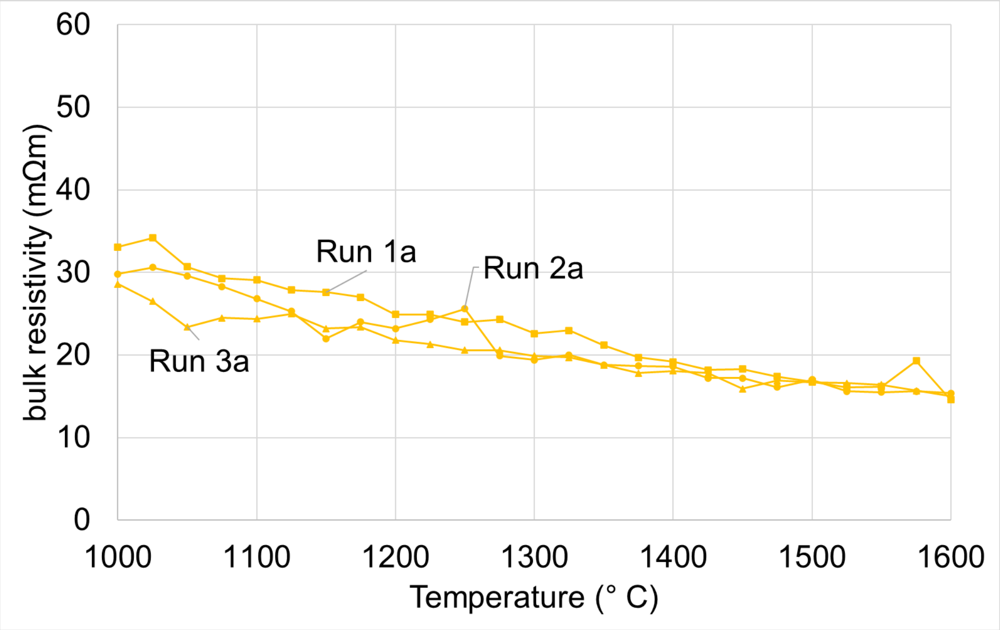

Figure 133. Resistivity with increasing temperature of all experiments with 60%SiC 6%Si from charcoal. Runs are labelled and colors show different packing.

ISBN 978-82-326-7296-7 (printed ver.)
ISBN 978-82-326-7295-0 (electronic ver.)
ISSN 1503-8181 (printed ver.)
ISSN 2703-8084 (online ver.)

NTNU
Norwegian University of
Science and Technology